SLAC-413
UC-414
(E)

A STUDY OF JET RATES AND MEASUREMENT OF α_s AT Z^0 RESONANCE

Jan A. Lauber

STANFORD LINEAR ACCELERATOR CENTER
STANFORD UNIVERSITY, STANFORD, CALIFORNIA 94309

February 1993

Prepared for the Department of Energy
under contract number DE-AC03-76SF00515

To my parents Elise and Konrad

who made my studies in the U.S. possible

A Study of Jet Rates and a Measurement of the Strong Coupling α_s at the Z^0 Resonance

Lauber, Jan A., (Ph.D., Physics)

Thesis supervised by Professor Uriel Nauenberg

This experiment was performed with the SLD detector at the Stanford Linear Accelerator Center. Only charged tracks measured in the central drift chamber were used for the measurement of the jet production rates.

The value of the strong coupling $\alpha_s(M_{Z^0})$ is determined from the production rates of jets in hadronic Z^0 decays in e^+e^- annihilations. The relative jet rates are obtained using the JADE-type algorithms. The results are compared with the jet rates obtained from a new jet algorithm proposed by N. Brown et al. called the "Durham" algorithm. The data can be well described by $\mathcal{O}(\alpha_s^2)$ QCD calculations and by QCD shower model calculations. A fit of the theoretical predictions to the data taken with the SLD yields a value

$$\alpha_s(M_{Z^0}) = 0.120 \pm 0.002(stat.) \pm 0.003(\mathrm{exp.})^{+0.011}_{-0.009}(\mathrm{theor.})$$

The error is dominated by the theoretical uncertainties. The measurement is compared with results from other experiments and it is shown that the value obtained for α_s agrees well with these results and furthermore supports the evidence for the running of the strong coupling, consistent with the non-Abelian nature of QCD.

The Stanford Linear Collider (SLC) can deliver partially longitudinally polarized electrons to the interaction point. Jet production rates and values for α_s are calculated both for right–handed and left–handed initial state electrons. All results are consistent with the unpolarized result, as predicted by the Standard Model.

ACKNOWLEDGMENTS

Above all I would like to thank the entire SLD/SLC collaboration who pulled this experiment through with determination, despite myriad difficulties and seemingly insolvable problems, with a special tribute to our fearless leaders Marty Breidenbach and Charlie Baltay.

I personally thank my thesis advisor, Uriel Nauenberg, for his patience, reading through my entire thesis many times, as well as for his encouragement to work through all the drab algebra - it built character.

I thank the whole Colorado gang, in particular Greg Baranko for his countless invaluable and constructive suggestions in writing code and analyzing the data, Nety Krishna, whom it was a pleasure to work with and get our Endcaps going, my fellow-sufferer in the quest for knowledge and glory, Cheng-Gang Fan, and John Carr, who taught me all I know about drift chambers, as well as everybody who helped in the construction of the Endcaps.

Special thanks goes to Phil Burrows, whose contributions to this thesis through innumerable conversations, discussions and proof readings have been absolutely invaluable, and to the QCD work group, including Dave Muller, Mike Strauss, Hiro Masuda, Mike Hildreth, Tom Junk and many others, who supported this work in many ways, not least by sitting through many dire presentations and practice talks of mine.

My sanity was saved by the great efforts of Richard Dubois and the whole SLAC Frisbee team who made me run my guts out and gave a whole new meaning to the observable *spin*.

For their friendship I thank Alice Bean, who introduced me to my wife, Derrell Durrett and Will Johns, who tolerate my *Swiss* way of running a household, Iris Abt, Christian Burri, Sarah Hedges, Greg Punkar and Christine Rüth.

Thanks also to Ray Cowan for his Texpertise - my thesis wouldn't look as neat - and to Douglas Adams for his good advice: **Don't Panic** (Unfortunately I can't do large friendly letters in TeX)

I'd like to thank Dave Engesen, Robert Moore and the technical crew at the CEH for their superb job of helping us install the endcap drift chambers in $S_L D$.

At the University of Colorado I'd like to thank Kathy, Norma and Vivian for taking care of the needs of us graduate students.

Thanks is not enough to my parents, Elise and Konrad Lauber, to whom I dedicate this thesis for their continuing support and for making my studies abroad possible in the first place.

And last but most I thank my wife Joy for her love and friendship and for making the years in the bay area my best ones yet.

This work was supported by the U.S. Department of Energy and the U.S. taxpayers.

CONTENTS

CHAPTER

TABLES

FIGURES

CHAPTER 1

QCD PROCESSES IN e^+e^- ANNIHILATION

1.1 Introduction

The operation of e^+e^-colliders at the Z^0 resonance provides an ideal testing ground for the Standard Model, both in the electroweak and in the strong sectors. Whereas tests of the electroweak model typically aim at high precision and compare to the accurate calculations of the Electro-Weak theory, the Quantum Chromodynamic (QCD) aspects, the non-Abelian gauge theory of the strong interactions, are rather less precise. Even in the large momentum transfer regime, where perturbative calculations can be used to describe jet production, the strong coupling is still large enough that as yet uncalculated higher order corrections could well shift current theoretical predictions significantly. Furthermore, the comparison with perturbative QCD predictions of physical observables with data relies on non-perturbative hadronization models. A relatively small experimental data sample is therefore sufficient for measurements with statistical errors comparable to the theoretical uncertainties. Within the framework of this theory, hadronic decays of the Z^0 are associated with the production of quarks and gluons, which subsequently materialize into jets of hadrons. The relative production rates of multijet events are determined by the value of the strong coupling, α_s, which, because QCD is a non-Abelian gauge theory, is expected to decrease with increasing energy.

In this thesis the relative production rates of multijet hadronic final states as observed with the SLC Large Detector (SLD) at the Stanford Linear Collider, SLC, are presented and a value for the strong coupling, α_s, determined.

1.2 The Z^0 Resonance

To lowest order in perturbative E-W theory, two fundamental processes contribute to the electron-positron annihilation into fermions $e^+e^- \rightarrow f\bar{f}$, where $f = e, \mu, \tau, \nu_e, \nu_\mu, \nu_\tau, u, d, s, c, b$: the exchange of a photon, the mediating boson of the electromagnetic interaction and the exchange of a Z^0, the neutral mediating vector boson of the weak interactions (Fig. 1.1).

The differential cross section is proportional to the square of the sum of the invariant amplitudes $|\mathcal{M}_{em} + \mathcal{M}_{weak}|^2$ of these two processes. In e^+e^-annihilations with center of mass energies near the mass of the Z^0, $\sqrt{s} \approx M_Z$, the weak term dominates over the electromagnetic one, forming a resonance near $\sqrt{s} = M_Z$ and with a width Γ_Z (Fig. 1.2).

Experiments preformed at SLAC and CERN[1]have measured the mass and the width of the Z^0:

$$\begin{aligned} M_Z &= 91.172 \pm 0.009\ GeV/c^2 \\ \Gamma_Z &= 2.498 \pm 0.0017\ GeV/c^2 \end{aligned} \tag{1.1}$$

At the center of mass energy $\sqrt{s} = M_z$, $\sigma_{\text{weak}}/\sigma_{\text{el.mag}} \approx 1100$, and also, the interference term of the cross section vanishes. Neglecting terms proportional to the initial and final state fermion mass, and with v_e, a_e, v_f and a_f being the vector and axial vector couplings for the incoming electrons and the outgoing fermions respectively, one can write the cross section in a simplified form:

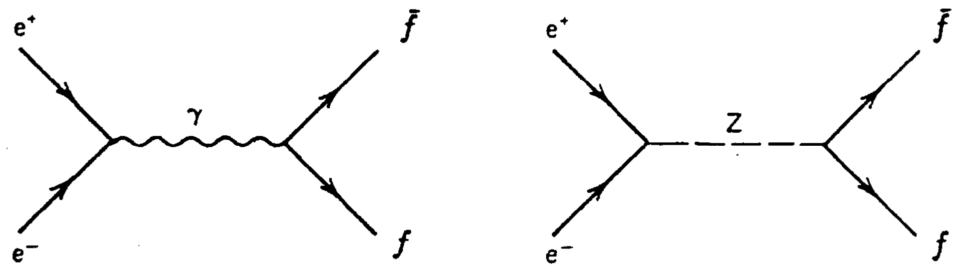

Figure 1.1 The fundamental diagrams for $e^+e^- \rightarrow \gamma/Z^0 \rightarrow f\bar{f}$

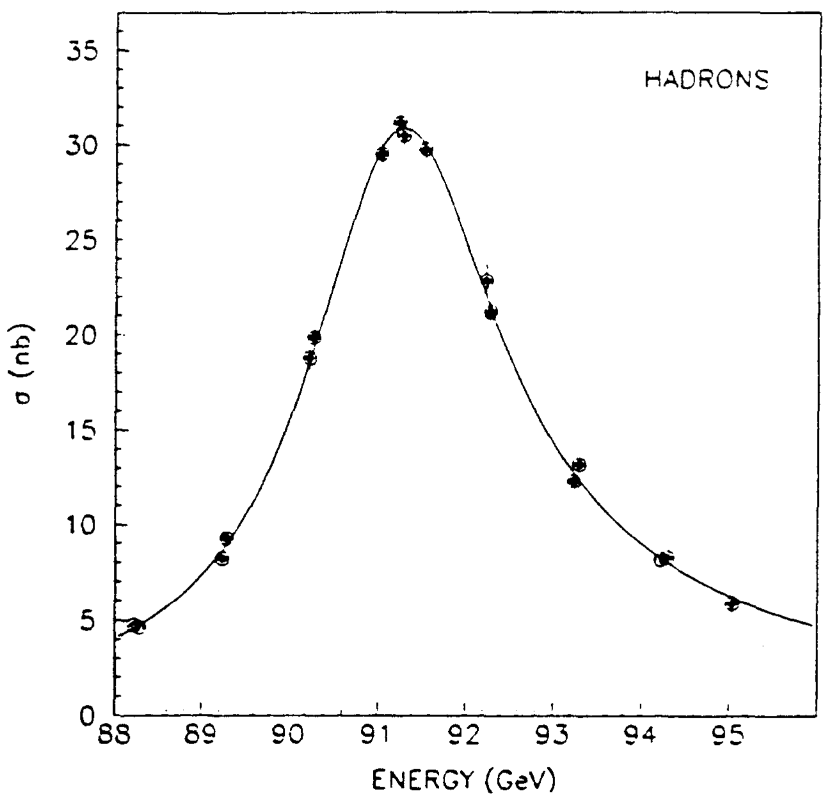

Figure 1.2 The e^+e^-annihilation cross section as a function of center-of-mass energy: the Z^0 resonance.[1] To get the total hadronic cross section, the measured cross section has to be corrected for effects of initial state radiation to give $\sigma^0_{had} = 41.8$nb at the Z^0 peak.

$$\frac{d\sigma}{d\cos\vartheta} = \frac{\pi\alpha^2}{2}\frac{s}{(s-M_Z^2)^2+\Gamma_Z^2 M_Z^2}\left[(v_e^2+a_e^2)(v_f^2+a_f^2)\right] \times\left[(1+\cos^2\vartheta)+8\cos\vartheta\frac{v_e a_e}{v_e^2+a_e^2}\frac{v_f a_f}{v_f^2+a_f^2}\right] \tag{1.2}$$

A detailed derivation of this formula is given in the Appendix. Integrated over the $\cos\vartheta$ this gives a total hadronic cross section $\sigma^0_{had} = 41.8$nb and $\sigma^0_{lept} = 2.0$nb for each of the three charged leptons, compared to the purely electromagnetic contribution to the total hadronic cross section of $\sigma^{em}_{had} = 0.038$nb.

1.3 Quantum Chromodynamics

QCD is the theory of quarks and gluons and their interactions, called the *strong* interactions. The quarks were first postulated by Gell-Mann and Zweig in 1964[2] as a computational device to explain the spectra of mesons and baryons in terms of bound $q\bar{q}$ and qqq states respectively. Quarks were defined to be spin-$^1\!/_2$ fermions and carry fractional electrical charge of $\pm{}^1\!/_3e$ or $\pm{}^2\!/_3e$, where e is the charge of the electron. They possess the quantum number flavor, $f = u, d, s$, (later more flavors, $f = c, b, t$, needed to be added to explain hadrons with higher masses discovered in experiments). The principle of Fermi-Dirac statistics dictates that fermions with identical quantum states cannot co-exist in a bound state. To explain states such as the $\Omega^-(= s\uparrow s\uparrow s\uparrow)$, which had been experimentally verified, another quantum number, color, $c = r, b, g$, was introduced. The number of colors N_c can be determined by experiment. To lowest order in QCD the ratio of hadronic to muon cross section in e^+e^-annihilations is:

$$R \equiv \frac{\sigma(e^+e^- \to \text{hadrons})}{(e^+e^- \to \mu^+\mu^-)} = N_c \sum_f q_f^2 \tag{1.3}$$

where q_f is the charge of the quark of flavor f and the sum is over all flavors whose masses are low enough that they could be produced at the given annihilation energy. At the Z^0 energy this excludes the top quark. A multitude of experiments preformed at various center-of-mass energies have shown results that are in excellent agreement with $N_c = 3$. The first direct evidence of quarks came from the Nobel prize-winning experiment at SLAC in 1968 which showed that in electron-nucleon scattering at high momentum transfer the electron scatters from quasi-free pointlike particles carrying roughly one third of the nucleon energy. The subsequent discoveries of the Ψ and Υ particles introduced two new quark flavors, the c and b. Powerful theoretical arguments suggest the existence of a sixth flavor, t, and measurements of loop corrections predict the mass of the *top* quark to lie in the range of $120 - 180$ GeV, out of the reach of presently existing e^+e^-colliders but within reach of Fermilab's $p\bar{p}$ collider.

Calculating physical quantities such as cross sections to higher order in perturbative QCD leads to infinitely large terms. To avoid these, QCD must be renormalized, absorbing these infinite terms into the basic constants of the theory, such as couplings and masses.[3] One prerequisite of the renormalizability of the theory is the invariance under local gauge transformation. This severely restricts the ways in which quarks can interact with each other. The intermediate bosons of the strong interactions are called *gluons*, which form a color octet in the adjoint representation. Because of color, the strong forces transmitted by gluons differ from the electromagnetic forces transmitted by photons. Gluons carry two labels, one color and one anticolor, such that color is conserved at each quark-quark-gluon vertex. Because gluons carry color they can couple directly to other gluons whereas photons cannot couple directly to photons since they are uncharged. There are three fundamental vertices in the theory: qqg, ggg and gggg. The latter, a four-gluon vertex does not have any major experimental consequences so far, but for the renormalizability of the theory its presence is essential.

A very important implication of the existence of this direct coupling of gluons is that of *color screening*. In quantum field theory a single electron is surrounded by a "cloud" of virtual photons which are continually emitted and reabsorbed by the electron. Some of these photons convert into a virtual e^+e^- pair. And, because opposite charges attract, the positrons will preferentially be closer to the electron. The charge of the electron is thus screened. Therefore, when measuring the charge of the electron or the strength of the electromagnetic force, the result depends on the distance scale at which the charge is probed, i.e. the closer one approaches the electron, the larger is the charge one measures.

A quark exhibits a similar behavior by emitting and absorbing gluons. The emitted gluons can then annihilate into $q\bar{q}$ pairs, but, due to the direct gluon-gluon interactions, also into gluon pairs. The gluons, themselves carriers of color, also spread out the effective color charge of the quark. But the effect is just opposite from the result of quantum electrodynamics: a quark carrying a red color charge, for instance, is preferentially surrounded by other red charges which has the effect of $anti-screening$ of the color charge. By moving closer to the original red charge we penetrate the sphere of surrounding red charge and the amount of red charge measured decreases. This is referred to by the name *asymptotic freedom*, i.e. two quarks interact through a color field of reduced strength at very small separations, and approach a state where they behave as essentially free, noninteracting particles. On the other hand, for larger separations of the quarks, the effect of anti-screening is known as *color confinement*. As two quarks move away from each other, the color field between them increases in strength. The most striking consequence of color confinement is that no experiment has "seen" color, nor the fractional charge of a single quark. Theory and experiment suggest that only colorless states are allowed in the form of physical hadrons, i.e. bound states of quarks and antiquarks (mesons) or triplets of quarks (baryons).

This dependence of the strong interaction on the energy scale, called the "running coupling constant", can be expressed in an analogous way as in QED:

$$\alpha_s(Q^2) = \frac{\alpha_s(\mu^2)}{1 + \frac{\alpha_s(\mu^2)}{12\pi}(33 - 2n_f)\ln(Q^2/\mu^2)}, \tag{1.4}$$

with the only difference from QED being the + sign in the denominator and the term $(33 - 2n_f)$, arising from the extra gluon self-interactions. n_f is the number of quark flavors involved in the process, which is taken to be 5 at the Z^0 scale. One parameter, μ, remains as a relic from the renormalization. From eq. 1.4 we see that at sufficiently low Q^2, the effective coupling will become large, just as we expected from *confinement*. It is customary to denote the Q^2 scale at which this happens by Λ^2,[5] where

$$\Lambda^2 = \mu^2 \exp\left[\frac{-12\pi}{(33 - 2n_f)\alpha_s(\mu^2)}\right]. \tag{1.5}$$

Eq. 1.4 can then be written in the simpler form. To first order:

$$\alpha_s(Q^2) = \frac{12\pi}{(33 - 2n_f)\ln(Q^2/\Lambda^2)}. \tag{1.6}$$

As a consequence of the running of the strong coupling α_s it is possible to use perturbative calculations for theoretical predictions in the high momentum-transfer region $Q^2 \gg \Lambda^2$, where α_s is small. Hence, processes like $Z^0 \to q\bar{q}$ and $Z^0 \to q\bar{q}g$ can be calculated fairly accurately in this limit. However, this procedure breaks down for 'soft', low $Q^2 \sim \Lambda^2$ processes which are dominant in the transition from quarks to hadrons, called fragmentation or hadronization. Thus, we can think of Λ as marking the boundary between a world of quasi-free quarks and gluons, and the world of hadrons. The value of Λ is not predicted by QCD; it is a free parameter to be determined by experiment. It is expected to be of the order of a typical hadronic mass.

1.4 Matrix Elements

The way to calculate the hadronic cross sections and jet rates in perturbative QCD is to determine the amplitude of every Feynman diagram to increasing order in α_s. The amplitudes are then added and squared. To $\mathcal{O}(\alpha_s)$ only three graphs contribute to the cross section: $e^+e^- \to q\bar{q}$ and $e^+e^- \to q\bar{q}g$ (Fig. 1.3a and Fig. 1.4). No four-parton final states contribute at this order. The matrix element for three massless final state partons is conveniently given in terms of scaled energy variables in the center-of-mass frame of the event [6]

$$\frac{1}{\sigma_0}\frac{d\sigma}{dx_1 dx_2} = \frac{\alpha_s}{2\pi}C_F\frac{x_1^2 + x_2^2}{(1-x_1)(1-x_2)} \tag{1.7}$$

with $x_i = 2E_i/\sqrt{s}$, the parton energy fraction in the center-of-mass frame. σ_0 is the leading order or Born cross section of the reaction.

From formula 1.7 we see that the 3-parton cross section is directly proportional to α_s. Studying the 3-jet final states in Z^0 decays therefore gives us a very intuitive way to measure α_s.

Many more Feynman diagrams have to be considered in second order perturbative QCD and the calculations become much more complex. Among

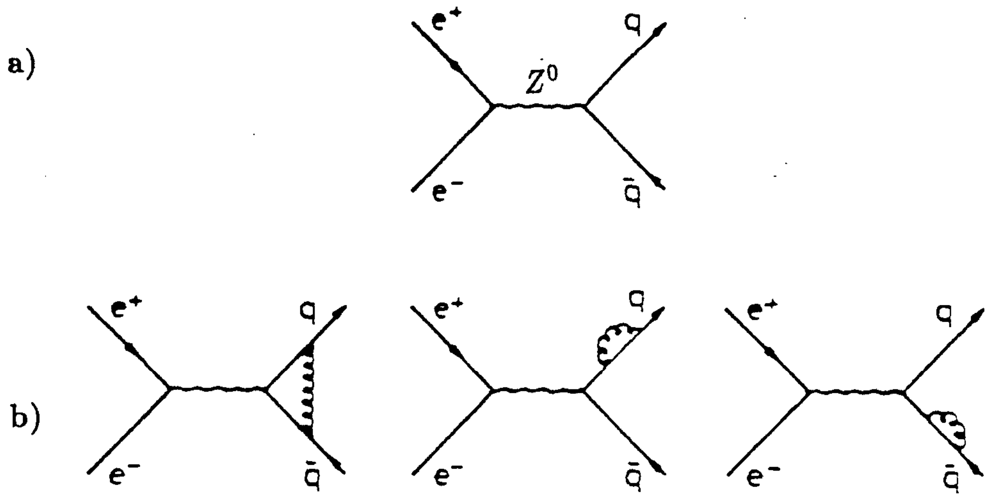

Figure 1.3 Feynman diagrams for $e^+e^- \rightarrow q\bar{q}$ and $\mathcal{O}(\alpha_s^2)$ corrections to the fundamental process.

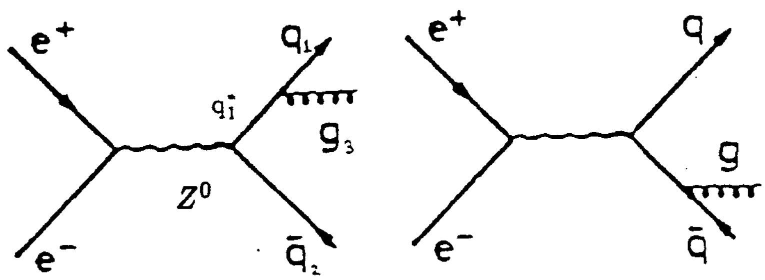

Figure 1.4 $\mathcal{O}(\alpha_s)$ Feynman diagrams for $e^+e^- \rightarrow q\bar{q}g$

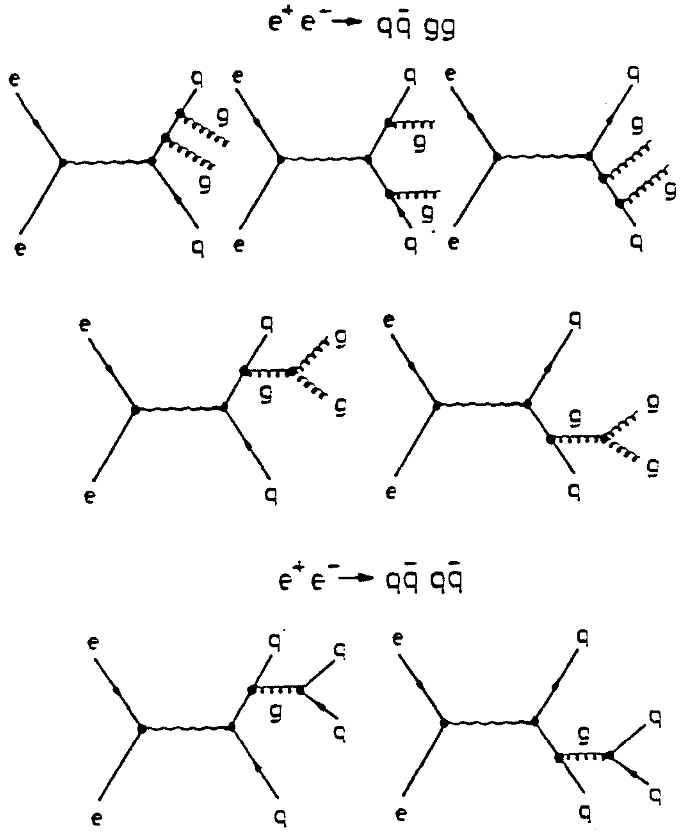

Figure 1.5 $\mathcal{O}(\alpha_s^2)$ Feynman diagrams $e^+e^- \to$ 4-parton final state

higher order radiative corrections, loop corrections and vertex corrections there are also two new event types, which must be included: $e^+e^- \to q\bar{q}gg$ and $e^+e^- \to q\bar{q}q'\bar{q}'$, giving rise to four-parton final states shown in Figure 1.5. The four-jet cross section has been calculated by several groups[7] [8] [9] [10], which basically agree among each other as to the rate of these processes.

The diagrams for the radiative corrections in Fig.1.3b are 'ultra violet' divergent, i.e. the integral over the virtual gluon momenta k diverge for $k \to \infty$. But the divergences in the amplidudes have opposite sign and cancel out when summed. The radiative corrections also diverges for $x_1 \to 0$ or $x_2 \to 0$, an 'infrared' divergence, which occurs when a gluon is radiated collinearly to any of the quarks. This divergence can be avoided by applying a resolution cut below which two partons are irresolvable. Commonly, the scaled invariant mass $y_{ij} = m_{ij}^2/s$ is used as a criterion. If $y_{ij} < y_{min}$ a radiated gluon cannot be observed separately from the quark which it was emitted from. The cross sections are only calculated in the region $y > y_{min}$. For $y_{min} = 0.01$ and α_s=0.12 the 2:3:4 parton composition is approximately 11%:77%:12% in full second order QCD.

In the second order calculation, α_s takes the following form as quoted by the Particle Data Group[11]

$$\alpha_s^{(2)}(Q^2) = \frac{12\pi}{(33-2n_f)\ln(Q^2/\Lambda^2)}\left[1 - 6\frac{153-19n_f}{(33-2n_f)^2}\frac{\ln(\ln(Q^2/\Lambda^2))}{\ln(Q^2/\Lambda^2)}\right] \quad (1.8)$$

A few years ago, the five-jet Born cross section was calculated.[12] [13] The calculations are very difficult and the resulting formulas are rather lengthy and no loop corrections have been made available yet. The actual 5-jet rate is very small. If only the regions of y_{ij} are considered in the measurements of α_s where the 5-jet rate is smaller than the errors introduced by the experiment, third order QCD terms can be neglected.

1.5 Jets

It is a common property of multi-hadron production in all kinds of reactions that the final particles are not distributed uniformly in phase space. Rather they are collimated along some distinguished axes in the direction of the original parton and are bundled into rather small regions, called jets. The exact definition of jets is discussed in details in chapter 4.3. The existence of such jets had been predicted by theory as a consequence of confinement,[14] but was first observed in e^+e^-annihilations by the Mark I collaboration in 1975.[15] Whereas their data at center of mass energies of $\sqrt{s} \sim 3-7$ GeV required a thorough statistical comparison to phase space models to establish the existence of jets, they are a very obvious phenomenon at higher energies (Fig. 1.6). Corresponding to the underlying elementary process as described by the Feynman diagrams in figures 1.4 and 1.5 events can be found with a 3-jet or 4-jet structures shown in figures 1.7. and 1.8.

Thus the global structure of hadronic events in e^+e^-–collisions is well understood in terms of hard partons (quarks and gluons) and QCD. How these partons convert into hadrons is less obvious and cannot be calculated from first principles. Rather, it is an active field of experimental research aimed at collecting information about the structure of jets, finding regularities and thus allowing one to penetrate deeper into the understanding of hadronization.

Much effort has gone into calculations of higher order QCD corrections to jet cross sections. In particular, full second order calculations have been made by G. Kramer and B. Lampe[16] as well as by Z. Kunszt and B.R. Nason.[17] To $\mathcal{O}(\alpha_s^2)$ the fraction of three jet events can be parametrized in the form

$$\begin{aligned}\frac{\sigma_{3jet}(y_{cut})}{\sigma_0} =& \frac{\alpha_s(Q)}{2\pi}A_3(y_{cut}) \\ &+ \left(\frac{\alpha_s(Q)}{2\pi}\right)^2 \left[A_3(y_{cut})2\pi b_0 log(Q^2/s) + B_3(y_{cut})\right],\end{aligned} \tag{1.9}$$

while the number of four jet events can be given as

$$\frac{\sigma_{4jet}(y_{cut})}{\sigma_0} = \left(\frac{\alpha_s(Q)}{2\pi}\right)^2 A_4(y_{cut}). \tag{1.10}$$

where y_{cut} is a jet resolution parameter, described in detail in section 4.3. σ_0 is the leading order or Born cross section of the reaction. There is no analytically closed expression for the coefficients A_3, B_3 and A_4, they are the

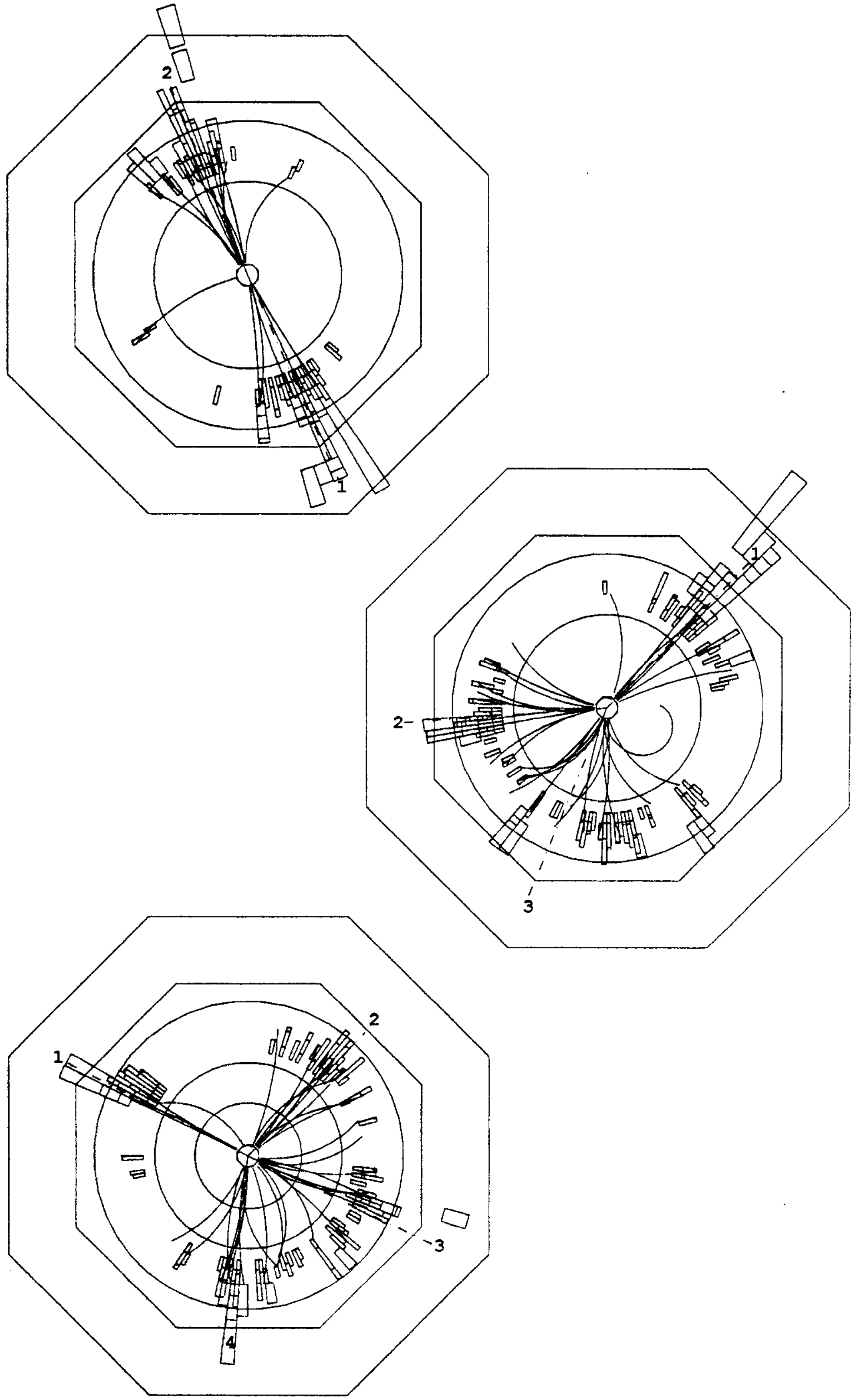

Figure 1.6–1.8 2-jet, 3-jet and 4-jet events seen with the SLD detector

result of lengthy numerical integrations and are tabulated.[17] [18] [19] In performing such calculations various divergencies arise, and these must be regulated in a consistent way. This requires a particular renormalization scheme. The most commonly used is the modified minimal subtraction ($\overline{MS}$) scheme. This involves counting momentum integrals from 4 to $4-2\epsilon$ dimensions and then subtracting off the resulting $1/\epsilon$ poles.[21] [22]

To order $\mathcal{O}(\alpha_s^2)$ only two, three and four jet cross sections contribute. Therefore the two jet cross section can be written as

$$\sigma_{2jet} = \sigma_0 - \sigma_{3jet} - \sigma_{4jet}. \tag{1.11}$$

The multi jet cross sections are usually calculated with respect to the tree-level Born cross section σ_0 while in the experiment we measure the total cross section σ_{tot}. The higher order corrections to the Born cross section are given by the formula[17]

$$\frac{\sigma_{tot}}{\sigma_0} = 1 + \frac{\alpha_s}{\pi} + (1.986 - 0.115 n_f)\left(\frac{\alpha_s}{\pi}\right)^2 + \cdots \tag{1.12}$$

with the number of flavors, $n_f = 5$ at the Z^0 energy scale.

1.6 Optimized Perturbation Theory

The second order virtual corrections to the three-jet rate are large compared to the first order terms. It is therefore possible that the third order corrections to the four-jet rate are quite large as well. Indeed, the experimental four-jet rate is much larger than second order predicts, if α_s is determined based on the three-jet rate.[23] Since full $\mathcal{O}(\alpha_s^3)$ calculations are not yet available, one has tried to minimize higher order contributions by a suitable choice of the renormalization scale. This is equivalent to a different choice for the Q^2 scale in α_s, a scale which is not unambiguous in finite order. If the 3-jet rate R_3 is calculated to infinite order, the renormalization group asserts that no dependence can remain on the original expansion parameter. Calculated to infinite order, α_s can therefore not depend on a particular choice of Q^2.

On physical grounds it can be argued that the scale for the emission of a gluon should be related to the kinematics of this emission. Given that most gluons are rather soft, the scale must thus be smaller than the standard value E_{cm}^2, i.e. $Q^2 = fE_{cm}^2$, with $f < 1$. Since α_s is increased by a reduction of the Q^2 scale, the $\mathcal{O}(\alpha_s)$ 3-jet rate would then be increased, and so would the number of 4-jet events. The loop corrections depend on the Q^2 scale also and compensate the changes above by giving a larger negative contribution to the three-jet rate.

If the one loop corrections to the Born term cross section are already known, several different prescriptions have been suggested by theorists for selecting which scale to use for a process, such as the BLM[24] method, which is based on absorbing terms which depend upon the number of active fermions n_f, into the strong coupling α_s. The PMS (principle of minimal sensitivity)[25] requires that the first derivative of the physical observable with respect to the scale Q^2 vanishes, since the true result is completely independent of Q^2. A more relaxed condition is required by the MSD method,[26] which demands that the observable has a moderate scale dependence but the first derivative of the observable with respect to Q^2 is minimal and hence the second derivative should vanish. FAC (fastest apparent convergence)[27] chooses a scale such that the next to leading order terms vanish in the second order calculations. All schemes are aiming at optimizing the perturbation theory and minimizing the uncalculated higher order corrections to keep the theoretical errors as small as possible. They all have in common that they strongly suggest the correct scale to be smaller than the naive $Q^2 = M_Z^2$ one and the larger the relative size of the second order term over the first order term the smaller the preferred scale.

When measuring the strong coupling α_s the experimentalist is thus faced with the problem of choosing the appropriate scale f. A possible choice of scale is $f = 1$, i.e. $Q^2 = E_{cm}^2$. Another possibility is to treat f as a free parameter to be determined along with $\Lambda_{\overline{MS}}$ from the data. Experimentalists[28] have used both scales to determine α_s and quoted the central value as their result and the difference of the two as a theoretical uncertainty of the measurement.

1.7 Hadronization and Monte Carlo Simulation

The schematic structure of a multihadronic event in e^+e^- annihilation is shown in Figure 1.9. In a first phase, an e^+e^- pair annihilates into a virtual γ/Z^0 state, which decays into a primary quark-antiquark pair $q\bar{q}$. Before the annihilation, initial state QED Bremsstrahlung may occur, so that the mass of the hadronic final state is reduced from the total center-of-mass energy of the process.

In the second phase, the initial $q\bar{q}$ pair may radiate gluons g, which in their turn may radiate. While the primary $q\bar{q}$ production is given by electroweak perturbation theory, strong perturbation theory must be used to describe this second stage.

In the third phase, the colored partons fragment into a number of colorless hadrons. In principle this process can be described by QCD as well, but for reasons described in Chapter 1.2, perturbation theory cannot be applied. Therefore we have to aid ourselves with phenomenological models which we

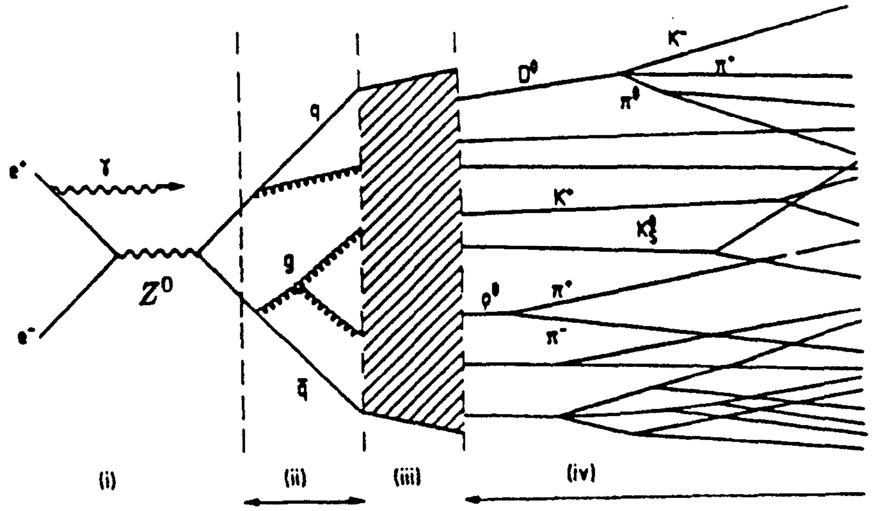

Figure 1.9 Schematic illustration of an e^+e^- annihilation event

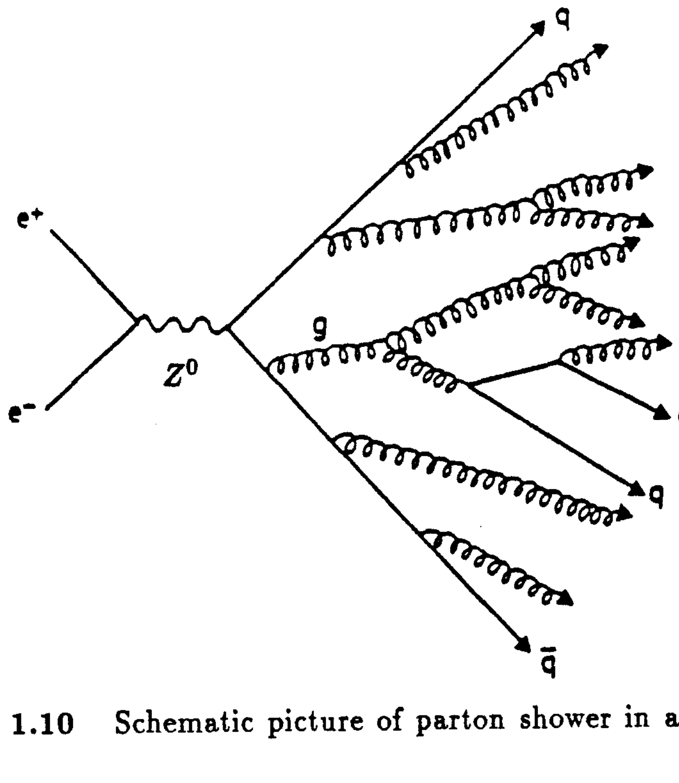

Figure 1.10 Schematic picture of parton shower in an e^+e^- annihilation event

tune with experimental findings.

In a fourth phase, unstable hadrons decay into the experimentally observable particles. This includes everything from $\pi^0 \to \gamma\gamma$ to long decay chains of charm and bottom hadrons. Whereas the qualitative features of these decays usually are well known, little quantitative understanding exists. Instead the main input here comes from experimentally determined branching ratios.

Given the complexity of the problems described, purely analytical techniques are of limited usefulness for physics studies at SLD. Therefore the Monte Carlo simulation of complete hadronic events constitutes one of the main tools for improving our understanding of QCD. The use of Monte Carlo methods, i.e. the selection of variables according to rules which contain random numbers, is well suited to describe nature, and in addition allows the subdivision of a complex task into more manageable subtasks, such as the generation of the partons, hadronization, decaying of unstable particles and subsequently simulating the finite resolution and acceptance of the detector.

1.7.1 Parton Showers

The Parton Shower model (PS) of hadronization is based on the leading logarithm approximation (LLA). In this approach, only the leading logarithmic terms in the perturbative expansion of the qqg and ggg cross sections are kept. Subleading corrections, which are down in order by factors of $\ln Q^2$ or by powers of $1/Q^2$ are neglected. This is a big simplification over the matrix element scheme, which grows enormously complicated beyond $\mathcal{O}(\alpha_s^2)$ due to the growing number of Feynman diagrams contributing to the calculation. Parton shower algorithms are based on an iterative use of the basic branchings $q \to qg$, $g \to gg$ and $g \to q\bar{q}$ depicted in Figure 1.10. The probability that a branching $a \to bc$ will occur during a small change dt of the evolution parameter $t = \ln(Q^2/\Lambda^2)$ is given by the Altarelli-Parisi equations.[5] The Altarelli-Parisi splitting kernel P for the branching $a \to bc$, takes the form

$$\frac{dP_{a\to bc}}{dt} = \int dz \frac{\alpha_s(Q^2)}{2\pi} P_{a\to bc}(z) \tag{1.13}$$

with the solutions

$$\begin{aligned} P_{q\to qg} &= \frac{4}{3}\frac{1+z^2}{1-z}, \\ P_{g\to gg} &= \frac{6(1-z(1-z))^2}{z(1-z)}, \\ P_{g\to q\bar{q}} &= \frac{1}{2}(z^2+(1-z)^2). \end{aligned} \tag{1.14}$$

The z variable specifies the sharing of four-momentum between the daughters, with daughter b taking z and daughter c taking $1-z$. The probability that no branching occurs between t and a lower cutoff t_{min} is given by the

$$\mathcal{P}(t_{min}, t) = exp\left\{ -\int_{t_{min}}^{t} dt' \frac{\alpha_s(Q^2)}{2\pi} P_{a\to bc}(z) \right\} \tag{1.15}$$

where $t_{min} = \ln(Q_0^2/\Lambda^2)$ and Q_0 is the lower cutoff, below which partons are not allowed to radiate. This is nothing but the exponential decay law of radioactive decays, with a Q-dependent decay probability. Once the parton a has branched, the products b and c are allowed to branch with a successively decreasing Q^2. The branching is stopped when $Q^2 < Q_0^2$. The total cross section of the shower is proportional to the product of probability of each individual branching and no interference between branchings are taken into account. The probabilistic branching in the LLA picture is particularly well suited for implementation in Monte Carlo simulations. Only two parameters are used to control the parton shower evolution: the cutoff Q_0 and the QCD scale Λ_{LLA}. It should be noted that this Λ_{LLA} is not the same as the $\Lambda_{\overline{MS}}$ described in section 1.6. $\Lambda_{\overline{MS}}$ is a parameter from a finite order calculation within a certain renormalization scheme, whereas Λ_{LLA} is a parameter in the parton shower model approximating the Λ from an infinite order calculation.

Since the neglected sub-leading terms are not necessarily small, attempts have been made to improve the PS model by going to next-to-leading-log approximations (NLL),[29] introducing $1 \rightarrow 3$ branchings. It is not clear, though, that this improves the agreement of the model with the experimental data.

1.7.2 String Fragmentation and the JETSET Model

A number of models exist for the third phase of hadronization. Being models, none of them can lay claims to being 'correct', but rather aim at a good representation of the existing data. Three main schools are usually distinguished:

1) String Fragmentation (SF)
2) Cluster Fragmentation (CF)
3) Independent Fragmentation (IF)

The first example of a string fragmentation scheme was given by Artru and Mennessier[30] and the model was then much expanded and refined by the Lund group[31] and used in their JETSET Monte Carlo programs.

The starting point of string fragmentation is the concept of linear confinement, best described for a back-to-back $q\bar{q}$ two jet event. As the partons move apart, a color flux tube is being stretched between them (Fig. 1.11). The color field in the tube is uniform along its length giving rise to a linearly rising potential $E(r) \sim \kappa r$ as the quarks separate, where r is the separation between the quarks and κ is a string constant, i.e. the amount of energy per unit length κ can crudely be estimated to be $\kappa \approx 1\mathrm{GeV/fm}$ or about a hadron

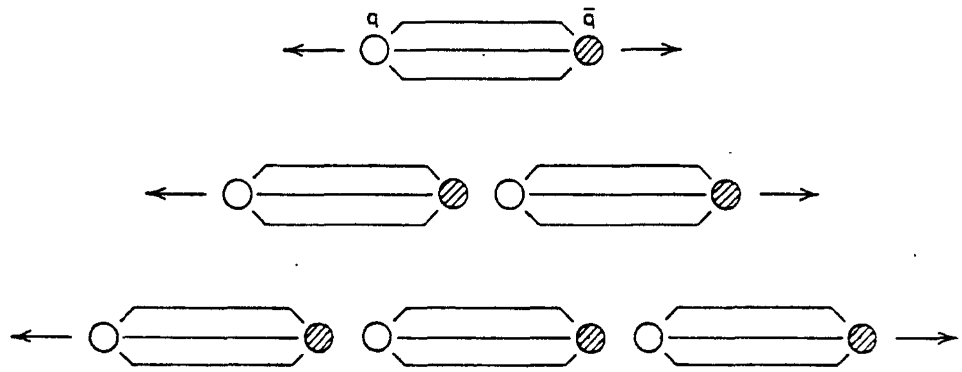

Figure 1.11 A color tube stretching from a q to a $\bar{q}$.[5] As the q and the $\bar{q}$ separate and the potential energy in the the tube becomes larger, a secondary pair $q'\bar{q}'$ get created with the probability $f(z)$.

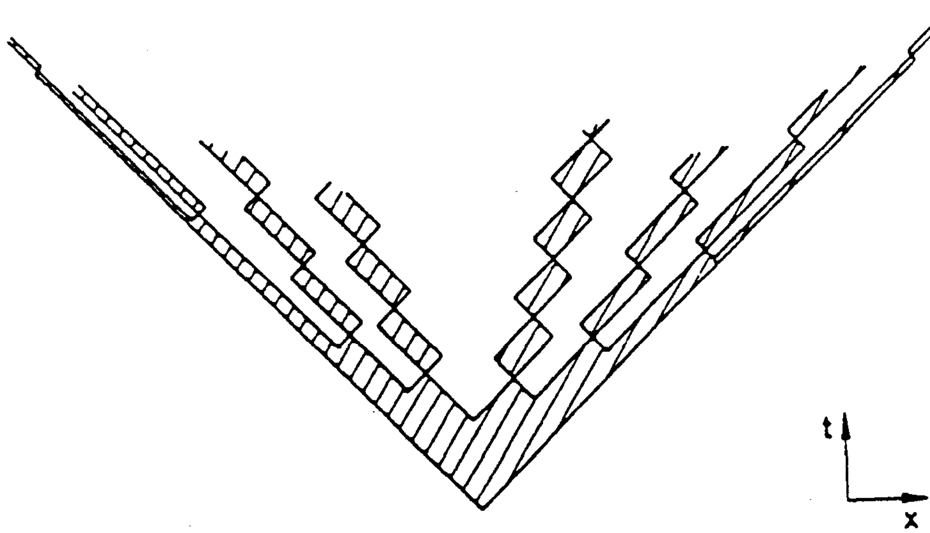

Figure 1.12 Breaking of a string in the Lund approach, schematically drawn for one space dimention x and time t. Massless quarks are moving along the light cone, corresponding to diagonal lines in the diagram. Hatched areas indicate regions of nonvanishing color field. At every vertex another $q\bar{q}$ pair is created. The quark from one break combines with the antiquark from the adjacent one to form a meson.

mass per hadron diameter.[3]

When the potential energy stored in the string becomes large enough, the string breaks according to the probability $f(z)$, forming a new quark pair $q'\bar{q}'$, so the system now contains two color singlets $q\bar{q}'$ and $q'\bar{q}$. In the Lund model the strings are broken up to form hadrons, each hadron corresponding to a small piece of the original string (Fig 1.12[4]). The breakup process is stopped when only on-mass-shell hadrons remain. Quantum mechanically the $q\bar{q}$ pair that leads to the break up of the string is produced at one point and tunnels out to the 'allowed' region. The tunneling probability is a function of the quark masses m and the transverse momentum p_T and is given by[4]

$$\exp\left(-\frac{\pi m_T^2}{\kappa}\right) = \exp\left(-\frac{\pi m^2}{\kappa}\right)\exp\left(-\frac{\pi p_T^2}{\kappa}\right). \tag{1.16}$$

Because of the mass term in the exponent, this amounts to a heavy quark suppression with a relative production rate of flavors $u : d : s : c \approx 1 : 1 : 0.3 : 10^{-11}$. Hence, charm and heavier quarks are not expected to be produced in the soft fragmentation. In the Lund model the fraction z of the remaining $E + p_L$ taken by a hadron, where E and p_L are the energy and the longitudinal momentum of the hadron along the string axis, is put in the form of a probability distribution $f(z)$:

$$f(z) = z^{-1}(1-z)^a \exp\left(-\frac{bm_T^2}{z}\right) \tag{1.17}$$

The variables a and b are parameters of the model and can be tuned to best fit the experimental data. The optimized values for a and b can be different for various quark flavors and for mesons/baryons.

The model gets more complex for multiparton systems. For $q\bar{q}g$ the string is stretched from q via the g to the $\bar{q}$. The gluon is in effect a kink in the

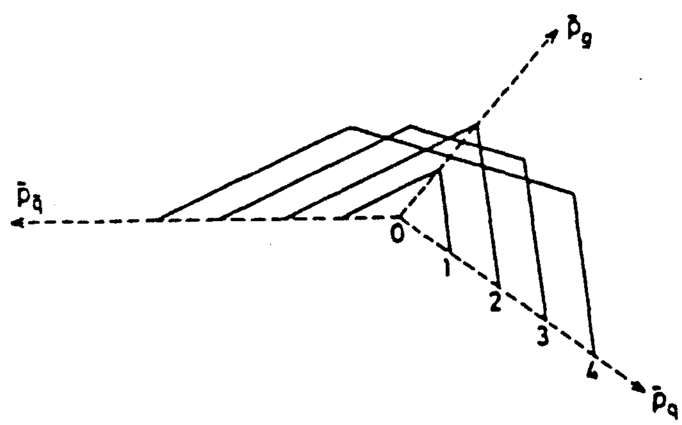

Figure 1.13 The string drawing for a 3-jet event

string, carrying energy and momentum (Fig. 1.13). As a consequence, the gluon g has two strings attached to it. The string constant κ in a string stretching from a quark to a gluon is twice the constant of a quark-quark string, because the gluon carries two color charges. The string constant is independent of the kinematic configuration: a smaller opening angle between two partons corresponds to a smaller string length drawn out per unit time, but also to an increased transverse velocity of the string piece, which gives an exactly compensating boost factor in the energy density per unit string length. This model can be expanded to higher numbers of partons. The $\mathcal{O}(\alpha_s^2)$ matrix element calculation only includes events with ≤ 4 partons, while the parton shower model can include an arbitrary number of partons.

The JETSET program ("the Lund Monte Carlo for e^+e^-annihilations")[31] is probably the most widely used simulation program for physics studies at the Z^0 resonance. Version 6.3, used in this experiment, uses $\mathcal{O}(\alpha_s^2)$ terms according to the GKS matrix element (ME) calculations generating up to 4-parton states. The parameters for the ME calculation are the QCD scale $\Lambda_{\overline{MS}}$ and the parton pair resolution cutoff y_{min} described in Section 1.5. Another option in the JETSET routine is the parton shower model (PS) described

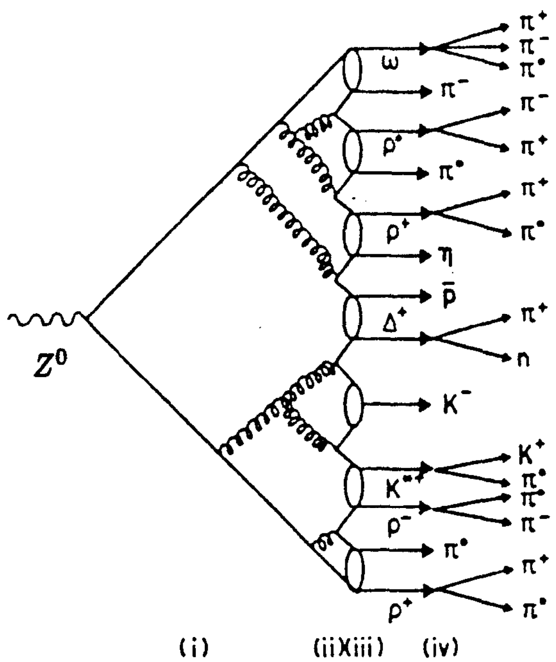

Figure 1.14 The HERWIG fragmentation model.

above. JETSET constrains the first branchings of the shower to agree with the explicit three-jet matrix element form, modifying the shower formalism in the region where the kinematical approximations involved are known to be least reliable. For a cutoff parameter value of $Q_0 = 1\text{GeV}$, JETSET yields on average 9.0 partons at the end of the parton shower, whereas the matrix element calculation has at most 4 partons in the final state. As a comparison, HERWIG,[32] described in the following section, gives 6.6 final state partons on average. All the Monte Carlo programs are tuned to yield the same number of final state hadrons after hadronization and decaying of short lived particles, as are observed in the experiment.

1.7.3 Cluster Fragmentation and the HERWIG Model

The cluster concept is simpler than a string fragmentation model. Clusters do not have any internal structure, but are only characterized by their total mass and color content. They are assumed to be the basic units from which hadrons are produced. This results in a compact description with few parameters.

In the Webber Model,[32] implemented in the HERWIG program, a parton shower calculation is used to form clusters, forcing $g \rightarrow q\bar{q}$ at the end of the shower evolution. Heavy clusters are fragmented into lighter ones and ultimately into two final state hadrons, illustrated in figure 1.14. The fragmentation is done isotropically in the cluster's restframe. Light clusters are allowed to decay into single hadrons, so as not to underestimate the rate of single particles carrying a large fraction of the total jet energy. Four-momentum is shuffled to or from nearby clusters, to achieve overall energy and momentum conservation.

1.7.4 Independent Fragmentation

As in the case of string fragmentation, the fragmentation of a jet is described iteratively. From an original quark jet q, hadrons are split off one by one, leaving behind a new jet with scaled down energy. The function $f(z)$, which describes how big a fraction z of the remaining energy is taken by the hadron, is assumed to be the same at each step, i.e. independent of remaining energy. In the independent fragmentation approach, it is assumed that the fragmentation of any system of partons can be described as an incoherent sum of independent fragmentation procedures for each parton separately.[35] [36] The process is to be carried out in the overall center-of-mass frame of the jet system, with each jet fragmentation axis given by the direction of motion of the corresponding parton in that frame. Gluons are handled by splitting the g jet into a pair of parallel q and $\bar{q}$ ones, sharing the energy according tho the Altarelli-Parisi splitting function (eq. 1.17).

CHAPTER 2

DETECTOR DESCRIPTION

An electron–positron collider is an ideal tool to produce the Z^0 boson in large numbers in a low background environment and to study its properties within the framework of the Standard Model. SLAC produced its first Z^0 particle with the linear accelerator, SLC, in May 1989. In the spring of 1991 the Mark II detector was replaced with the more versatile and powerful *SLD*.

2.1 SLC

The SLAC Linear Collider consists of a 3 km long accelerator, which accelerates both electrons and positrons in a straight line to an energy of up to 50 GeV, and two arcs which bring the beams around to the interaction point *IP* (Fig. 2.1).

In a source bunches of 7×10^{10} electrons are produced which are transported into the accelerator. Two thirds down the Linac every alternate bunch of electrons is extracted and directed onto a fixed target. The positrons from the resulting electro-magnetic shower are collected and brought back to the beginning of the Linac. After accelerating the e^+ and e^- bunches to 1.2 GeV they are transferred to two damping rings. Since the higher energetic particles loose more energy through synchrotron radiation than the lower energetic ones, this leads to a reduction in the spread in the momenta within the electron and positron bunches. Sets of quadrupole magnets are used to cool the transverse spread in the momentum (emittance). The particles then get transferred back

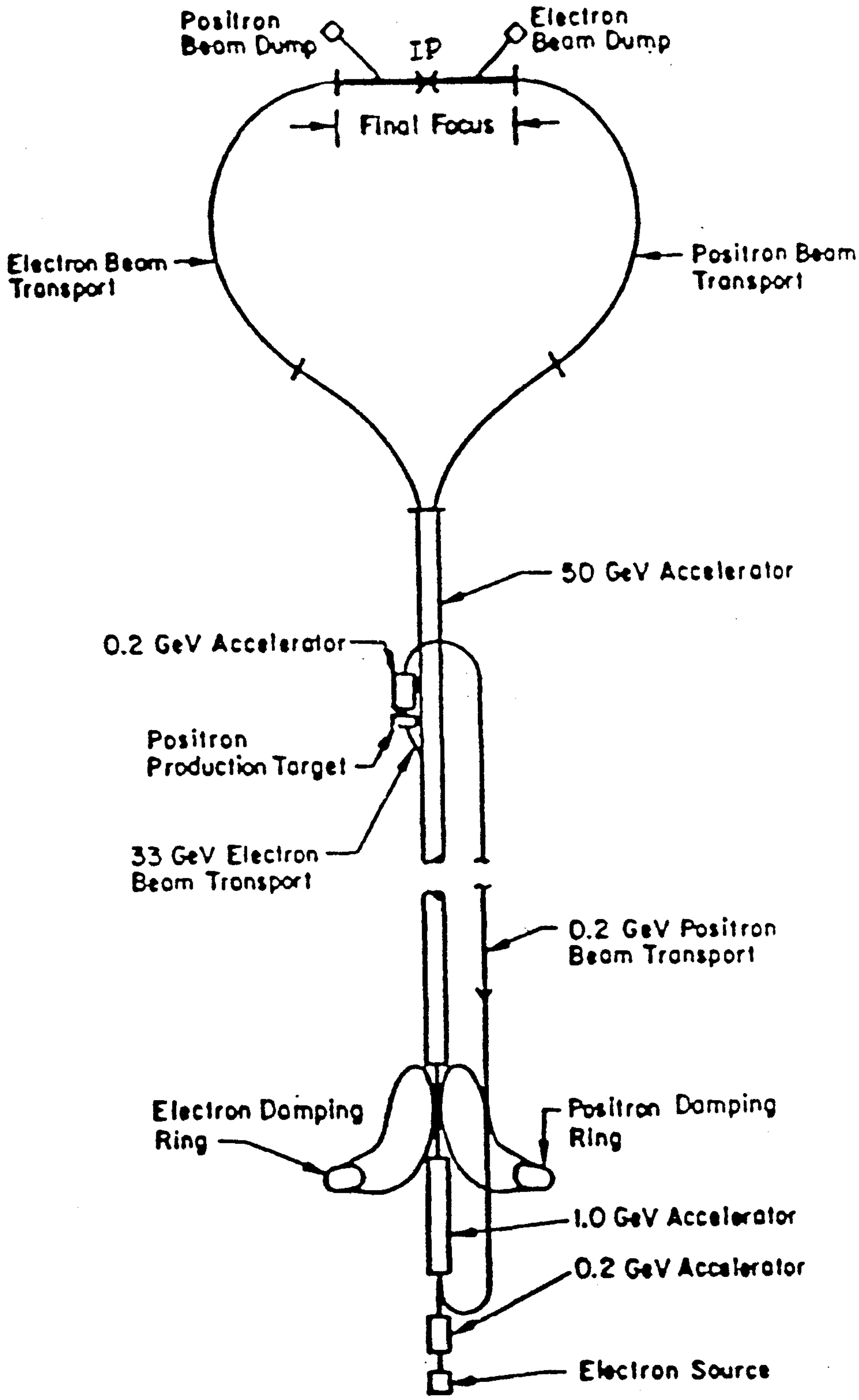

Figure 2.1 The SLAC Linear Collider is capable of colliding electrons and positrons at the center-of-mass energy of the Z^0 mass.

to the main accelerator where they are accelerated to their final energy of 46.7 GeV. At the end of the Linac, the e^+ and e^- beams are separated by a dipole magnet and transported through two arcs, loosing on average about 1 GeV of energy due to synchrotron radiation. Before the beams collide they go through a set of superconducting focusing quadrupole magnets (SCFF) which squeezes the beams to a diameter of 2μm. As the two beams intersect the oppositely charged electrons and positrons deflect each other by a very small angle. Monitors further down the beam line monitor this beam-beam deflection continually. These measurements are then used in a feedback loop to steer the beams, continuously optimizing the intersection of the two beams. After the beams pass through the interaction point (IP) they are removed from the regular beam line and directed into a beamdump.

The advantages of a linear accelerator design over a circular storage ring are the low energy loss due to synchrotron radiation and the ability to deliver longitudinally polarized beams. Since the beams are not reused, the beams can be focused more strongly before the collision, thereby increasing the luminosity. This also allows the use of a smaller beampipe, and hence, a smaller vertex detector with higher resolving power. The drawback is that the beams can only be used for one crossing while the same beams in a storage ring can be circulate for several hours at a time.

The luminosity of SLC is given by

$$\mathcal{L} = f_R \times \frac{N^+N^-}{4\pi\sigma_x\sigma_y} \tag{2.1}$$

where N^+ and N^- are the number of positrons and electrons per bunch, about 3×10^{10} for either beam. f_R is the repetition rate of the machine of $120Hz$. σ_x and σ_y are the spot size in x and y, measuring about 2μm in both directions. The luminosity of SLC for the run in the summer of 1992 was around $\mathcal{L} = 0.14 - 0.23 \times 10^{30}\mathrm{cm}^{-2}\mathrm{sec}^{-1}$ which translates to a rate of about 15-25 Z^0 event per hour for the observable (neutrino production excluded) cross section of $\sigma(e^+e^- \to f\bar{f}) = 48nb$ at the center of mass energy of 91.2 GeV.

2.2 Polarization at SLC

SLC is capable of delivering a longitudinally polarized electron beam to the Interaction Point (IP). Longitudinally polarized electrons are produced by photo-emission from a bulk gallium arsenide photocathode which is illuminated by a circularly polarized laser beam of wavelength $\lambda = 715$ nm. Presently, the polarization of the emitted electrons is typically 28%. With improved cathode material, polarization of up to 45% can be achieved. The electron helicity is changed randomly on a pulse-to-pulse basis by changing the bias voltage on a Pockels cell that is used to circularly polarize the laser beam.

A system of spin rotators rotate the polarization vector of the electrons into the vertical direction for storage in the damping ring and controls the orientation of the vectors at the end of the linac to compensate for precession in the machine's arcs. Depolarization effects in the damping rings and in the arcs reduce the net longitudinal polarization at the IP to typically 22%.

Two kinds of polarimeters are used along the electron beam to monitor the status of the polarization. A Møller polarimeter at the end of the Linac is used for diagnostic purposes. It makes use of the polarized asymmetry of the cross section in electron-electron elastic scattering in a thin iron foil which can be moved into the beam line. A Compton polarimeter is used to continually monitor the polarization of the electron beam after it has passed through the IP and before the beam is extracted. The electron beam collides with polarized photon beam that is produced by a frequency-doubled Nd:YAG laser. A diagram of the polarimeter is shown in Figure 2.2a.

The first bending magnet of the focus region is used as the analyzing magnet. The scattered electrons are dispersed horizontally and exit the vacuum system through a thin window. The two detectors consist of a nine-channel threshold Cherenkov counter and a 5-radiation-length lead radiator that is instrumented with 16 proportional tubes.

The electron beam polarization is extracted from the large asymmetry in the polarized Compton scattering cross section, σ_p, i.e. the asymmetry of the scattering cross section of longitudinally polarized electrons with left-handed and right-handed circularly polarized photons, which is defined by the following expression,[39]

$$\frac{d\sigma_p}{dE_s} = \frac{d\sigma_u}{dE_s}[1 + P_\gamma P_e A(E_s)], \tag{2.2}$$

where E_s is the energy of the scattered electron, σ_u is the unpolarized Compton scattering cross section, P_γ is the photon spin polarization, P_e is the longitudinal polarization of the electron and $A(E_s)$ is the Compton asymmetry function defined as

$$A(E_s) = \frac{(1/k - 1/k')\,[\vec{k}\cos\theta_0 + \vec{k}'] \cdot \hat{s}}{(k - k')^2/kk' + 1 + \cos^2\theta_0} \tag{2.3}$$

with $\vec{k}$ and $\vec{k}'$ being the momentum vectors of the incident and scattered photons, respectively and θ_0 the photon scattering angle. The energy dependent asymmetry measurement is shown in Fig. 2.2.b.

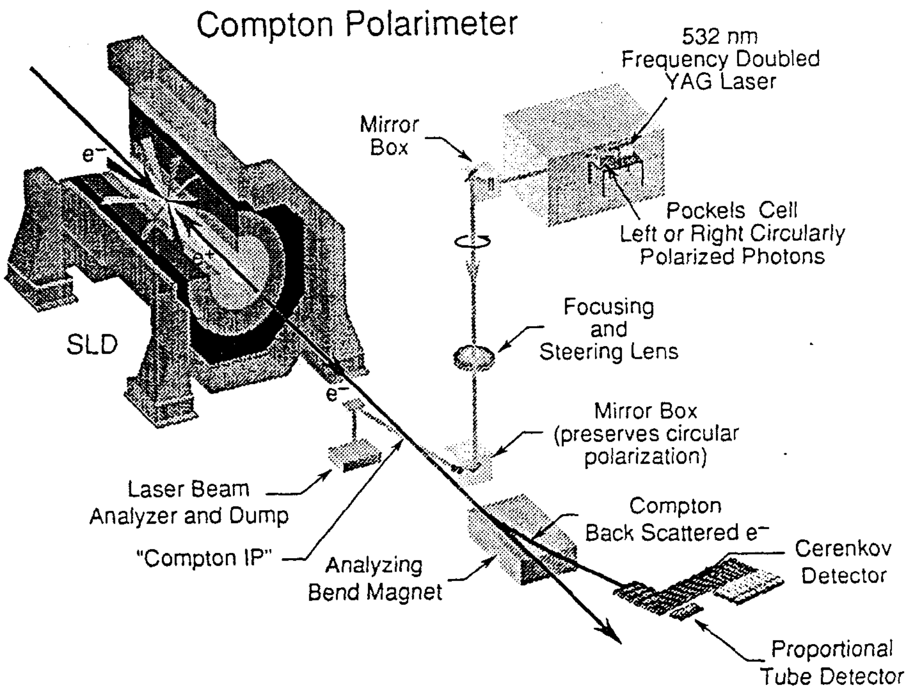

Figure 2.2.a The Compton Polarimeter provides a continual measurement of the longitudinal beam polarization.

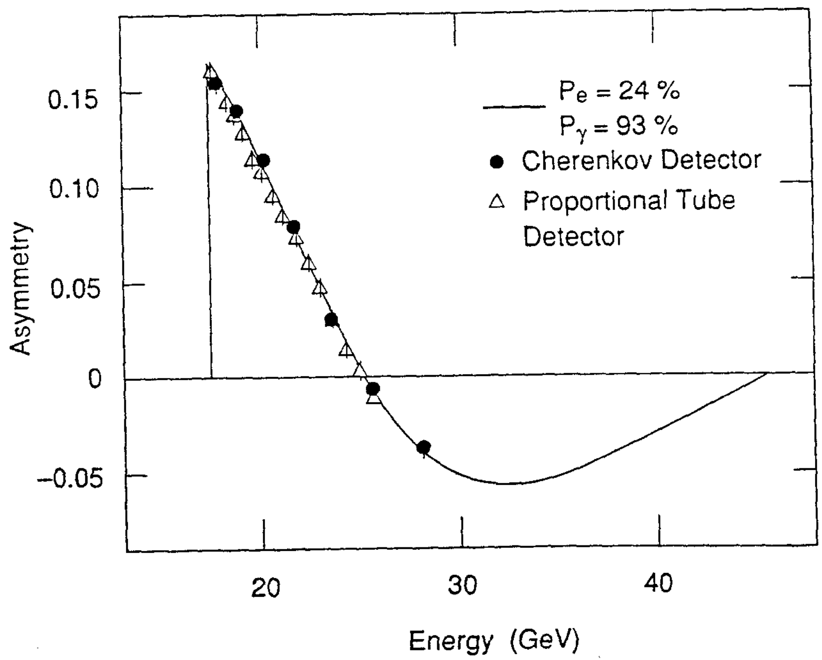

Figure 2.2.b Compton asymmetry $A(E_s)$ measured by the Compton polarimeter as a function of the energy of the scattered electron.

2.3 Overview of SLD

SLC's Large Detector (Fig. 2.3) consists of many individual detectors, which use state of the art technology, designed to study physics at the Z^0 mass energy scale.[38] SLD was built between 1986 and 1991. It is situated in a 15 m deep pit inside the collider hall that was erected around the interaction point. All detector components are contained in a 9 m diameter octagonal steal structure. Particle tracking is done with a silicon vertex detector (VXD) and a precision central drift chamber (CDC) and a set of endcap drift chambers (EDC) for low angle tracks. Particle identification is provided by a set of Cherenkov Ring Imaging Detectors ($CRID$). Calorimetry is provided by three parts: a Liquid Argon Calorimeter (LAC), measuring the electromagnetic part of the energy and 85% of the hadronic energy, a Warm Iron Calorimeter (WIC), instrumented with streamer tubes between iron absorbers, that measures the tail ends of the hadronic showers and is also capable to track the escaping muons, and a Luminosity Monitor (LUM) which measures energies deposited in the extreme forward and backward directions. All the components, except for the WIC are placed inside a magnet coil producing a 0.6 Tesla magnetic field. By measuring the curvature of the charged particle in the magnetic field one can determine its momentum. Platforms all around the detector support the power supplies for each component. A small building on top of SLD, nicknamed "the penthouse", accommodates the fastbus readout electronics (FB) for the data acquisition. Great care went into radiation shielding and earthquake safety. The 5,000 ton detector is massive enough to absorb practically all particles emerging from the IP. A set of movable concrete blocks plug the ends of the tunnels and the space between the detector and the pit wall to absorb the synchrotron radiation from the beams.

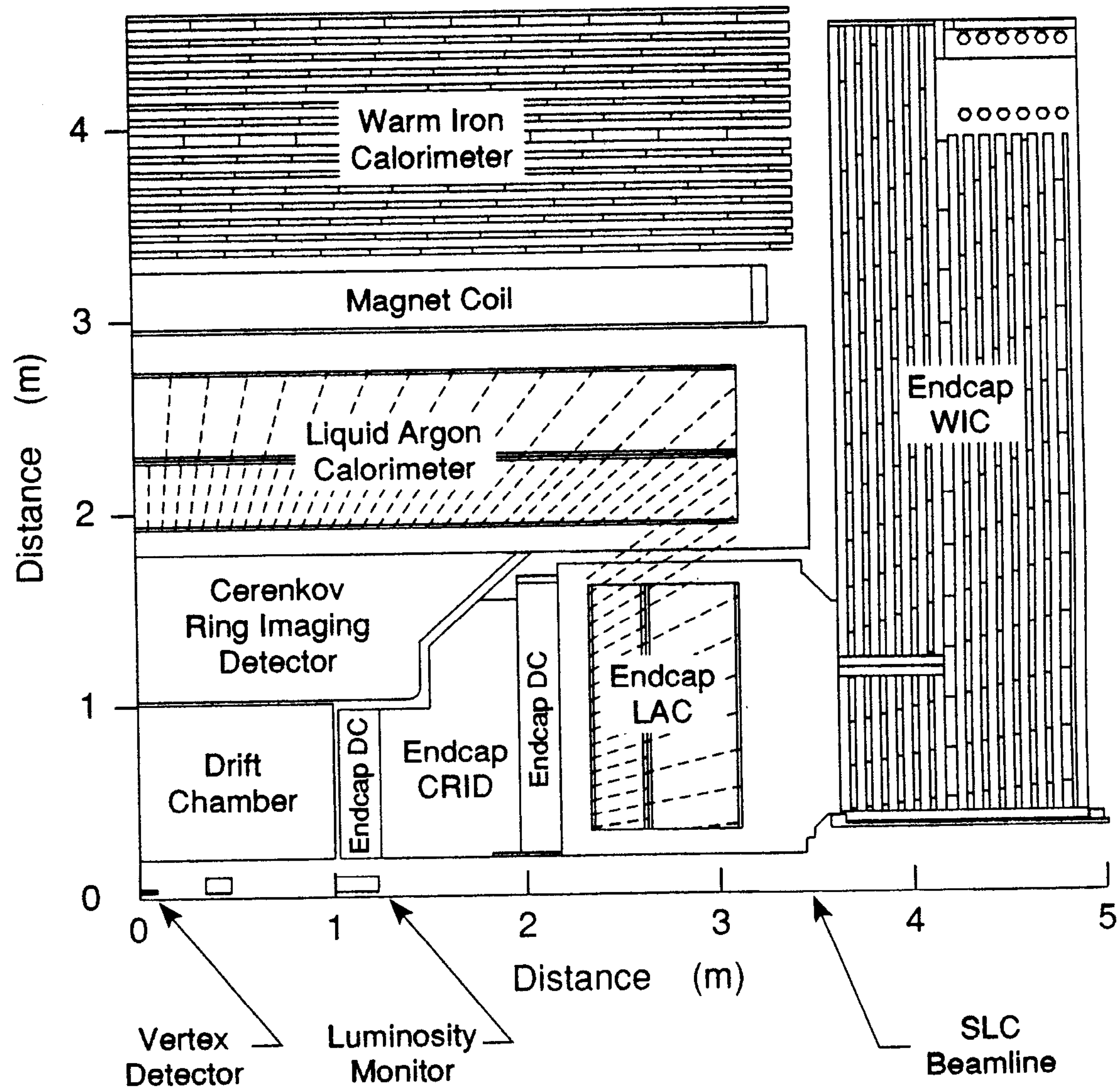

Figure 2.3 Quadrant View of the $S_L D$ Detector

2.4 Vertex Detector

The Vertex Detector is based on silicon charged coupled devices (CCD).[40] It comprises 480 CCD chips, each CCD contains approximately 400×600 pixels, adding up to a total of 120 Mpixels. Each pixel functions as an independent particle detection element, providing space point measurements of charged particle tracks with a typical precision of 5μm in each coordinate.

To ensure full coverage the CCDs are mounted on both sides of a ladder, slightly overlapping each other. These ladders are arranged in four concentric cylinders just outside the beampipe at radii between 29 and 41 mm (Fig. 2.4).

The vertex detector is build in a low mass structure (5% of a radiation lengths) to minimize multiple scattering. To reduce the noise in the semiconducting material of the CCDs the temperature is lowered to $200^\circ K$, by flowing chilled Nitrogen gas through the detector.

The total readout time for the entire vertex detector is 50 ms or about 6 beam crossings, hence the information is only read out if the trigger detects an interesting event.

The vertex detector is a powerful tool for distinguishing secondary vertex tracks, produced by decay in flight of heavy flavor hadrons or tau leptons, from tracks produced at the primary event vertex.

2.5 Drift Chambers

The drift chambers provide the position and momentum measurement for charged particles. A set of high voltage wires provide a uniform electric field in a gas filled volume. A charged particle traversing this volume ionizes the gas atoms and the electrons drift with a constant velocity towards the anode. In

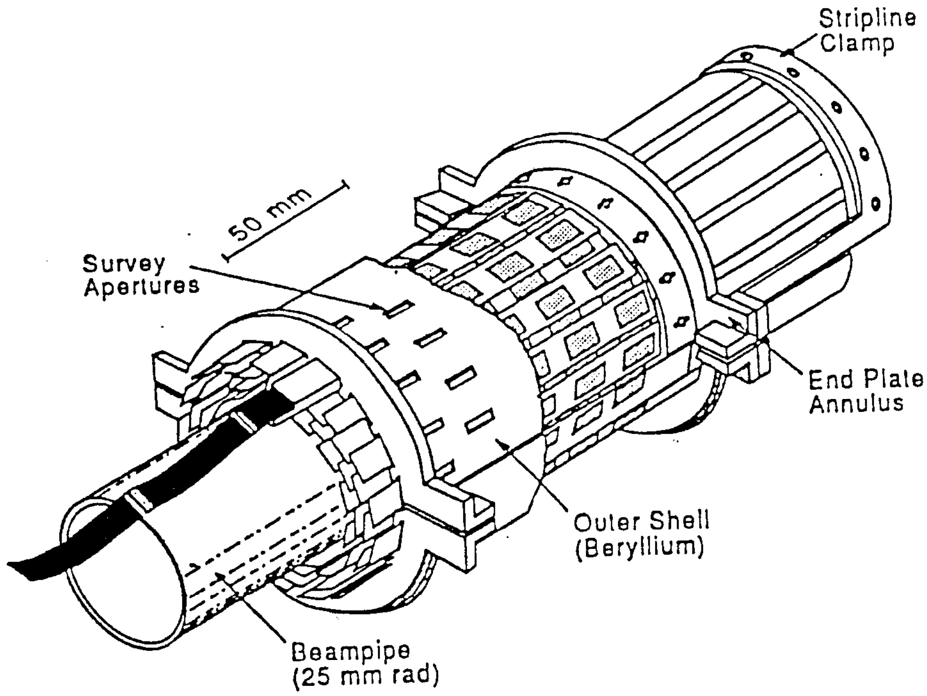

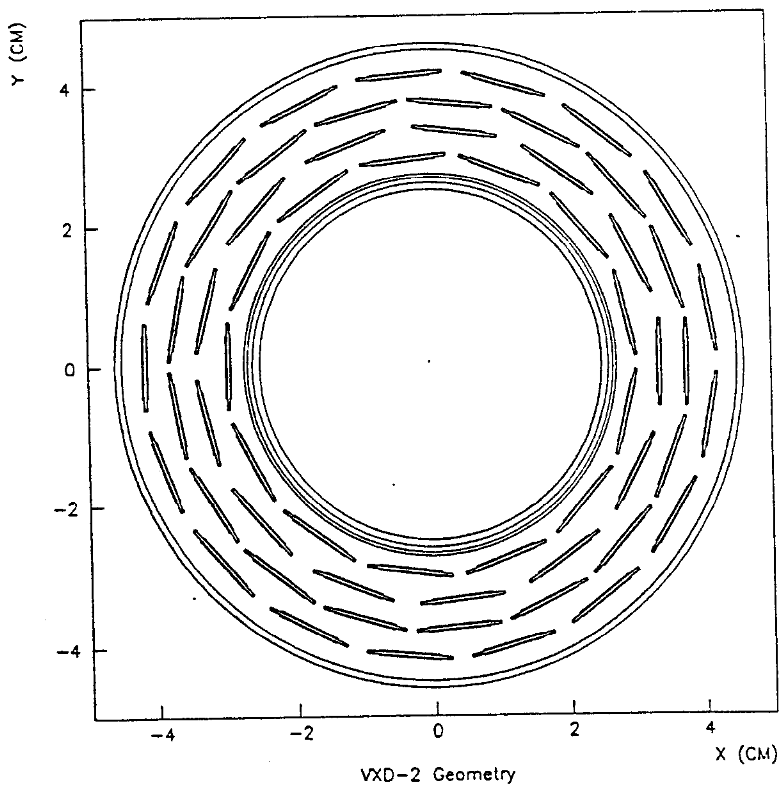

Figure 2.4 The Silicon Vertex Detector consists of 480 CCD chips located concentrically around the beam pipe at radii of only 2-4 cm, capable of measuring track positions with a resolution of 5 μm.

the high gradient field near the anode wires the electrons avalanche, amplifying the signal. Measuring the drift time and knowing the drift velocity, the drift distance can be determined to an accuracy of about $100\mu m$. A track fitting program then reconstructs the trajectory from the space points provided by the drift chamber. The curvature of the tracks in the magnetic field determines the particle momenta.

2.5.1 Central Drift Chamber

The central drift chamber is a barrel around the beampipe, 2 m in length, with an inner and outer radius of 0.2 m and 1 m respectively, centered about the interaction point. The constant drift field is provided by a set of cathode wires, field shaping wires and guard wires shown in Fig. 2.5.a. The maximum drift distance in any cell is 30 mm. The wires of the chamber are arranged in ten concentric superlayers, each having eight sense wires per cell, providing up to 80 space points per track (Fig. 2.5.b). Each sense wire is read out on both sides of the chamber. Charge division determines the coordinate of the hits along the wire to within 15 mm (Fig. 2.6). Since the driftcell is symmetric about the sense wires, it is not a priori known from which side the electrons drift in to the sense wire. To resolve this left-right ambiguity every third layer is an axial layer, i.e. the wire are strung parallel to the beam axis, the rest are small angle stereo layers, strung at a ± 50 mrad stereo angle with respect to the beam axis.

Most characteristics of the CDC, such as the gas and calibration, as well as the read out electronics, are the same as in the EDC and are described below.

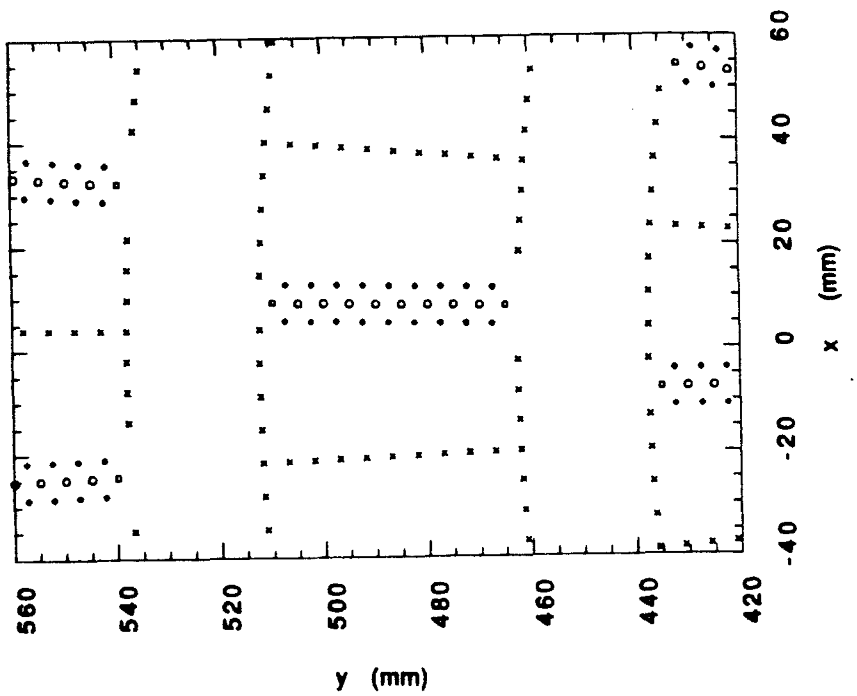

Figure 2.5.a A CDC drift cell: **o** are the sense wires, ◊ are the guard wires and **x** are the field shaping wires

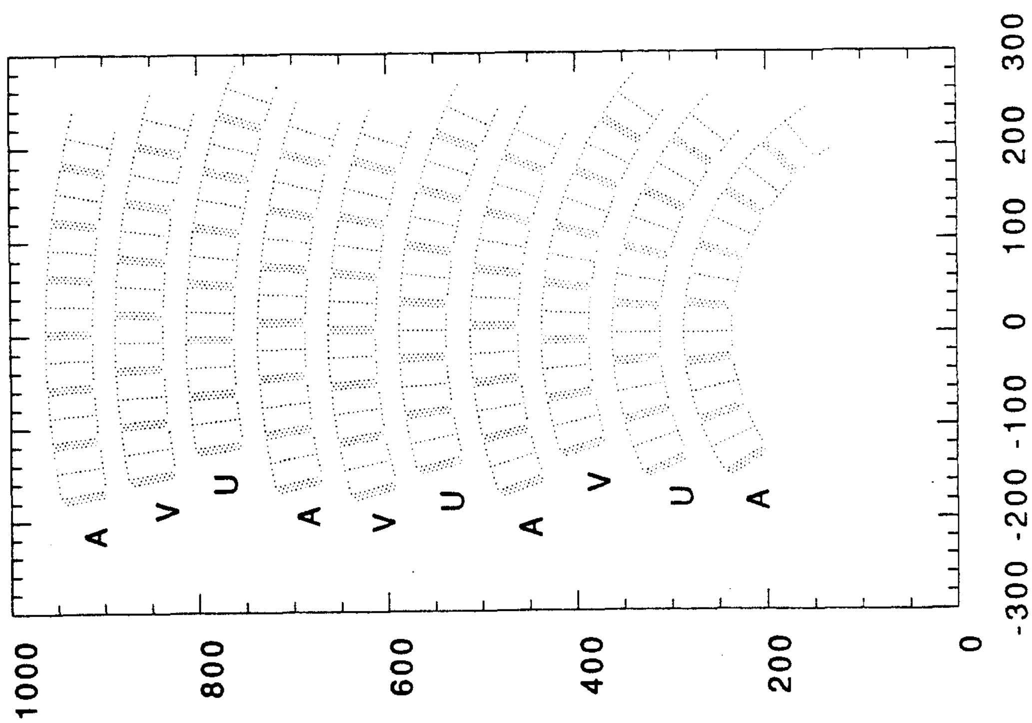

Figure 2.5.b 10 CDC superlayers: **A** denote the axial layers, **U** and **V** denote the stereo wires

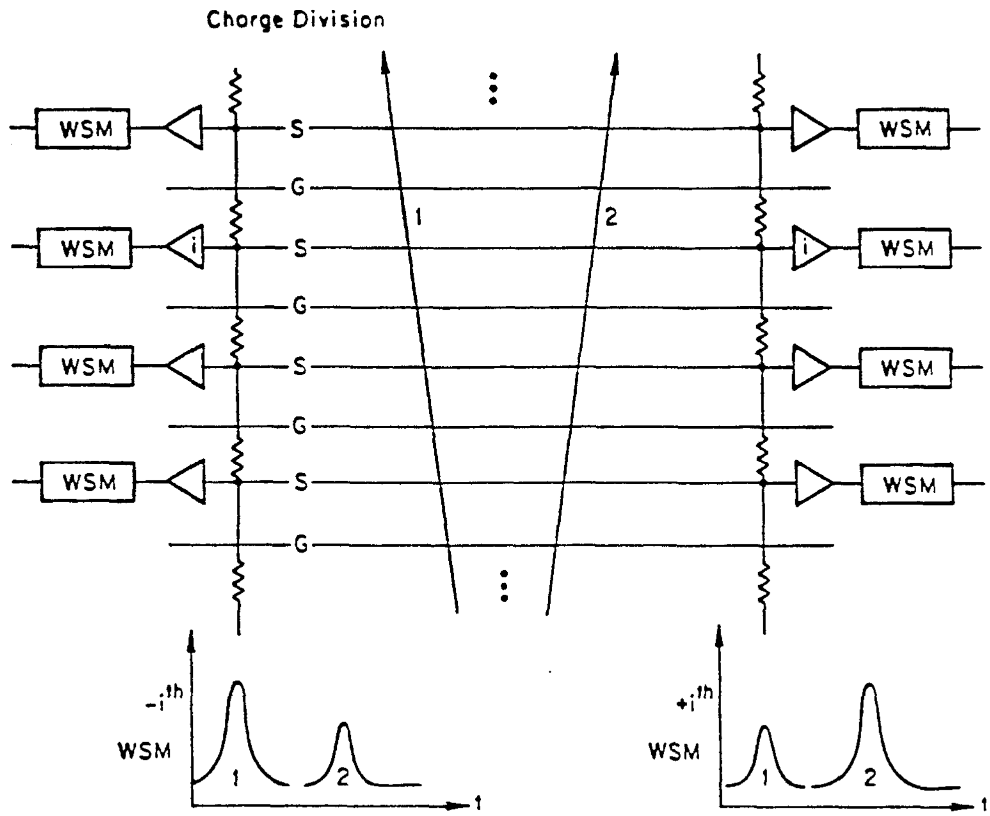

Figure 2.6 Charge Division is used to measure the z-coordinate of the hit.

2.5.2 Endcap Drift Chamber

About one half of the Z^0 events have thrust axes that lie within 40° of the beam axis, since the angular distribution of the events is proportional to $1 + \cos^2 \vartheta$. Therefore, good tracking information in the forward and backward direction improves the studies of hadronic event shapes significantly. At angles of less than 30° with respect to the beam axis the tracking resolution of the *CDC* drops off drastically, since the tracks only pass through a fraction of all layers. Four endcap drift chambers cover the region between 12° and 40°.

The *EDC*s were built by the Colorado group. I took part in building the chambers, testing them prior to the installation, installing them in the detector and maintaining them during the first two year of running. Therefore this part of the detector will be discussed in more details.

2.5.3 Description of the chambers and drift cells

Two sets of drift chambers at 1.12 m and 2.06 m from the interaction point with the wires strung perpendicular to the beam axis provide up to 36 additional space points for low angle tracks down to an angle of 12° with respect to the beam axis.

Except for their outer radius and number of cells the inner and outer *EDC*s are basically the same. Both sets of chambers have an inner radius of 0.2m to fit around the quadrupole magnets of the super conducting final focus. The outer radii are 0.97 m and 1.65 m for the inner and outer chamber respectively, so that both sets cover roughly the same solid angle from the interaction point.

Each drift chamber consists of three superlayers rotated by 120° with respect to each other (Fig. 2.7), providing three track segments which allow an unambiguous reconstruction of the trajectory in space.[41] Each superlayer of the inner and outer chambers consist of 22 and 34 cells each with 6 sense wires per cell respectively. 15 cathode wires make up the boundary between two adjacent cells and limit the maximum drift distance to 50 mm. The uniformity of the drift field across most of the cell is provided by 2.5 mm wide copper stripes, spaced evenly 2.5 mm, printed onto the G10 surface. A grid of guard wires in front of the sense wires improve the isochrony of the drift paths from different places across the width of the cell (Fig. 2.8). The voltage of every wire was chosen to optimize the linearity of the drift field. To ob-

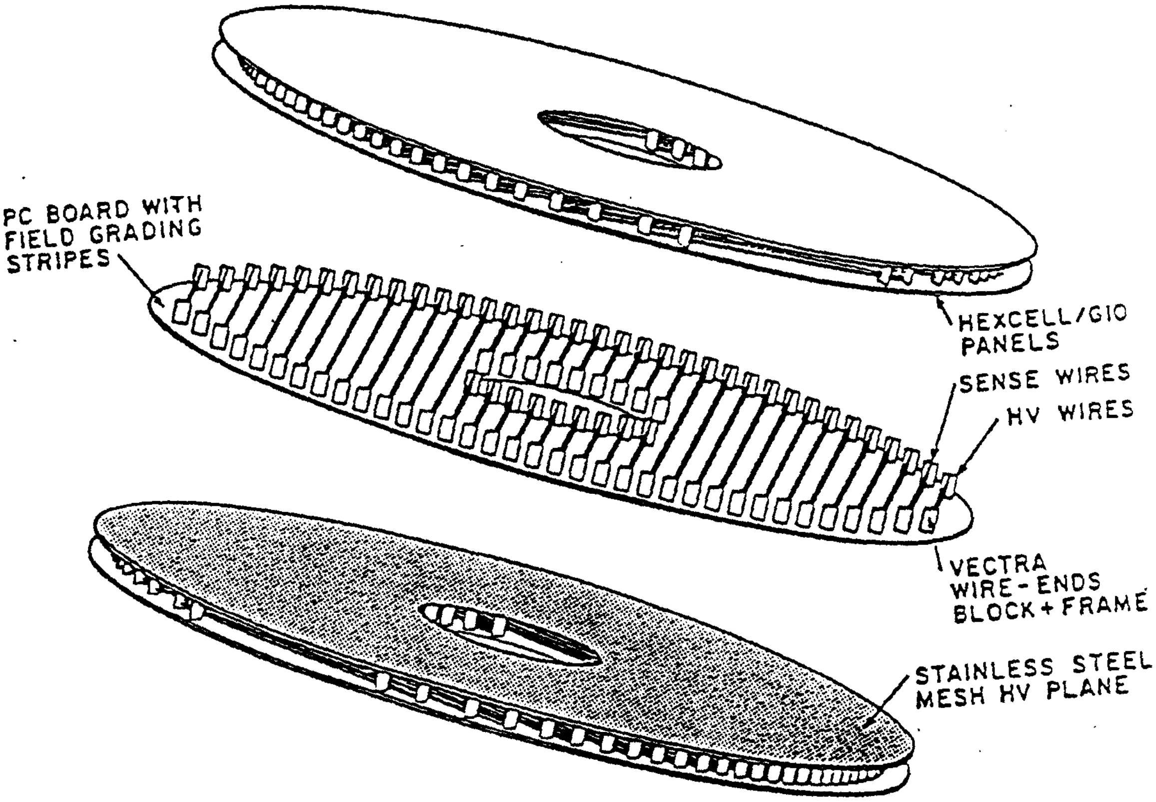

Figure 2.7 Blowup View of a Endcap Drift Chamber

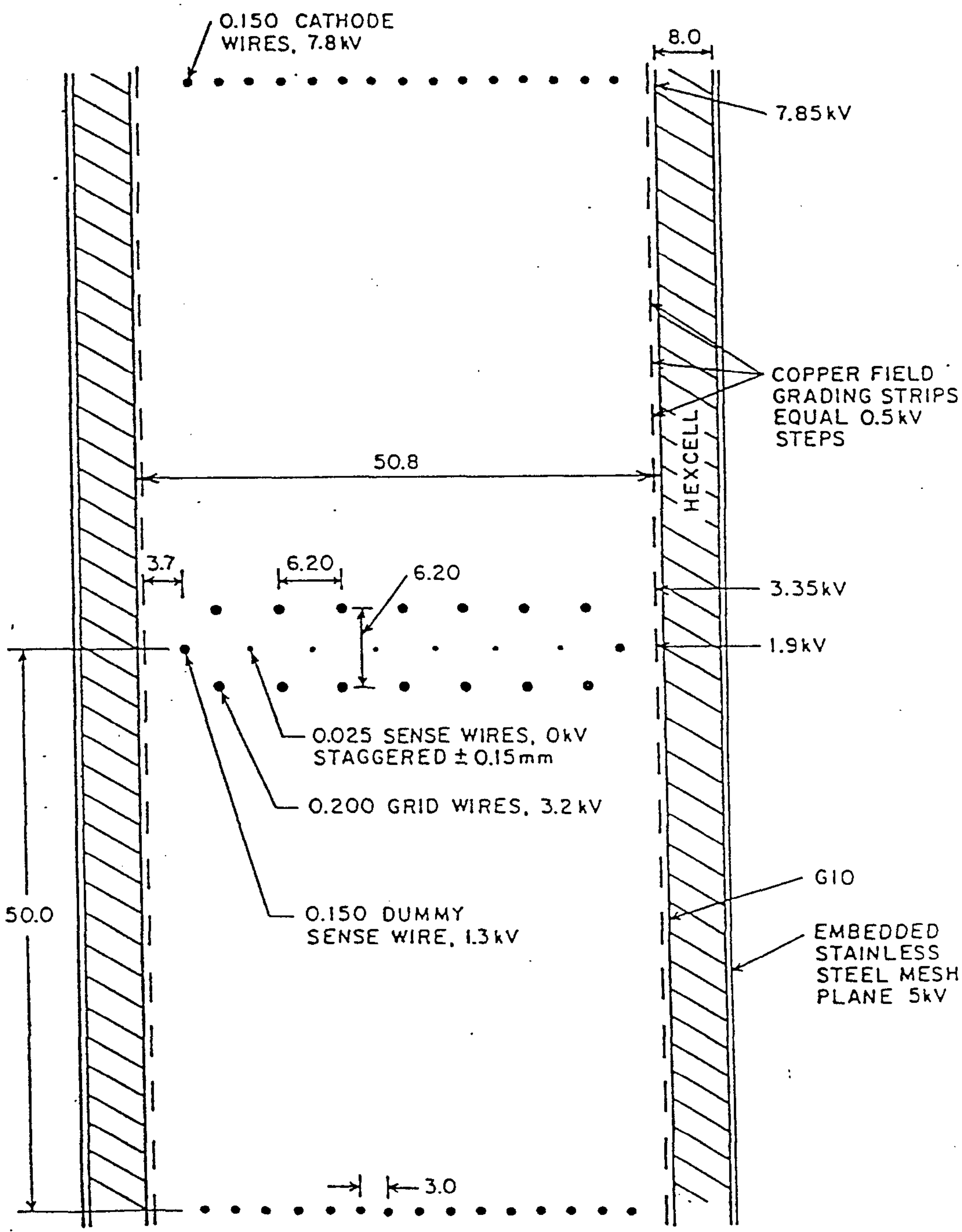

Figure 2.8 EDC Drift Cell

TABLE 2.1

Best Voltage Values from the Simulation

Name	Voltage (V)
High Voltage (Cathode Wires)	–7700
High Voltage Field Shaping (S10)	–7623
Low Voltage Field Shaping (S1)	–2808
Voltage Step Field Shaping	480.4
Guard Wires Voltage (G)	–2900
Copper Strip Low Voltage (S0)	–2265
Dummy Sense (DS)	–845
Steel Mesh	–2808

tain this we used a simulation program[42] that solves the electrostatic Poisson equation on a two dimensional grid, providing a detailed electric field map of the cell[43] (Fig. 2.9). The voltages used on the chamber are listed in Table 2.1. This results in an electric drift field of about 1 kV/cm which is constant to within $\approx 1\%$ in the sensitive area of the cell. A stainless steel mesh embedded in the panels separating each superlayer is kept at a uniform voltage of about 3000 Volts to isolate the electric field of adjacent superlayers from each other.

The sense wires are made of gold plated tungsten and are held at ground potential. Their diameter of only 25μm ensures a high gradient field near the surface of the wire enhancing the amplification of the signal.

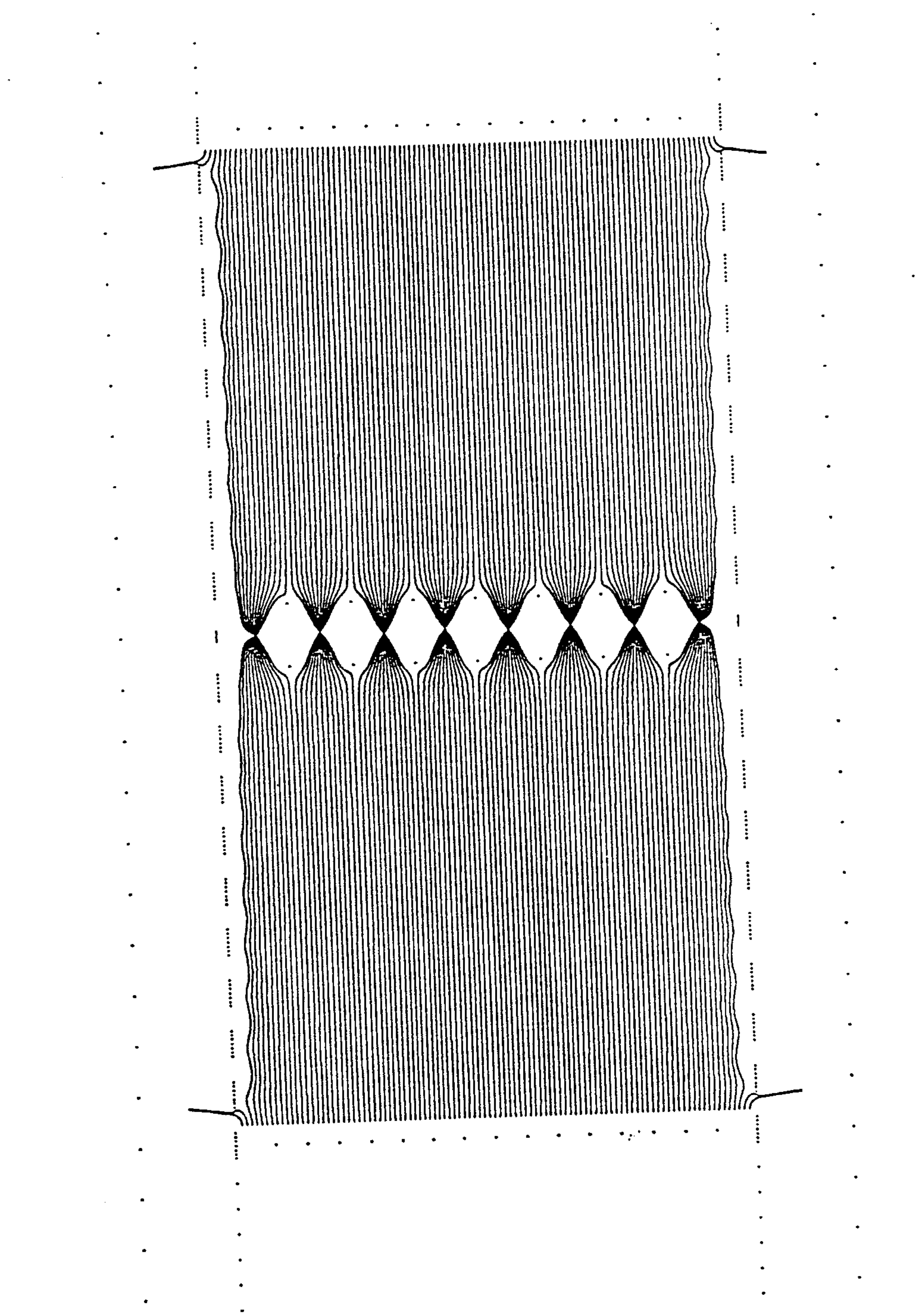

Figure 2.9 Electric Drift Field Map in EDC Cell. The drift field is constant to 1% in most of the cell and has a high gradient near the sense wires.

Like in the *CDC* it is not known on which side of the sense wire the electrons drift in. A stagger of $150\mu m$ of the sense wire away from the central plane of the cell results in different drift times for equal distances on either side. In a reconstruction program the right solution can be chosen by fitting the drift distances on either side of the sense wire plane to a helix trajectory and picking the solution with the lower χ^2 (see paragraph on track reconstruction).

The gas used in this drift chamber is a mixture of 75% CO_2, 21% Argon saturated with 0.3% H_2O and 4% Isobutane (C_4H_{10}). This gas mixture has a relatively small drift velocity of about 10μm/ns and low diffusion which is advantageous for a good drift time resolution. The Isobutane increases the gain so that the chamber can be run at a lower voltage which prevents electric break down. The small component of water in the mixture reduces the deposition of carbon atoms on the sense wires. Since oxygen is very electro-negative, even small amounts of it in the chamber seriously degrade the efficiency of the chamber by capturing the drift electrons. Great care was take to keep the O_2 content in the chamber below 50 ppm.

2.5.4 Time to Distance Calibration

A drift chamber measures the time between a beam crossing and the arrival of the signal on the sense wires. Assuming the particles from the *IP* travel at the speed of light, the time of flight can be subtracted to obtain the net drift time. Figure 2.10 shows a distribution of drift times typical for this drift chamber. The peak at low drift times is due to the higher drift velocity near the sense wires. To obtain the drift distance, which the experimentalist is interested in, he must know the exact time to distance relationship within the drift cells. To obtain this I used the program that calculates the electric field at every point of the cell and simulated the electron drift from many

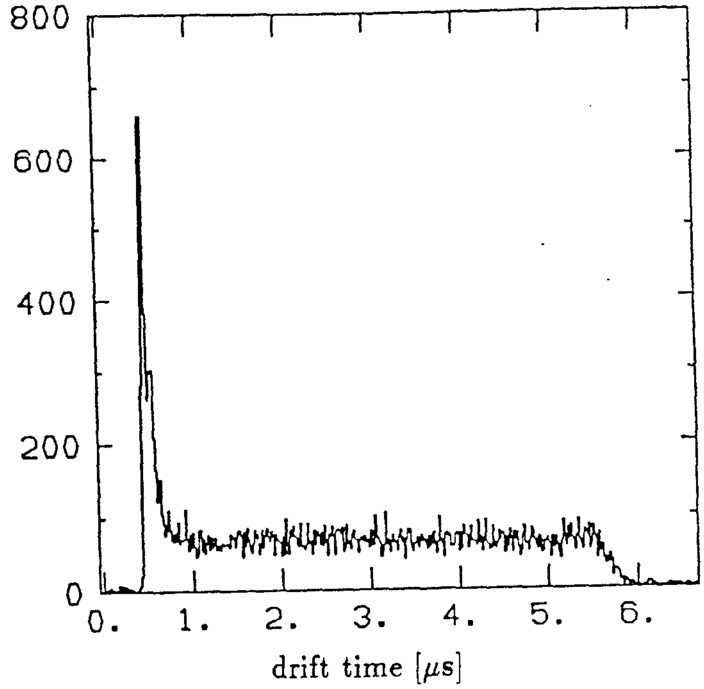

Figure 2.10 Drift Time Distribution in EDCs. The peak on the left is due to the increased drift velocity near the sense wires. .

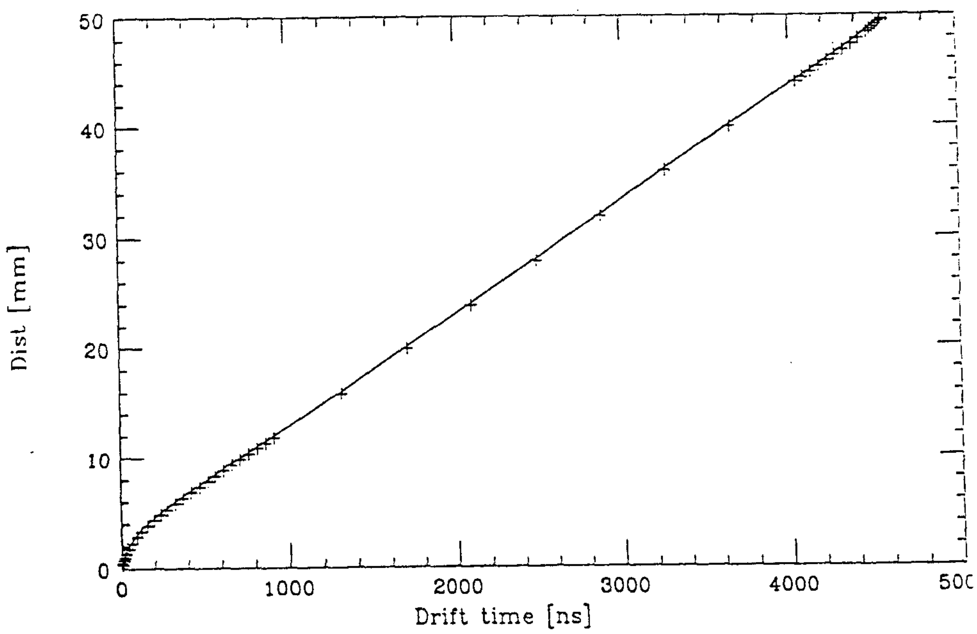

Figure 2.11 *t*-to-*d* Calibration curve: + mark points used in lookup table. Values between the points in the lookup table are obtained by interpolation.

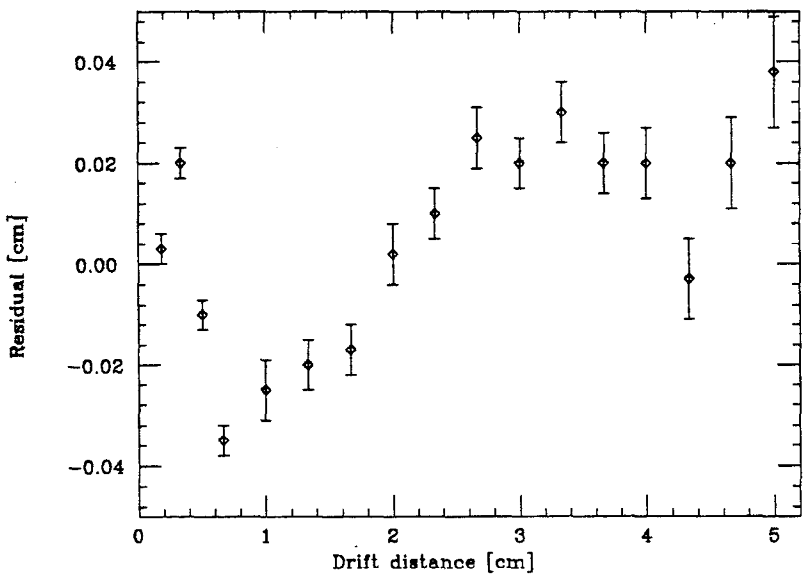

Figure 2.12a Average residuals distance of the raw hits to the fitted cosmic ray tracks as a function of drift distance, obtained with the t-to-d calibration from a lookup table.

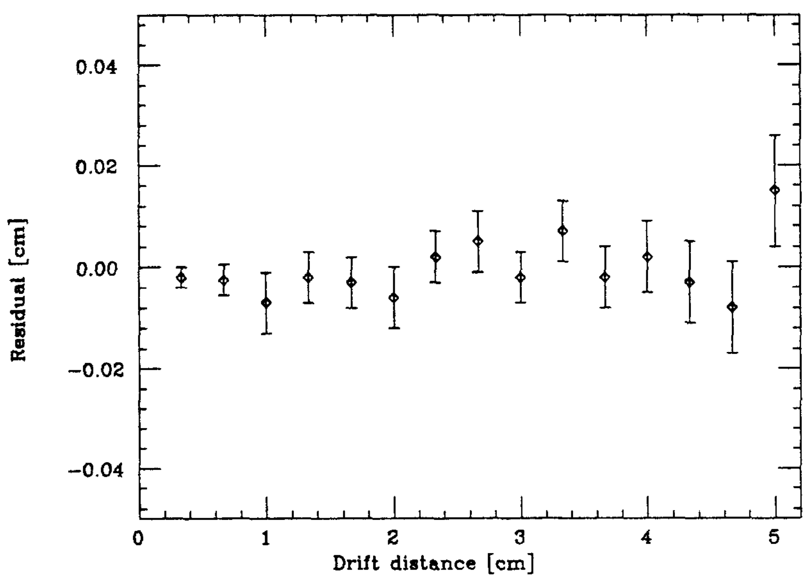

Figure 2.12b Residuals obtained with 2^{nd} order corrected t-to-d calibration for cosmic rays.

points in the cell to the sense wires, integrating up the drift time for each drift path.[44] For 50 discrete distances from the sense wires I chose the minimum drift time and put it into a lookup table (Fig. 2.11). More points are needed in the non-linear region near the sense wires than further out in the cell where the drift velocity is constant. An interpolation between the nearest points in this calibration table provides the drift distance for any given drift time. A simple parametrized angular correction is then applied for tracks crossing the cell at a non-zero angle from the perpendicular. An angle correction is necessary because ionization electrons near the boundary of the cell reach the sense wire before the ones on the center plane do, as is the case for tracks traversing the cell perpendicularly. In analyzing data taken in test runs with cosmic rays the limitations of this simulation, especially near the sense wires, emerge: Fig. 2.12a shows the average residual distance between the drift points and the fitted track as a function of drift distance. These residuals are then used as a correction to the drift distance acquired from the lookup table (Fig 2.12b).

2.5.5 Velocity monitor

To obtain a drift distance from a drift time, one needs to know the drift velocity at every point on the drift path. The drift speed in the gas used in the drift chamber is a function of the gas pressure and temperature, as well as on the gas mixture proportions and electric field. Temperature, gas mixture and electric field is controlled in the detector, but pressure varies with atmospheric conditions. To maintain optimal position resolutions, a drift speed monitor was developed, which gives continual measurements of the drift speed within all of the operating chambers.[45]

The drift speed monitor employs a pulsed UV laser to photo-emit electrons from the cathode and guard wires in particular cells within the chamber. These

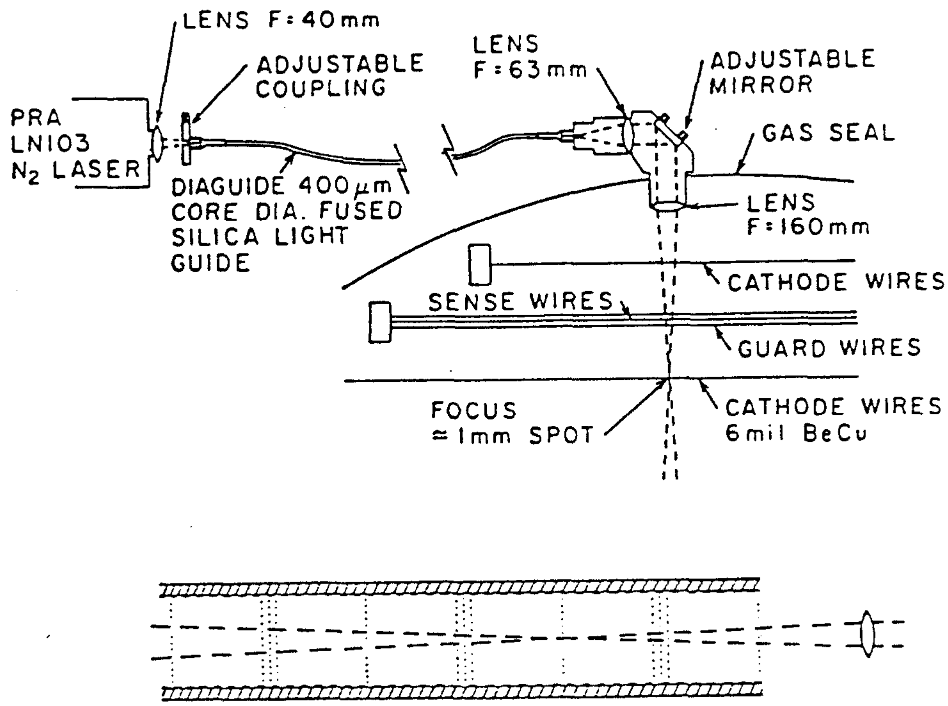

Figure 2.13 UV laser calibration system. Light pulses are focused onto guard wires and cathode wires at the edge of the chambers.

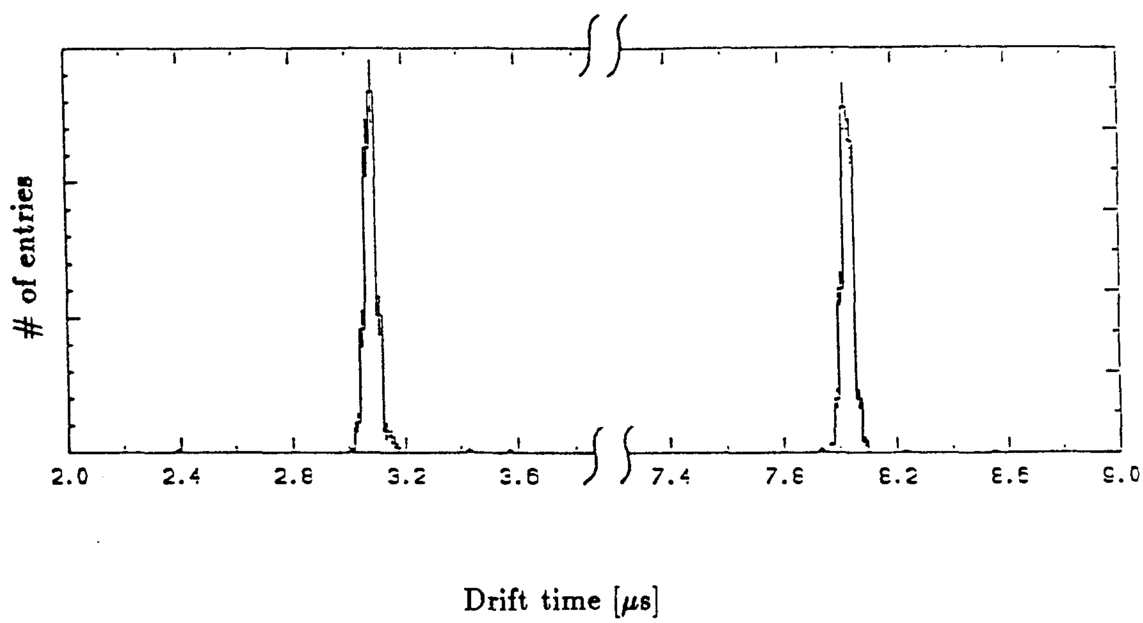

Figure 2.14 Time Distribution of Photo-emitted Electrons. The first peak is produced by electrons emitted from the guard wire, the second one from electrons emitted from the cathode wire.

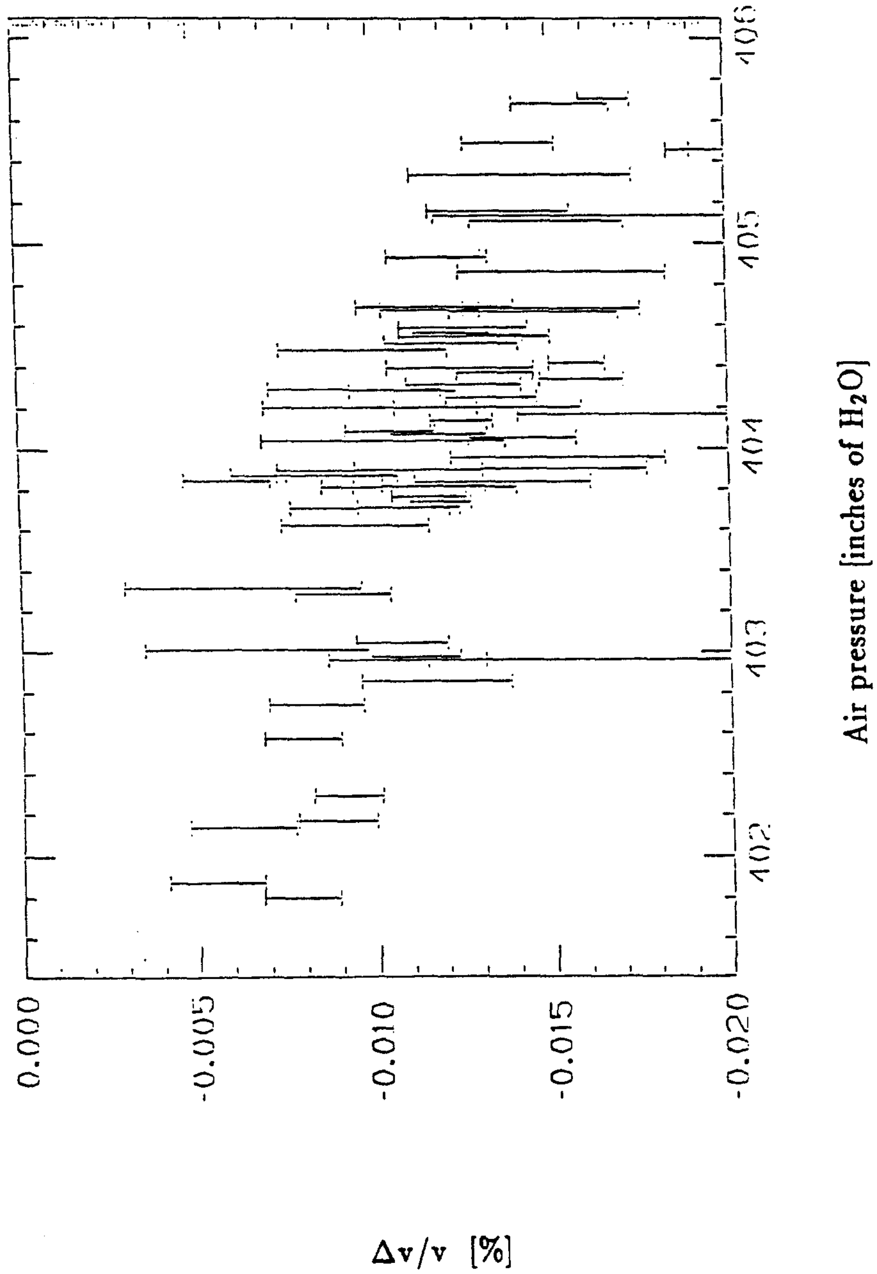

Figure 2.15 Drift Velocity vs. Pressure measured with the velocity monitor. The velocity is measured as deviation in % from the standard velocity.

photo-emitted electrons then drift along the electric field lines, to be collected at the sense wires in exactly the same way as ionization electrons from charged tracks. The timing between the pulse from the cathode wire and the guard wire calibrates the average drift speed along the drift path, knowing the fixed distance between the wires. Figure 2.13 shows the components of the monitor. The 337 nm light from a nitrogen laser is focused on the end of a bundle of 21 light guides and then transmitted down to the outer gas seal of the drift chamber, where a telescope system of two quartz lenses and a mirror is mounted to focus and steer the light onto a particular set of wires in the outermost cell of the chamber. After carefully centering the 7mm$\times$ 9mm spot on the bundle of 21 fibers, using the 5 corner fibers, which are extracted from the bundle, an average of 1.5μJ is transmitted to the end of the fibers. The position of the fibre relative to the laser can be optimized with an adjustable mount. The optics produces a spot of about 1mm diameter at a focal plane. Figure 2.14 shows a typical distribution of the difference in drift time from the electrons emitted from the cathode and guard wires. The Laser is triggered once every minute. The drift times from 100 successive measurements are averaged to obtain the drift velocity as a function of time. Figure 2.15 shows the variation of the drift velocity as a function of pressure, taken over the period of several days. The variations of the individual measurements are also due to slight changes in gas mixture and temperature.

2.5.6 Electronics

The readout electronics for the *CDC* and the endcaps are functionally similar, differing only in the geometrical layout. Performance and space requirements led to a novel design for the *SLD* drift chamber electronics system. Most of the components are installed on the chamber itself. within the magnet volume in order to minimize noise pick-up, capacitive loading of the signals and cable plant volume. The signal from the sense wires are passed on to an 8-channel preamplifier (one per cell, for the *EDC* two channels remain unused because it is a 6 sense wire cell) which is located on a circuit board shaped to fit directly on the outside surface of the chamber (Figure 2.16). Each of these motherboards processes 4 to 6 cells. The amplifiers have a 8 ns risetime to ensure a time resolution equivalent to the spacial resolution of the drift chamber of $\leq 50\mu$m. The analog signals are then routed to a Hybrid Analog Memory Unit (*HAMU*) on the same circuit boards. The HAMU is a storage system which divides the incoming waveform into 512 time buckets of 16.8nsec (59.5 MHz sampling frequency) each on a custom HAMU monolithic chip. The HAMU stores the 512 samples in an array of capacitors. The HAMU memory is continually overwritten for every beam crossing (120Hz at the SLC) until a triggered event occurs. Upon an external read request, the stored analog information is multiplexed onto two sets of output buses which are connected to A/D converters which digitize the signal. The digital signals are then serialized in shift registers and passed on to the controller board (one per side of the *CDC* and one on each endcap).

To simplify the cable plant of the readout the signals of several motherboards are again multiplexed and converted to light pulses on a transition board which sends the information through optical fibers to the fastbus data acquisition system in the "penthouse" on top of the detector. The digital waveforms of 4 motherboards (192 channels) can be transmitted through a single fiber. Using optical fibers instead of coaxial cables also has the advantage to break the ground lines from the outside to the electronics and stop noise pulses generated by ground loops. The signals are then processed in the

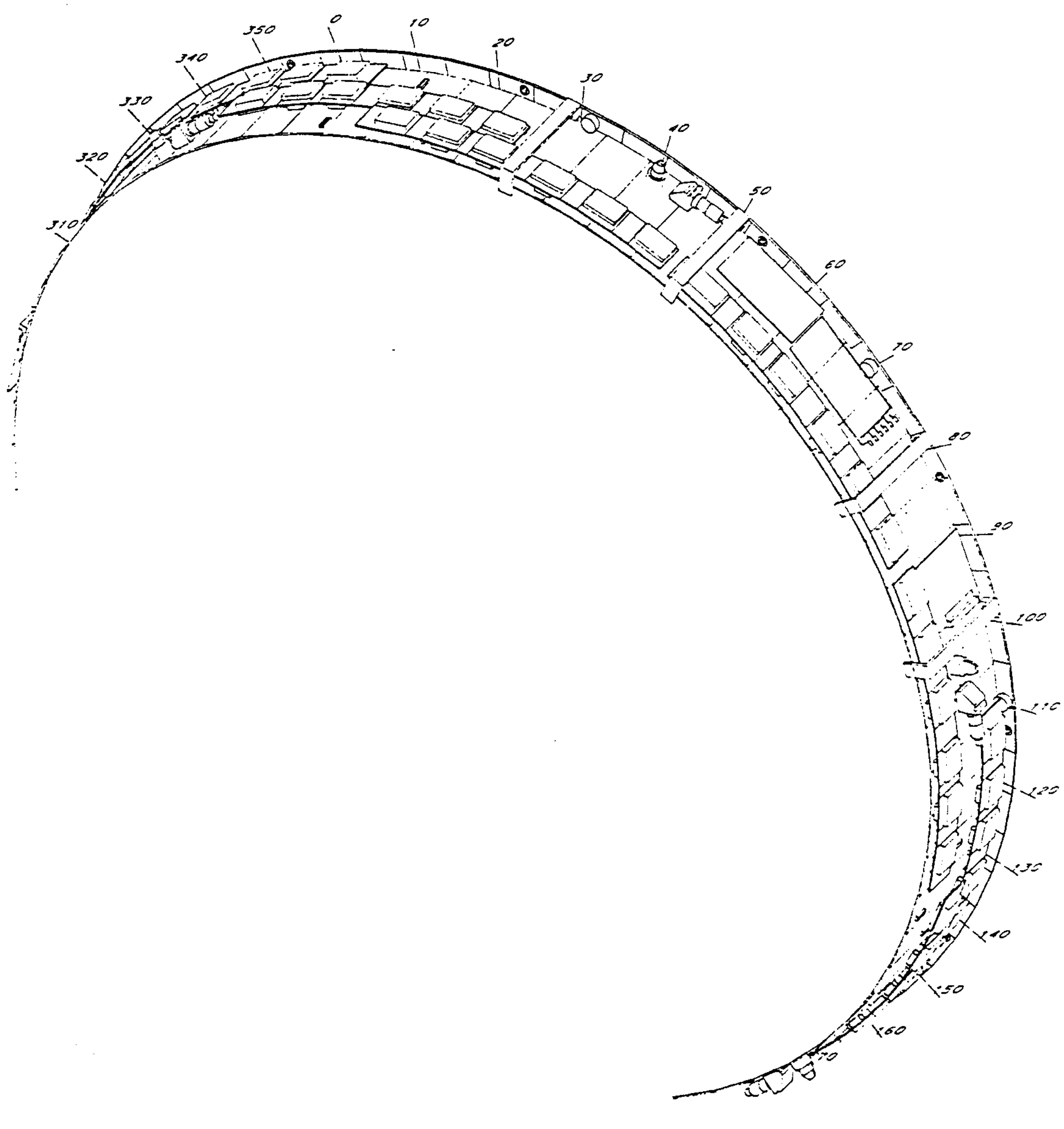

Figure 2.16 Readout electronics boards containing preamplification and digitization are mounted directly on the chamber.

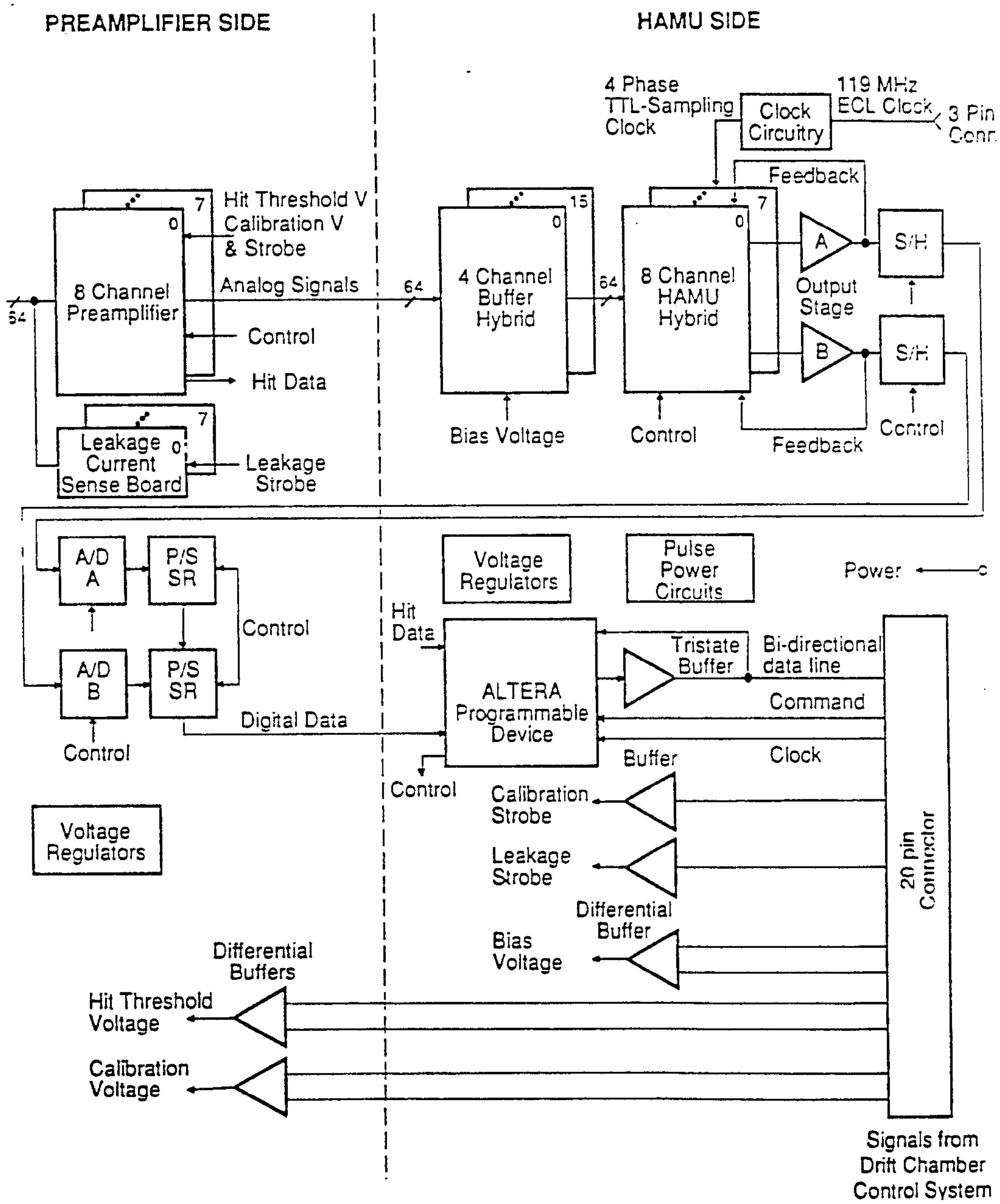

Figure 2.17 Schematic of the Drift Chamber Readout Electronics

Waveform Sampling Module (WSM) which correct each channel for pedestal offsets and gain. The parameters for the correction are acquired in calibration runs taken once a day. The corrected data is passed via the fastbus system to an ALEPH Event Builder (AEB) for first level online data processing: the wave form of 512 digitized words is truncated and only the part that contains a pulse, called a snip, is passed on to that wave form algorithm which finds the starting time of the pulse in the snip. Only these drift times, along with a random selections of whole pulse snips for control purposes, are passed up the the VAX 8800. In this whole process the initial data volume of approx 10 Mbytes is reduced to 10 kbytes which subsequently get written to magnetic cartridge.

The central drift chamber data is also utilized in the readout trigger decision of the SLD. The pulses from the sense wires are discriminated and if the pulse hight exceeds the preset threshold, a flag is set. These bits are multiplexed in the hit-circuitry on the motherboard and sent in parallel to the transition/controller boards, where the data is temporarily stored and then optically transmitted to a fastbus Drift Chamber Trigger module ($DCTR$). If more than four sense wires in a cell are hit, the cell is considered *on*. The DCTR then compares all combination of *on* cells against a stored list of all cell combinations formed by a real track. If it finds a match, the cell combination is counted as a track. This is a very quick procedure that is done every beam crossing. The number of found tracks can then be used in a trigger decision.

2.5.7 Track Reconstruction and Resolution

In a first stage the reconstruction program fits the raw hits from each of the 6 (8 in the CDC) sense wire in a cell to a track segment called vector hit, by minimizing the χ^2 of residual distance of the raw hit to the vector hit (Fig. 2.18). In the EDC these vector hits could be anywhere along the wire, because the sense wires are only read out on one end. The EDCs provide no information in this dimension, unlike the CDC which uses charge division. In a second stage the program loops over all possible combination of vector hits in the 3 superlayers of each chamber trying to fit an entire track segment through the chamber, shown schematically in Fig. 2.19. Fig. 2.20 shows the raw data and the fitted tracks in an event in the CDC. The hits read out from the chamber are drawn as mirror images on each side of the sense wire since it is not a priori known from which side the electrons drifted in. In the last stage of the reconstruction the program tries to connect the track segments from both inner and outer drift chamber as well as from the CDC and the Vertex detector to form a complete track. This track is then fitted to a helix, the trajectory a charged particle describes in a magnetic field. The direction and radius of this helix yields the charge and momentum of the particle associated with the track.

How well we can determine the momentum of a particle depends on the spacial resolution of each detector component. We distinguish between local and global resolution. The local resolution is the width of the distribution of the residuals to the vector hits in each cell, while the global resolution is the width of the distribution of the residuals to the fitted track. The spacial resolution has a strong dependence on the distance to the sense wire (Fig. 2.18). Close to the wire, in the high gradient field the uncertainty of the

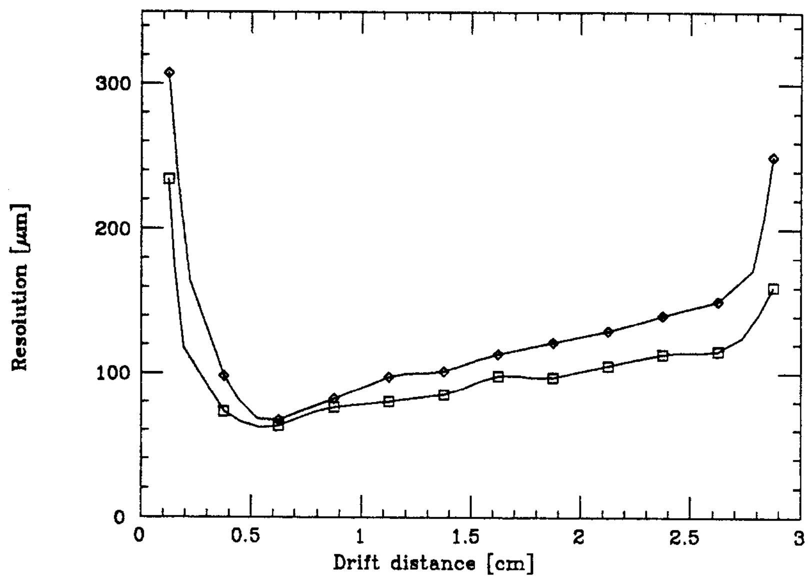

Figure 2.18a Local (bottom curve) and global (top curve) drift Distance Resolution in CDC measured as a function of the drift distance.

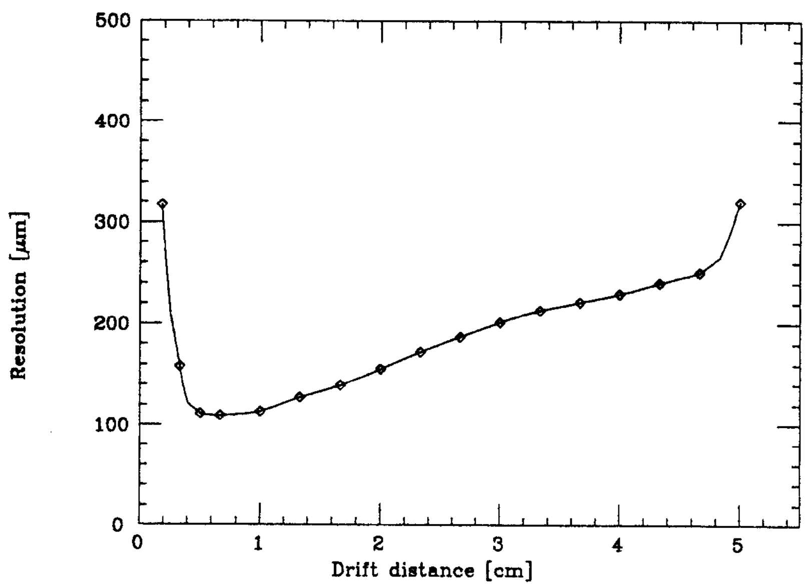

Figure 2.18b Global drift Distance Resolution in EDC measured as a function of the drift distance.

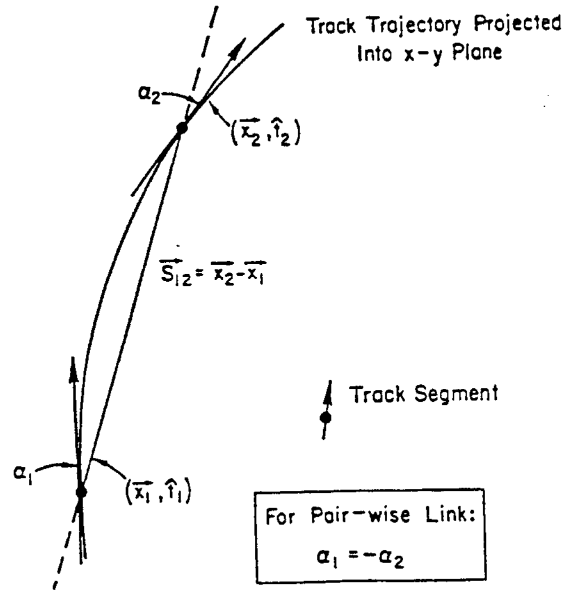

Figure 2.19 Schematic of the Track reconstruction.

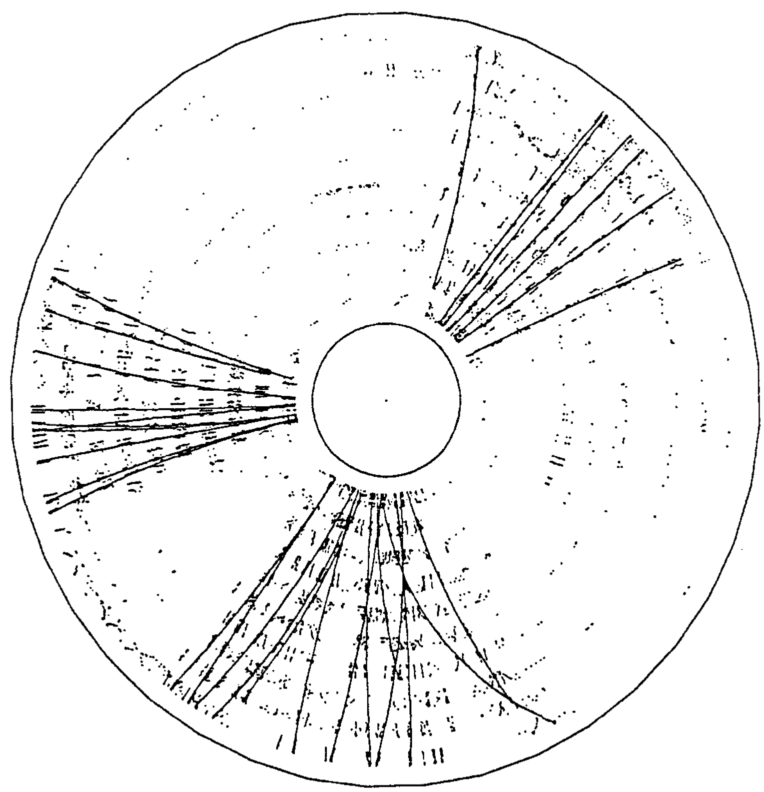

Figure 2.20 Raw hits and fitted tracks. The hits read out from the chamber are drawn as mirror images on each side of the sense wire.

measurement increases with the velocity of the drifting electrons. At the other end of the cell the resolution is degraded by diffusion and loss of electrons due to capture and recombination. At best the local resolution in the *EDC* is better than 100μm and averages at about 140μm over the entire cell. For the *CDC* the local resolution is better than 70μm and averages at about 100μm over the whole drift region. The global resolution is always worse than the local one, since additional uncertainties, like multiple scattering, dE/dx losses and errors in the mutual positioning of the detector components, have to be taken into account. The design momentum resolution of the drift chambers averaged over the angle $|\cos\vartheta| < 0.96$ may be parametrized as

$$\Delta p/p = \sqrt{(0.01)^2 + (0.0025p(\mathrm{GeV/c}))^2} \tag{2.4}$$

and with the constraint from the CCD's of the vertex detector

$$\Delta p/p = \sqrt{(0.01)^2 + (0.0015p(\mathrm{GeV/c}))^2}. \tag{2.5}$$

At small angles where most of the tracking information comes from the *EDC* alone, the resolution is somewhat worse, given by

$$\Delta p/p = \sqrt{(0.015)^2 + (0.003p(\mathrm{GeV/c}))^2}. \tag{2.6}$$

The momentum resolution in the *CDC* can be measured by comparing the two track segments of a cosmic ray that passed through the center of the *CDC*. These measurements indicate that the momentum resolution at the present stage of the reconstruction programs is about a factor two worse than the design resolution. This is mostly due to the lack of knowledge of the exact wire positions and directions. Alignment studies are expected to improve the momentum resolution significantly. The momentum resolution of tracks that pass through the vertex detector was shown to be almost down to the level of the design and will also improve with the exact position calibration of the vertex detector.

2.6 CRID

The Cherenkov Ring Imaging Detector (CRID) is used for particle identification and flavor tagging. When a charged particle passes through a medium, exceeding the speed of light in that medium, the atoms get polarized and emit photons (Cherenkov radiation). The opening angle of the light cone with respect to the incident track is inverse proportional to the velocity: $\cos\vartheta_c = \frac{1}{\beta n(\lambda)}$. The emitted light is focused onto a photon detector and by measuring the radius of the light circle one can determine the velocity of the particle. Together with a momentum measurement of the particle the mass and hence the type of the particle can be determined.

The *CRID* used in *SLD* consists of four main parts: first the particle passes through a thin layer (10 mm) of liquid radiator. The liquid used is Freon (F_6C_{14}) with an index of refraction $n = 1.277$. For $\beta = 1$ the Cherenkov angle of the photons is 672 mrad. The photons are mainly emitted at frequencies in the near UV region (170-220 nm), therefore the endplates of the radiator vessel are made out of quartz glass, which is transparent to UV light. Typically about 14 photons are emitted by a particle of $\beta = 1$. After being refracted by the quartz window by 236 mrad the photons pass across the 13 cm gap to the photon detector at an angle of 52° with respect to the incident particle trajectory, forming a circle of 17 cm radius and about 1.5 cm width (Fig. 2.21).

On the other side of the photon detector is the gas radiator filled with

C_5F_{12}, a gas transparent to UV light and a low index of refraction (n=1.0017). To get an equal amount of light from the gas radiator as from the liquid its thickness is about 45 cm. The angle under which the light is emitted is 59 mrad. The photons are reflected and focused back onto the outer side of the photon detector by a set of spherical mirrors mounted on the outer wall of the $CRID$ vessel.

A time projection chamber is used to detect the Cherenkov light (Fig. 2.22). The drift volume is filled with ethane saturated with $TMAE$ (Tetrakis Dimethyl Amino Ethylene), which has a very high quantum efficiency in the wave length range of 170 to 220 nm. The photons enter the driftbox from the top and the bottom through a quartz window and are absorbed by the organic $TMAE$ molecules and knock out an electron which then drifts to the sense wires. The uniform drift field of 400 V/cm is established by a set of equally spaced wires around the box. Over a maximum drift distance of 126 cm this amounts to a potential difference of 60kV from one end of the box to the other. The electrons drift parallel to the magnetic field in the detector. The anode of each drift box is made of 93 carbon fiber wires, 7μm thick, strung in the radial direction. The z-coordinate of the photon conversion, along the barrel axis, is measured by the drift time, the azimuthal coordinate is determined by the anode wire address. The depth of the conversion in the drift box is measured by charge division on the sense wires to better than 1%. The detector is optimized for single electron detection, typically only four or five electrons from each circle make it all the way to the anode. However, it will also detect the large dE/dx ionization loss from the charged particle passing through the drift box, depositing about 700 electrons.

The accuracy with which the $CRID$ measures the Cherenkov angle, ϑ_C is

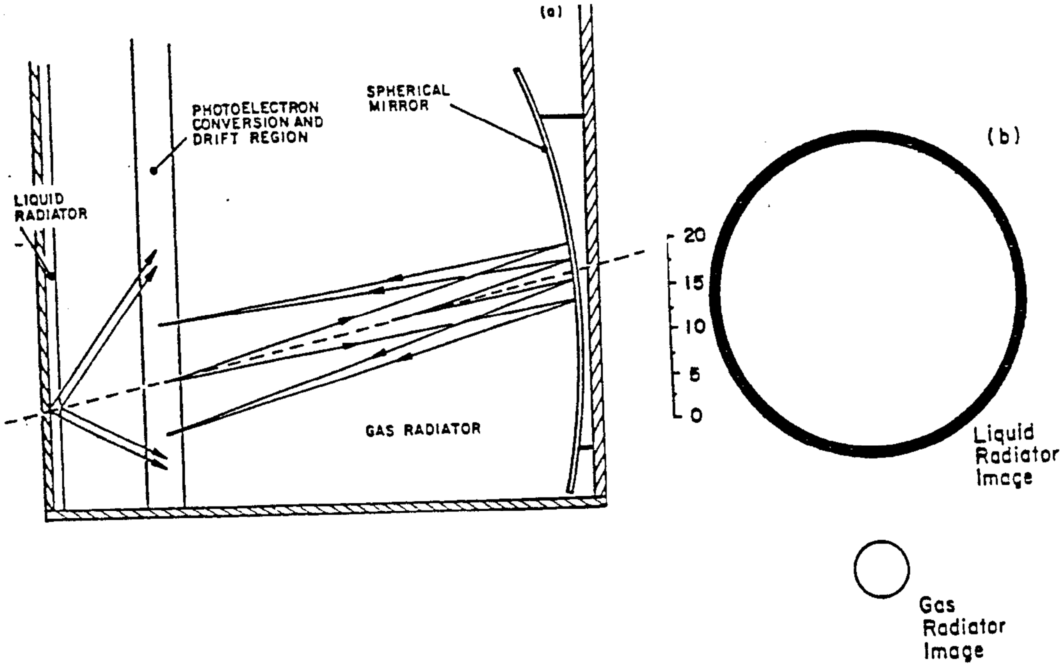

Figure 2.21 The CRID consits of a liquid and gas radiator and time projection chamber for photo detection. The size of the rings from the two radiators are indicated by the circles.

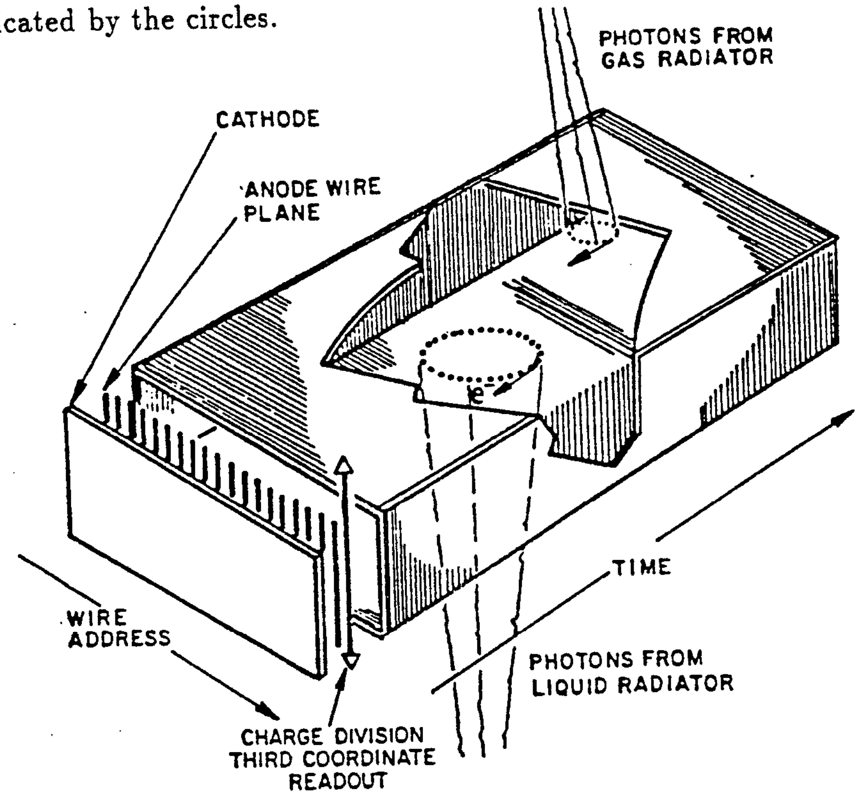

Figure 2.22 CRID Time Projection Chamber used for Cherenkov Photon Identification.

Table 2.2 CRID Properties (Design)

	Liquid	Gas
1. Solid Angle Coverage	88%	93%
2. Angular Coverage (Endcap)	n/a	$8.5^\circ - 42.1^\circ$
(Barrel)	$40.2^\circ - 89.1^\circ$	$46^\circ - 89.5^\circ$
3. Radiator Material	C_6F_{14}	C_5F_{12}
4. Index of Refraction (at 6.5 eV)	1.277	1.001725
5. Thickness of Radiator	1 cm	$\sim$ 45 cm
6. Focusing Method	proximity	spherical mirror
7. Cherenkov Threshold γ for pions	1.61	17.05
8. Cherenkov Angle (for $\beta = 1$)	672 mrad	59 mrad
9. Radius of Cherenkov Ring (for $\beta = 1$)	17 cm	2.9 cm
10. Number of Photoelectrons (for $\beta = 1$)	14	14
11. Momentum Threshold (for 3 p.e.)		
e	$\sim$ 1 MeV/c	$\sim$ 9.5 MeV/c
π	0.23 GeV/c	2.6 GeV/c
K	0.80 GeV/c	9.1 GeV/c
p	1.50 GeV/c	17.3 GeV/c
12. Particle Separation Range at 90° (3σ Level)	[both radiators]	
e/π	0.2 to 6.2 GeV/c	
μ/π	0.2 to 1.1 and 2.1 to 3.8 GeV/c	
π/K	0.23 to 23 GeV/c	
K/p	0.80 to 37 GeV/c	

limited by

a) the chromatic error due to the variation of n for different frequencies of the emitted photons,

b) the spacial resolution of the photon detector,

c) the width of the circle projected onto the drift box due to the finite thickness of the liquid radiator and the focusing from the gas radiator

d) the uncertainty of the trajectory of the charged particle due to multiple scattering in the inner wall of the $CRID$ and the curvature in the magnetic field. Thus the Cherenkov angle for a track can be measured to about 1 mrad. The momentum thresholds and separation range for various particle types are listed in Table 2.2.

2.7 Calorimetry

The task of the calorimeter is to measure accurately the fraction of electromagnetic and hadronic energy from the decay of the Z^0, covering as much of the solid angle around the interaction point as possible, as this is very important in cleanly separating events with missing energy. The SLD calorimeter consists of three parts, a lead-liquid argon calorimeter (LAC), which absorbs most of the electromagnetic and hadronic energy, and an outer part consisting of a warm iron calorimeter (WIC) which contains the tails of the hadron showers and a Luminosity Monitor (LUM) which measures the energy deposited at very small angles to the beampipe. The electromagnetic part of the LAC has 22 radiation lengths and the LAC and the WIC together have 8 interaction lengths to absorb most hadrons completely. In one radiation length, X_0, $1 - e^{-1}$ of all charged particles interact electromagnetically and in one interaction length $1 - e^{-1}$ of all hadrons interact strongly with the matter they are passing through. Electrons and gammas form electro-magnetic showers which can be distinguished from hadronic showers by the energy deposition per penetration length. Electro-magnetic showers deposit most of their energy within the first section of the LAC while hadronic showers extend much further into the detector since the hadronic interaction length is greater than the electro-magnetic radiation length. The form of the showers can thus be used to separate electrons from pions and/or protons. A matching track in the *CDC* will identify an EM shower as an electron which can thus be separated from a shower induced by a gamma.

2.7.1 Liquid Argon Calorimeter

The *LAC* is placed inside the magnet coil, to avoid degrading the performance of the calorimeter due to energy absorbtion in the material of the coil. The *LAC* works as a ion chamber, collecting the charge deposited in the argon by electromagnetic or hadronic showers. The chamber is made of stacks of lead tiles interspersed by gaps filled with pure liquid argon. The tiles are alternately at ground potential and at negative high voltage. The electrons from the primary ionization by the jets drift to the anode where the total charge is measured. No secondary ionization, like in the drift chamber, amplifies the signal. Since Argon is a very inert liquid only a very small portion of the charge is lost to recombination. Stacks of tiles are daisy chained together to form projective towers pointing back to the *IP* (Fig. 2.23). The towers have lateral dimensions between 6 and 12 cm, somewhat larger than the average size of an electromagnetic shower. The towers are further split into four parts in the radial direction, making up two electromagnetic parts of the calorimeter, $E1$ and $E2$, and two hadronic parts, $H1$ and $H2$ (Fig. 2.24). The geometry of the electromagnetic section was chosen to provide the best possible efficiency for isolating electrons from semileptonic decays within jets, lowest possible π/γ overlap background, and good position resolution. The LAC is placed inside a vacuum vessel and surrounded by a cryostat which is cooled by liquid Nitrogen. The LAC endcaps are a continuation of the barrel in the forward and backward direction with a similar internal tower geometry. The endcaps fit like plugs inside the barrel. Together they cover about 98% of the solid angle for electromagnetic showers.

Since a liquid argon calorimeter has no gain in the sensitive medium and therefore produces very small signals, low noise amplifiers must be provided. The approximately 44,000 electronics channels require a fast pre-processing of the event to form a reliable trigger information and to reduce the data volume passed on to the computer.

2.7.2 WIC and Muon Identification

The hadronic energy which escapes the LAC is measured by the Warm Iron Calorimeter which also serves as a muon tracking device and as the flux return for the magnetic field. The WIC is the outer structure of SLD. The iron structure is segmented into 14 layers, 50 mm thick with 32 mm gaps instrumented with streamer tubes (Iarocci tubes) shown in Fig. 2.25. At 90° the iron makes up 4 interaction lengths; together with the LAC and the coil SLD has at least 8 interaction lengths in any direction. The WIC consists of eight barrel section surrounding the coil in an octagonal fashion and two endcaps covering almost the entire solid angle around the interaction point.

In the center of the graphite coated plastic 9mm $\times$ 9mm streamer tubes there is a 100μm wire of BeCu held at 4.5kV in a gas mixture of 25% Argon and 75% Isobutane. On the top and bottom of the tubes there are stripes of G10 material plated with copper patterns in shapes of strips and pads. A

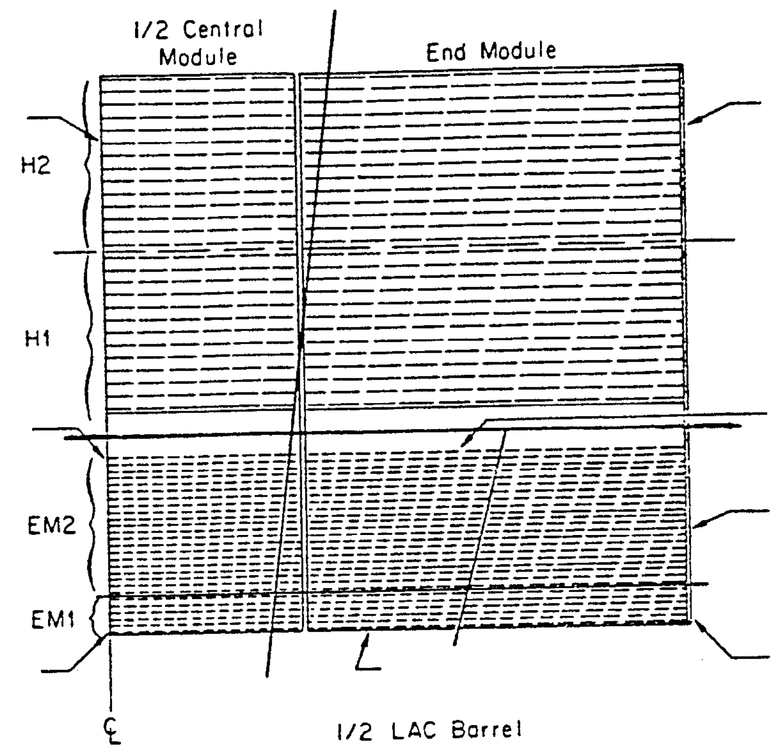

Figure 2.23 Tower Structure of the Calorimeter

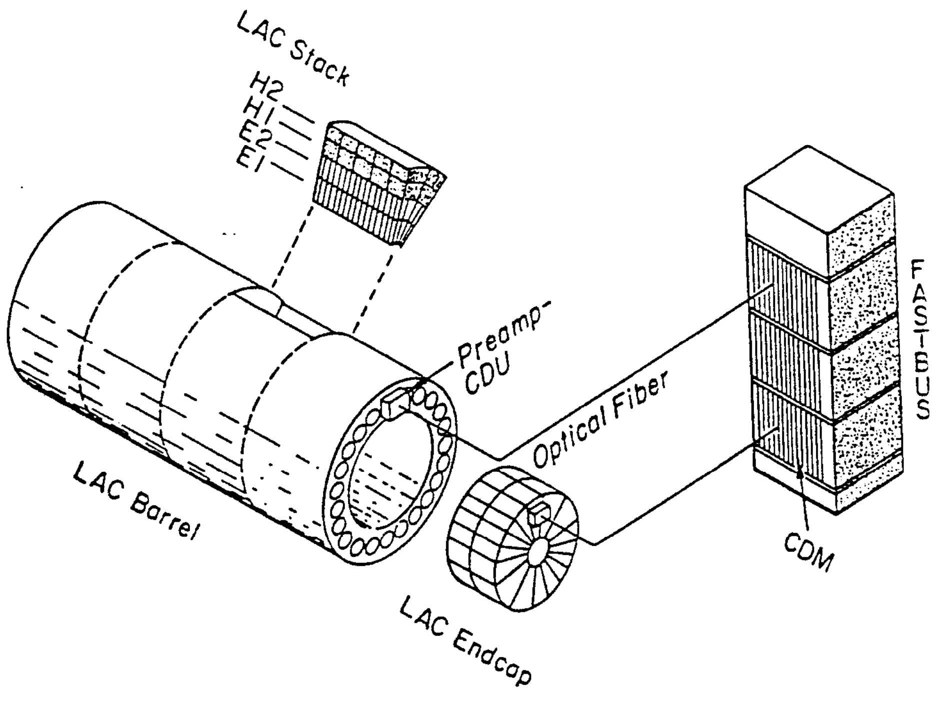

Figure 2.24 Liquid Argon Calorimeter

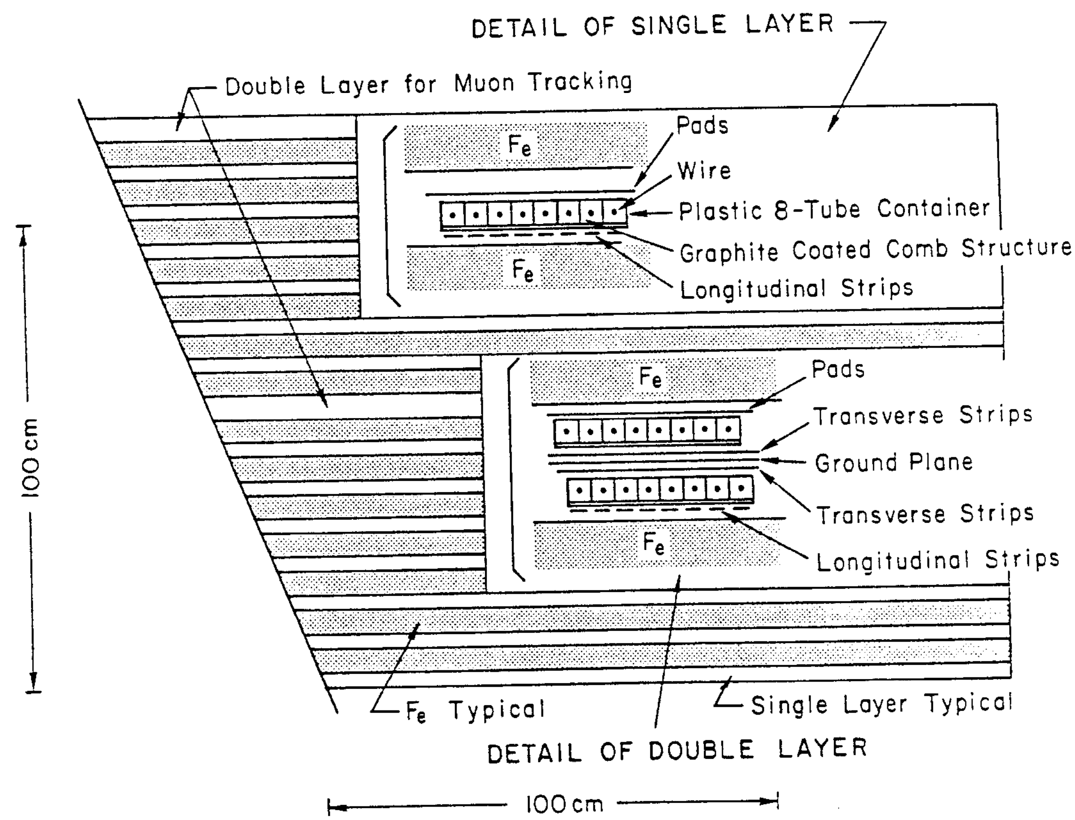

Figure 2.25 The Warm Iron Calorimeter measures the Hadronic Energy spilling over from the *LAC* and is used for muon tracking

charged particle passing through the gas mixture forms so called streamers, small lightnings from the high voltage wire to the surface, inducing charge in the copper circuits proportional to the energy of the particle, typically $12pC$ per streamer and about 7-8 streamers per GeV of energy.

In the eight coffins of the barrel section there are 17 layers of tubes. The strips run parallel to the tubes, except in layer 8 and 17 where they are perpendicular to them. They are read out digitally providing an exact tracking of the particles in $r - \phi$ and two points in z determining the angle of the muons to better than 10 mrad. The background of the muon identification comes from "punch through" hadrons, mainly π's with high enough energy. Pattern recognition and tracking capability for individual track can extrapolate the particles back to the drift chamber and is able to reduce the number of pions faking muons to the level of 2×10^{-3}, independent of the momentum. This contamination of punch-throughs is on the same order of magnitude as the expected decays in flight of π and K in the drift chamber and the $CRID$: 5×10^{-3} at 10 GeV/c and 1.7×10^{-3} at 30 GeV/c.

The geometry of the pads is a continuation of the hadronic tower structure of the towers in the LAC. The readout is analog, proportional to the energy deposited. They are squares of 265mm $\times$ 216mm on the inner most layer, increasing in size to 295mm $\times$ 316mm in the outer plane. The first eight layers are connected together to measure the energy flux in the "front tower" the remaining 7 layers form the "back towers". The energy resolution $\sigma(E)$ is $\sim 0.8\sqrt{E}$ (GeV). Since the typical energy deposited in the WIC is less than 30 GeV the resolution is on the order of $15 - 20\%$. The combined resolution of the LAC and the WIC calorimeters is 5.5% at an energy of 92 GeV.

The endcap region in the doors consist of eight horizontal and eight vertical layers of tubes read out in a similar fashion as the barrel with strips along each tube and pads in a tower structure. To cover the gaps between the endcaps and the barrel so called 45° chambers have been installed on the support arches. Along each section of the octagon there are two of these chambers, staggered by half a cell, 120 cm $\times$ 375 cm in size, with strips parallel and vertical to the tubes. The WIC contains a total of 101,488 stripes and 8640 towers covering 97% of the solid angle.

2.7.3 Luminosity Monitor

The Luminosity Monitor and Small Angle Tagger ($LMSAT$) and the medium angle silicon calorimeter ($MASC$) provide SLD's small angle electromagnetic coverage, measuring photons and electrons in the 23-200 mrad region (Fig. 2.26). The main function is to measure the integrated luminosity by precise tagging of Bhabha electrons, essential to measuring the mass and the widths of the Z^0 and any cross section in the experiment. With a total of 23 radiation lengths it simultaneously provides a low angle coverage for the calorimetry, specially important in photon-photon scattering. A secondary function of these devices is the shielding of the inner components of SLD from background radiation.

The $LMSAT$ and $MASC$ are cones of silicon detector centered around the beam pipe with a projective tower structure very much like the LAC. The $LMSAT$ covers the angles from 23 to 65 mrad and is about $1m$ from the interaction point, right in front of the Superconducting Final Focus $SCFF$. The $MASC$ covers the angles from 65 to 200 mrad and is right next to the vertex detector at $z = \pm 200$mm. On both devices each of the 23 layers of silicon detector is interspaced with tungsten plates of 1 radiation length. Like the electromagnetic part of the LAC the monitor is split up in EM1 and EM2,

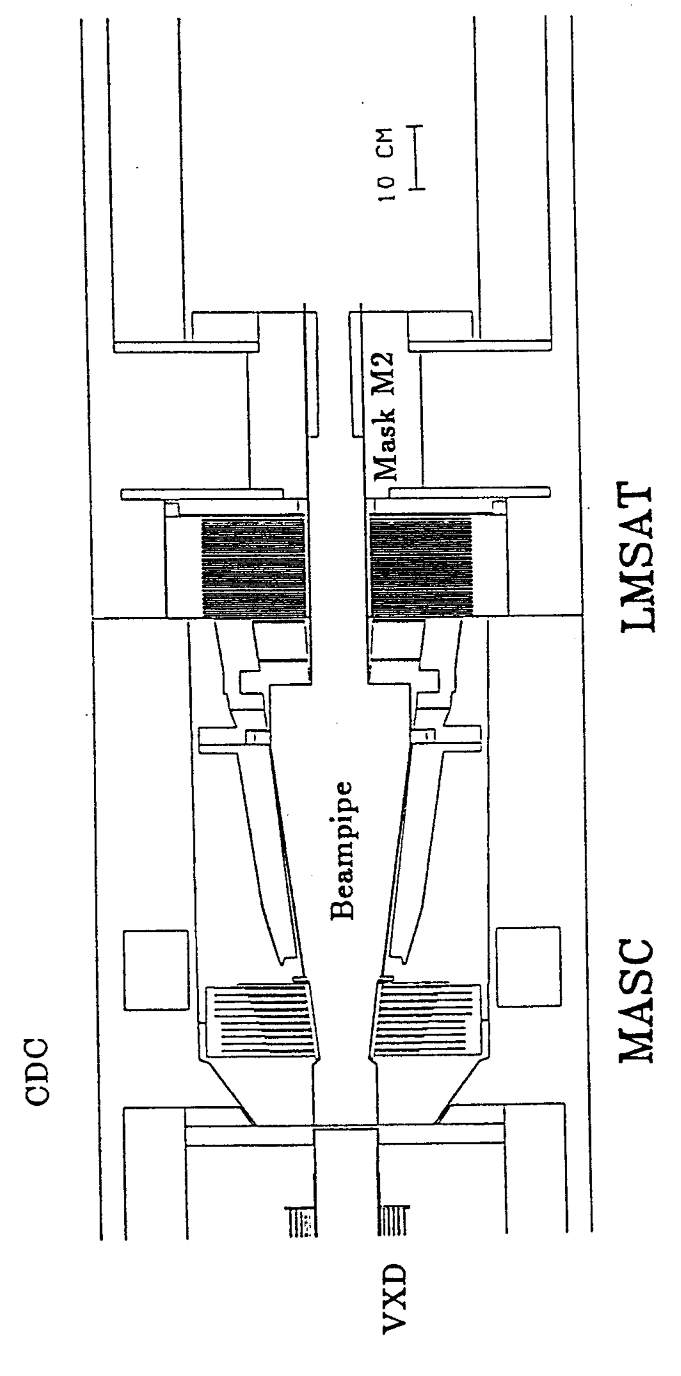

Figure 2.26 The Silicon-Tungsten Luminosity Monitors (LMSAT/MASC)

two sets of towers in front of each other. Measurements of Bhabha scattering and extensive EGS calculations determined an energy resolution of $23\%/\sqrt{E}$, and spatial resolutions of $\delta\vartheta = 0.3$ mrad and $\delta\phi = 6.5$ mrad.

2.8 Magnetic Coil

The magnet is a 5.9 m diameter and 6.4 m long coil situated between the LAC and the WIC. A current of 6600 A through 508 turns provide a magnetic field of 0.6 Tesla in the center of the coil. The iron structure of the WIC on the doors and the barrel serve as flux return. The Poisson-parametrization of the magnetic field in the coil

$$\begin{aligned} B_r &= B_r^0 \frac{rz}{r_0 z_0} \\ B_z &= B_Z^0 \; + \; 0.5 \; B_r^0 \; \frac{r^2 - 2z^2}{r_0 z^0} \end{aligned} \tag{2.7}$$

where $B_r^0 = 0.0214T$, $B_z^0 = 0.601T$, $r_0 = 1.2$ m and $z_0 = 1.5$ m agrees with the measured field to within 0.05% inside the volume of the CDC and to within 0.4% for the EDC. The uniformity of the field is more than adequate for the tracking measurements and the radial component of the field is small enough for the requirements of the $CRID$.

The dissipated power in the coil is 5 MW which is removed by cooling water flowing at a rate of 54 l/s. The coil weighs a total of 85 tons and exerts an attracting force of 240 tons on the endcap doors.

CHAPTER 3

EVENT SELECTION

3.1 Introduction

The events that were recorded on tape by the *SLD* were logged under highly variable beam conditions, different trigger configurations and with different active detector components. The data were recorded between March 1992 and September 1992. In a first step the hadronic Z^0 events had to be filtered out from the background. In a second step carefully determined cuts were applied to select a hadronic event sample suitable for this physics analysis. Monte Carlo studies were then made to estimate the backgrounds from various sources and the signal to noise ratio.

3.2 Event Trigger

Four different trigger types were used to select the events to be written to tape:

(*i*) the Energy trigger required a minimum deposited energy of 8 GeV* in the barrel and endcap *LAC* with an individual tower threshold of 60 ADC counts in the electro-magnetic section and 120 ADC counts in the hadronic section. Only towers above the trigger thresholds contributed to the trigger energy sum.

(*ii*) The Luminosity trigger required a minimum deposited energy of 10 GeV in each of two back-to-back towers in the luminosity monitor.

---

* The energy thresholds were changed several times. The values quoted here were used during most of the period of data taking

(*iii*) The Tracking trigger was activated when two or more tracks were detected in the CDC with an opening angle $> 20°$.

(*iv*) The Random trigger recorded events at the time of a beam crossing at a fixed rate of 1/20 Hz for the purpose of background studies.

The *standard* LAC energy scale applies to minimum ionizing particles like muons. In this scale, ADC counts convert to GeV as follows:

EM towers: 1 ADC = 2.04 MeV or 1 GeV = 489 ADC

HAD towers: 1 ADC = 5.41 MeV or 1 GeV = 185 ADC

Electrons are less efficient at depositing visible energy in the LAC, so the corresponding electromagnetic energy scale must be multiplied by the e/μ ratio = 0.7 to convert ADC counts into GeV. Hadrons deposit even less visible energy, so the hadronic energy scale must be multiplied by about 0.5 (e/π ratio = 1.4).

The trigger rate was typically between 0.5–2 Hz, depending on the beam conditions. To reduce the trigger rate and hence to increase the livetime of the detector (the fraction of the time in which the detector is able to take a new event), it was often required that the energy trigger and the tracking trigger fired at the same time, for an event to be written to tape, with the requirement of ≥ 1 track in the CDC.

3.3 Z Event Selection

In a first pass the raw data of the events that had satisfied the trigger conditions were run through several offline filter programs to select hadronic Z^0–candidates, τ–pairs, wide angle Bhabha, Bhabha events in the luminosity monitor and μ–pairs. Events of various types are shown in Figures 3.1.-3.4.

For an event to pass the hadronic Z^0 filter it had to meet the following criteria:

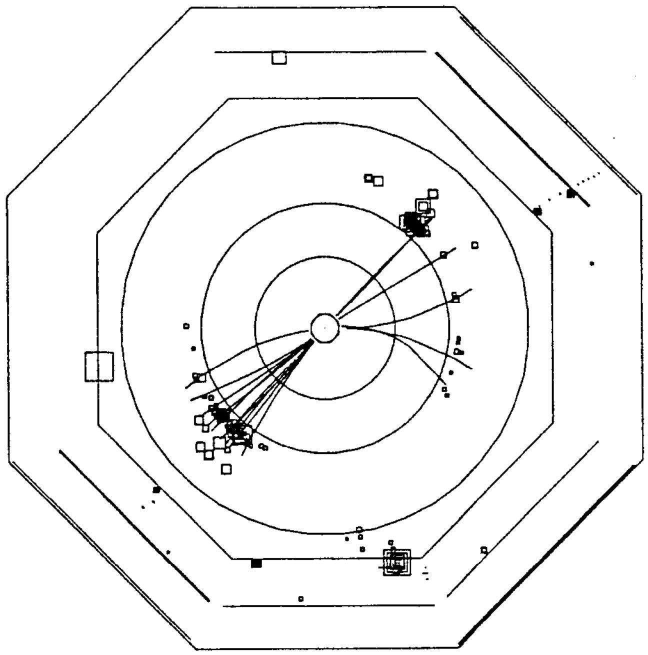

Figure 3.1. Hadronic Z^0 event. The track in the upper right-hand quadrant of the WIC indicates a muon with a high transverse momentum from a semi-leptonic decay of a heavy quark.

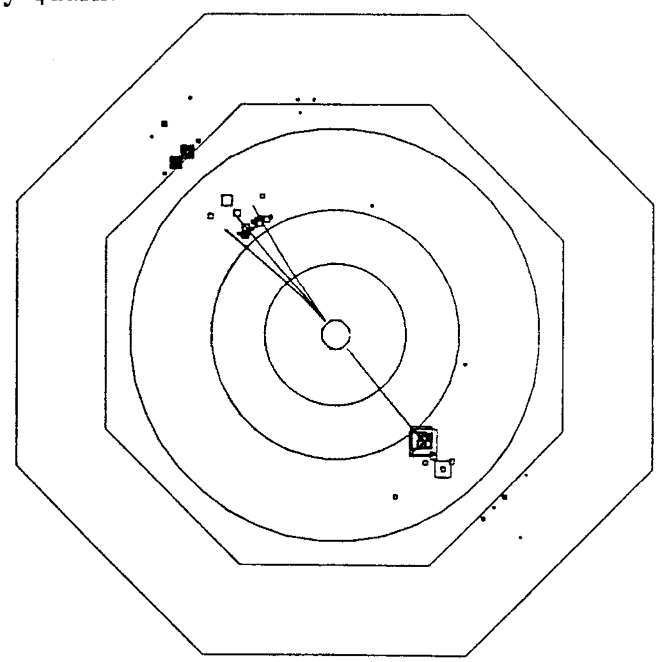

Figure 3.2. $\tau^+\tau^-$–pair. One τ^- decayed into an electron and two neutrinos, indicated by a single track and a large amount of energy deposited in the electromagnetic section of the LAC, the other τ decayed into three hadrons ($\pi^+\pi^+\pi^-$) and a ν_τ indicated by the three tracks in the CDC and the energy deposited in the hadronic section of the LAC and the WIC.

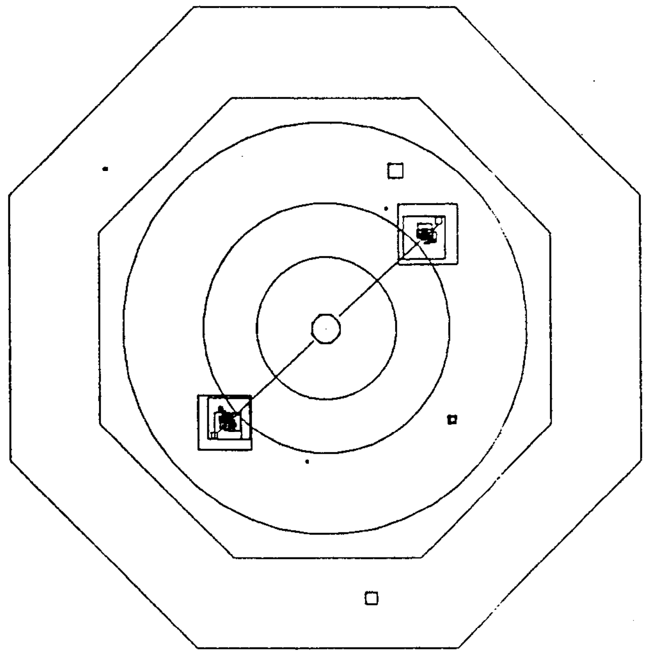

Figure 3.3. Wide Angle Bhabha event ($e^+e^- \rightarrow e^+e^-$). This event is characterized by two back-to-back hight momentum tracks in the CDC and all the energy deposited in the electromagnetic section of the LAC

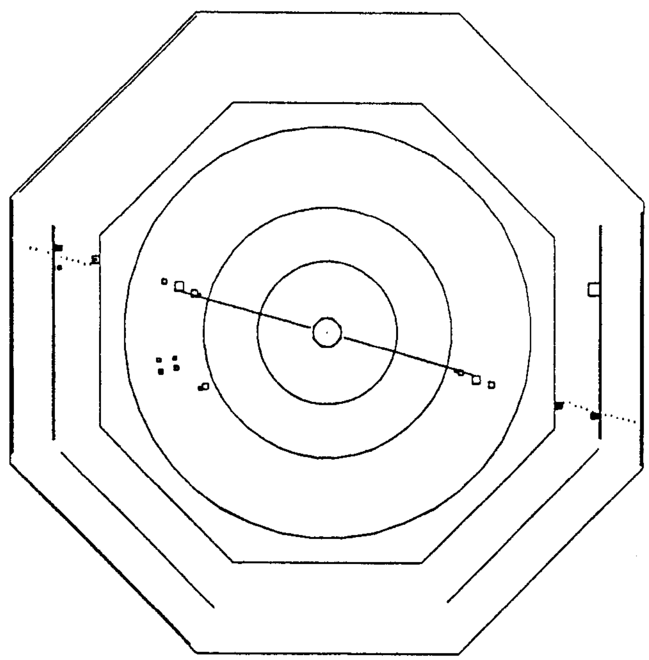

Figure 3.4. $\mu^+\mu^-$-pair indicated by two 45 GeV tracks in the CDC, small amounts of energy deposited in both sections of the LAC, consistent with a minimum ionizing particle and two tracks extrapolating through the WIC.

(*i*) the total energy in the barrel and endcap LAC, $E_{LAC} > 14\text{GeV}$,

(*ii*) the energy in the endcap WIC $E_{WIC} < 11\text{GeV}$, to veto events with excessive muon showers parallel to the beam axis,

(*iii*) the energy imbalance and sphericity S, $E_{imbal.} < 0.9$ and $(E_{imb.}+S) < 1$. The event was divided in two hemispheres by the plane perpendicular to the sphericity axis and the energy imbalance defined as

$$E_{imb.} = \frac{E_{hem(1)} - E_{hem(2)}}{E_{hem(1)} + E_{hem(2)}} \tag{3.1}$$

These criteria were used to filter out so-called *Monojet* events which were caused by beam-related events such as beam-wall interactions and beam muon backgrounds. These kind of events are very asymmetric, since the underlying reactions are boosted in the beam direction. This filter would not distinguish between hadronic events and tau pairs decaying into hadrons.

Wide Angle Bhabha events were selected by requiring back to back clusters in the electro-magnetic section of the LAC, each with energies of more than 10 GeV. Since the showers are purely electro-magnetic, very little or no energy is deposited in the hadronic sections.

To identify a $\mu^+\mu^-$-pair, two back to back tracks were required in the CDC with corresponding extrapolated tracks in the WIC pads. The distance of closest approach to the IP along the beam direction was required to be smaller than 1cm and the momentum of the tracks greater than 10GeV.

The events passing these cuts were then fully reconstructed and written to data summary tapes.

In a second pass a set of cuts were applied to select the events suitable for this physics analysis:

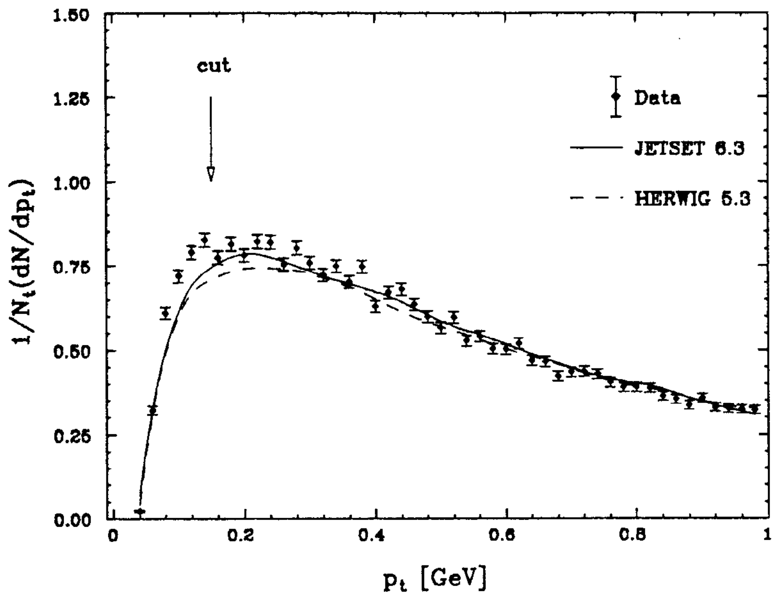

Figure 3.5. Transverse track momentum spectrum

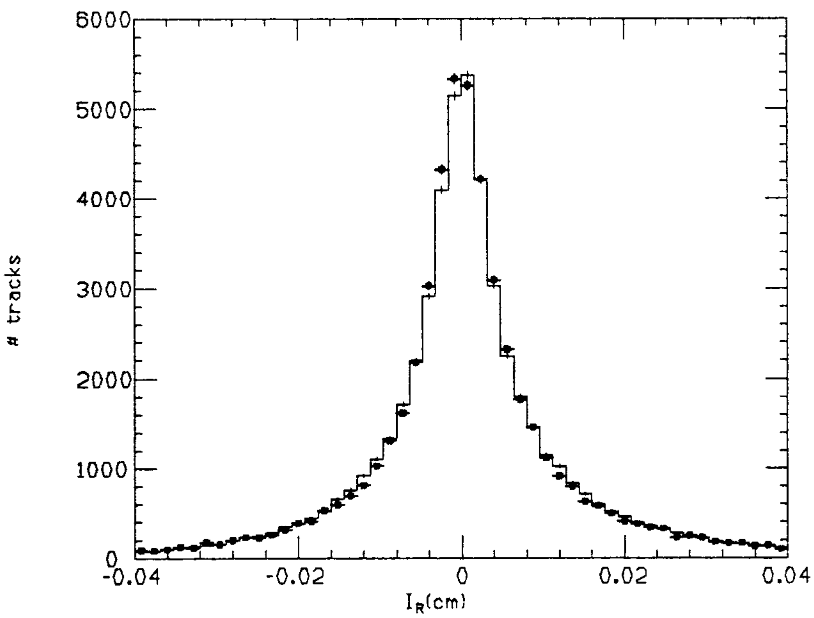

Figure 3.6. r–coordinate of Impact parameter

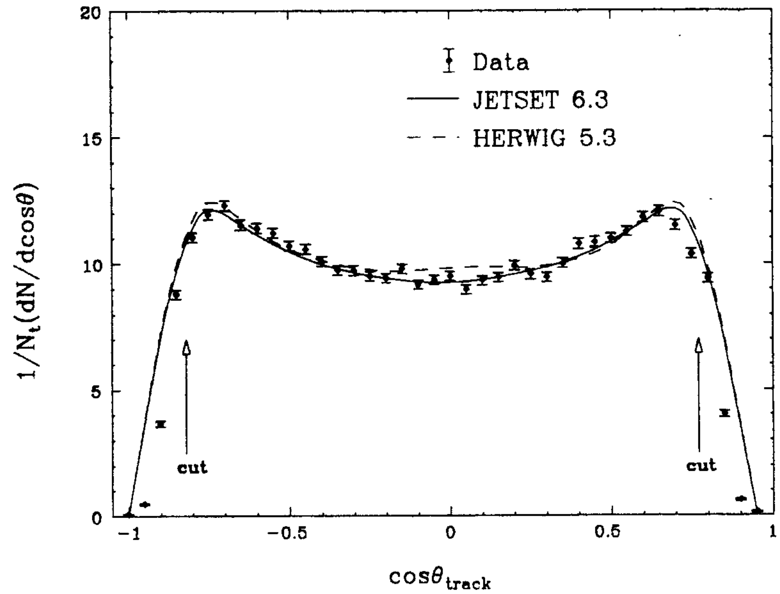

Figure 3.7. polar angle $\cos\theta$ of the charged tracks with respect to the beam axis.

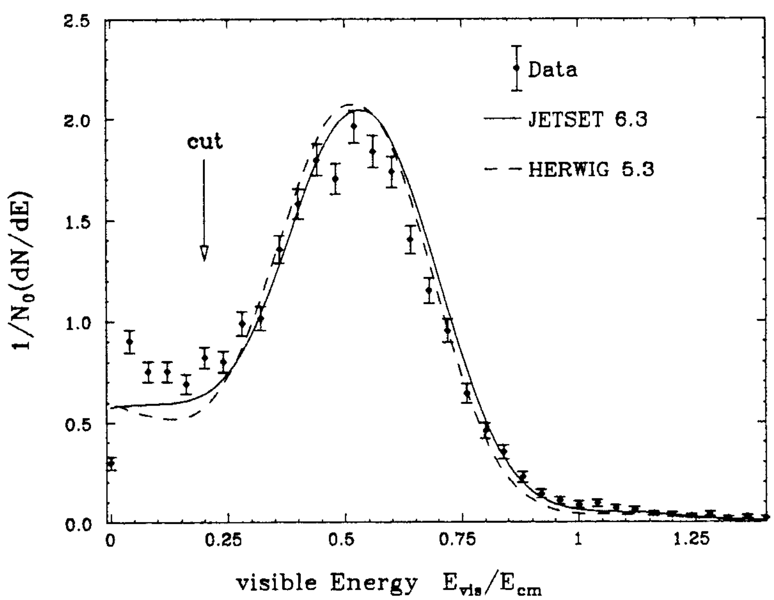

Figure 3.8. charged energy E_{vis} over center of mass energy

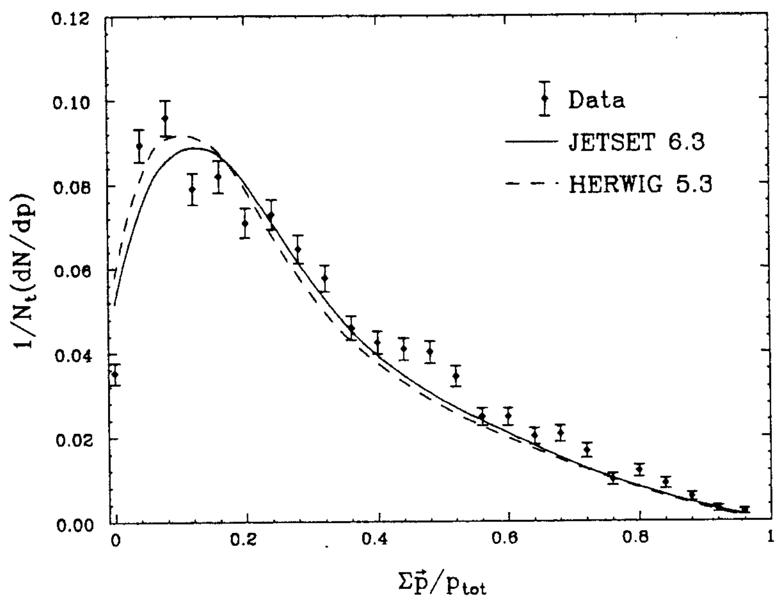

Figure 3.9. vector sum of the track momenta divided by the sum of absolute value of track momenta

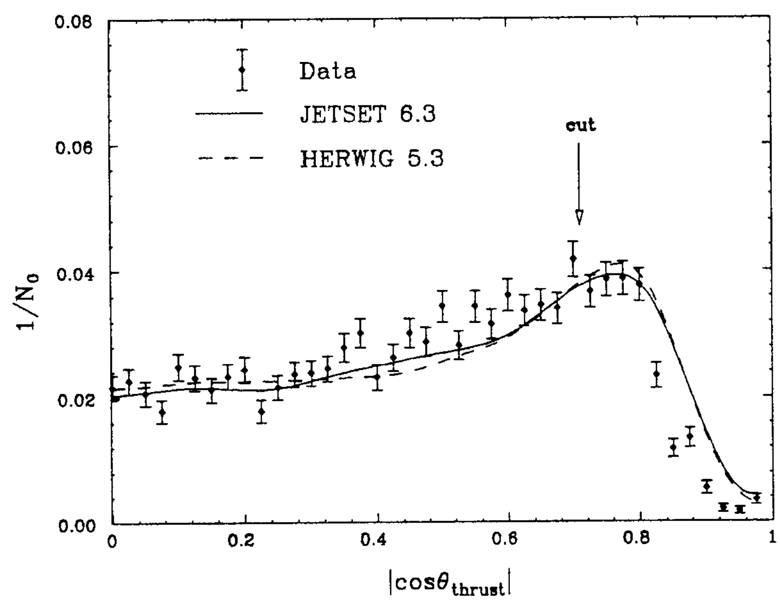

Figure 3.10. $|\cos\theta_t|$ of thrust axis

(i) Tracks were required to have a transverse momentum of at least $p_t > 150$ MeV. Figure 3.5 shows the transverse track momentum with respect to the beam axis. It is apparent that the Monte Carlo simulation of hadronic Z^0 events underestimates the number of tracks in the low transverse momentum region. These low momentum tracks are mostly originating from conversions and multiple scattering and are very hard to model exactly.

(ii) Tracks were also required to have a closest approach to the beam axis within 5 cm, and

(iii) within 10 cm along the beam axis of the nominal interaction point (Fig. 3.6) to insure that they originate from the proximity of the interaction point,

(iv) and have polar angle in the range $25° < \theta < 155°$ (Fig. 3.7). Cut *iv* guarantees that the tracks are well contained in the active region of the CDC. The track reconstruction efficiency outside this region drops off significantly as the angles with respect to the beam axis gets smaller and is not well modeled by Monte Carlo simulations.

Hadronic events were selected by requiring

(v) at least five charged tracks (Fig. 4.1)

(vi) a total charged energy of at least 20% of the center of mass energy E_{cm} (Fig. 3.8).

(vii) that the thrust axis be in the range $35° < \theta_t < 145°$ (Fig. 3.10). The thrust T is defined by

$$T = \max\left(\frac{\sum_i |\vec{p}_i \cdot \hat{n}|}{\sum_i |\vec{p}_i|}\right) \tag{3.2}$$

where i runs over all tracks, and the thrust axis $\hat{n}$ is chosen to maximize the value of T. For a back-to-back two-parton final state T has the value of 1. For planar three parton final states T is in the region $^2/_3 \leq T \leq 1$, and for nonplanar multi-jet events the T value can be as low as $^1/_2$.

The last two cuts ensure that the events are well contained in the active region of the detector and only a small number of tracks lost due to finite acceptance or tracking inefficiencies. In the data we observe a number of events with visible charged energy of less than 10% of the center of mass energy. Most of these events lie close to the beam direction losing multiple tracks down the beam pipe or into non-sensitive regions of the detector. In Figure 3.8 we observe an excess of these very low energy events that are not simulated by the Monte Carlo. Some of these events are background events produced when electrons or positrons from the incoming beams interact with gas in the beam line or with the beam pipe wall. Requiring $E_{vis}/E_{cm} > 0.2$ eliminates this source of background nearly entirely (see next section). Events with a thrust axis close the the beam direction are not well reconstructed due to the decreasing efficiency of the CDC in the forward region. It can be seen in Figure 3.9 that the Monte Carlo simulations do not reproduce the data very well in the region of $\cos\theta_{thrust} > 0.8$ and it was therefore chosen to exclude these events from this analysis. This analysis does not use tracks found in the EDC's, since these were still being commissioned during this run.

In addition it was considered to require that the momentum imbalance, defined as the vector sum of the track momenta divided by the sum of absolute value of track momenta, be smaller than 0.75. But it is evident from Figure 3.9 that the momentum imbalance is well simulated by the Monte Carlo and can be corrected for as described in the following chapter. This cut only reduces the statistics of the measurement without eliminating any backgrounds and was therefore not used in this analysis.

cut	# tracks	effic. Data	effic. MC
$p_t > 150$MeV	179,775	88.5	88.6
$I_z < 10$cm	162,195	80.2	80.4
$25° < \theta < 155°$	144,226	71.1	71.7
	# events	effic. Data	effic. MC
# of tracks ≥ 5	8928	92.4	93.2
$E_{vis}/E_{cm} > 0.2$	7545	82.8	84.7
$35° < \theta_t < 145°$	5500	65.8	66.5

Table 3.1 List of cuts and their efficiencies on Data and Monte Carlo

A summary of these cuts and their efficiencies is listed in table 3.1. Out of a total of 11679 Z^0 candidates that passed the hadronic filter, 8928 contained CDC information and 5500 events with an average of 18.2 tracks per event passed all the above analysis cuts.

3.4 Backgrounds

It is necessary to estimate the contamination of the final event sample arising from background events which pass the cuts described in section 3.3. The major source of background are $\tau^+\tau^-$ pairs, two-photon events and beam-related events.

The main decay modes of τ's are semileptonic: $\tau^\pm \to l^\pm \nu_l \nu_\tau$ where $l = e, \mu$, or hadronic: $\tau \to K/\pi\nu_\tau$. In 86.1% of all cases, the τ decays into one charged and multiple neutral particles ("1-prong").[11] In 13.8% it decays into three charged daughter particles and one or more neutral particle ("3-prong"). By requiring at least 5 charged particles in an event, one therefore expects to cuts out 98.1% of all $\tau^+\tau^-$ events. Nevertheless, other tracks can be generated through radiative photon conversions or interactions in the detector material. To study this, a large number of Monte Carlo τ-events were generated and subjected to the same selection criteria and cuts as the hadronic Z^0-events. It was shown that $4.2\% \pm 0.13\%$ of the τ–pairs passed the cuts, a slightly larger fraction than the expected 1.9%. Together with the branching ratio of $Z^0 \to \tau^+\tau^- / Z^0 \to \text{hadrons} = 4.7\%$, the contamination of the data sample by τ events was estimated to be $0.2\% \pm 0.07\%$.

Two-photon events are generated in the process $e^+e^- \to e^+e^- + \gamma\gamma$, $\gamma\gamma \to$ hadrons. These events occur rather frequently, but only few are energetic enough and at a large enough angle away from the beam axis to actually trigger the detector. The cross section for this process has been calculated[47] and, for $Q^2 > 5$ GeV, determined to be 4.5 nb at the Z^0, or about $1/5$ of the hadronic cross section. Two-photon events with a $Q^2 < 5$ GeV would not trigger the detector. Two-photon events can be simulated with a special Monte Carlo program.[48] Applying the same cuts on these events as are applied to the hadronic events, just as described for the τ background, eliminates about 99.5% of them. Multiplying the remaining $1/2\%$ by the ratio of cross sections of two-photon to hadronic events we estimate the background from this source to be of the order of 0.1%

Beam-related events, where an electron or positron from the beam interacts with the wall of the beam pipe or with a nucleon of a residual gas atom in the beam pipe vacuum, occur rather frequently. The characteristics of these events are multiple low momentum tracks. Most beam-related events can readily be identified as such due to their high momentum imbalance. It is not possible to calculate any cross sections for these events, since their production rate is heavily dependent on the beam conditions which can vary considerably over just a short period of time. The study of Monte Carlo simulation of such events indicate that a cut on the number of tracks and on the minimum charged energy in the event, but particularly a cut on the momentum imbalance, eliminates practically all such events. From these simulations one can estimate the ratio of *obvious* beam-related events to events that pass all the cuts, faking a hadronic event. Measuring the event rate of these *obvious* events in the data sample, one can estimate the number of residual background events in the final event sample. This method is not very precise but is appropriate since the contamination of the event sample by beam-related events is $< 0.1\%$ and is therefore negligible.

$\sqrt{s} = 91.1\text{GeV}$	$Z^0 \rightarrow$ hadrons	$\tau^+\tau^-$-pairs	$\gamma\gamma$-events	beam-gas
σ (nb)	41.8	0.99	4.5	–
acceptance (%)	65	4.2 ± 0.13	0.5 ± 0.1	0.09 ± 0.01
# of events	5500	18	9	< 10
signal/background (%)	> 99.5	0.2 ± 0.07	0.1 ± 0.03	< 0.1

Table 3.2 Z^0 events and Backgrounds

CHAPTER 4

ANALYSIS AND RESULTS

4.1 Introduction

The hadronic Z^0 decay into final state particles collimated into two, three or more jets as shown in Figure 1.6–1.8. They can be interpreted in terms of the production and fragmentation of quarks and radiated gluons described by perturbative QCD calculations. The boundaries between these different classes of multi-jet events are diffuse, both from a theoretical and experimental point of view. The spectrum of gluons produced ranges from hard (high transverse momentum p_t) to arbitrarily soft (low p_t) gluons. In the calculation of the cross section, the latter case introduces a divergence in the integration over the gluon momentum in the limit $p_g \rightarrow 0$. This is effectively removed by introducing a lower cutoff in the gluon momentum and angular spectrum due to the experimental condition that allows one to separate a gluon from its parent quark. This reduces the number of partons counted in the final state. The number of partons therefore depends on the value chosen for this cutoff parameter. Experimentally this has no effect if this cutoff value is chosen to be reasonably small. Such soft partons cannot be resolved as separate jets because of the smearing introduced by fluctuations in the hadronization process and experimental resolution. The experimental separation of two jets also depends on the angle between them. Even if a gluon carries a momentum comparable to that of the quark, the resulting jets start overlapping when the angle between them gets sufficiently small. They can then no longer be resolved into two distinct jets.

In this chapter it is described how the number of jets in an event is determined as a function of a resolution cutoff y_{cut} and how the theoretically predicted jet rates are fitted to data after correcting it for hadronization and detector effects, such as acceptance and resolution.

4.2 Simulation of the Data by Monte Carlo Calculations

In chapter 1 several Monte Carlo (M.C.) programs were described and in the previous chapter the M.C. was used to estimate the contamination of the data by various background sources. In order for the M.C. to be an effective tool, it must foremost provide a good simulation of the data to which it is compared. There are a large variety of options provided by JETSET for simulation of the evolution and fragmentation of partons. Here, the default options were used, by which the original quark-antiquark pair created in the e^+e^- annihilation initiates a parton shower described in chapter 1.7.1 by which the transition from partons to hadrons occurs according to the Lund string model for fragmentation.[49] JETSET incorporates a procedure by which the first gluon branching in the leading logarithmic shower is mapped onto the first order matrix element distribution for $e^+e^- \to q\bar{q}g$. This feature is intended to compensate for the underestimation of the rate of hard, acollinear gluon emissions by the leading log approximation.

The main parameters of JETSET which control the momentum distribution of the hadrons are listed in Table 4.1. The parameter Λ_{QCD} is the QCD scale parameter, whose value determines the extent to which partons will branch. Q_0 specifies the minimum mass squared value to which partons may evolve and it serves to terminate the shower. The three parameters σ_q, a and b belong to the fragmentation phase, controlling the transverse and longitudinal momentum spectrum of hadrons with respect to the underlying string directions. These parameters were optimized by the OPAL collaboration[51] to describe experimental distributions from the data at the Z^0 resonance in the best possible way, such as charged track multiplicity, n_{ch}, shown in Figure 4.1, and event shapes, such as thrust T, (eq. 3.2) shown in Figure 4.2.

Parameter	Monte Carlo name	Default value	Optimized value by OPAL
Λ_{QCD}	PARE(21)	0.40 GeV	0.29 GeV
Q_0	PARE(22)	1.0 GeV	1.0 GeV
σ_q	PAR(12)	0.35 GeV	0.37 GeV
a	PAR(31)	0.50	0.18
b	PAR(32)	$0.90\mathrm{GeV}^{-2}$	$0.34\mathrm{GeV}^{-2}$

Table 4.1 The main parameters of JETSET version 6.3 which control the momentum distribution of hadrons.

The main parameters of HERWIG for the control of the momentum spectra distributions of hadrons are given in Table 4.2. The QCD scale parameter Λ_{QCD} specifies the likelihood or branching in the shower. m_g is a formal mass value assigned to the gluon, serving to terminate the perturbative evolution. M_{max} is a threshold parameter which determines whether a large mass cluster will evolve through a stringlike mechanism to lower mass clusters rather than decay to hadrons directly.[50]

Apart from the physics that describes the decay of the quarks into final state hadrons, the Monte Carlo program must simulate the effects of the detector. The *SLD* simulation program is based on the GEANT3 package[57] developed at CERN. Particles are tracked through a detailed

Parameter	Monte Carlo name	Default value	Optimized value
Λ_{QCD}	QCDLAM	0.20 GeV	0.11 GeV
m_g	RMASS(13)	0.65 GeV	0.65 GeV
M_{max}	CLMAX	5.0 GeV	3.0 GeV

Table 4.2 The main parameters of HERWIG version 5.3 which control the momentum distribution of hadrons.

model of the *SLD* simulating the effects of energy loss, secondary decays, Bremsstrahlung, Compton scattering, multiple scattering, delta-ray production, gamma conversions, hadronic interactions, photoelectric interactions and positron annihilation. As an end result we obtain M.C. events in the same format as the real events collected with our data acquisition system. Close attention was paid to details to ensure a good agreement between the data taken with the *SLD* and the M.C. simulation thereof. The *measured* resolutions in the drift chamber such as the charge division resolution, drift time resolution and momentum resolution were used in the M.C. to reconstruct the simulated data. Other effects such as readout electronics that were not operational during part of the run or high voltages that were off for an entire superlayer of the CDC were simulated by reproducing these effects in the M.C. with the appropriate probability as determined in the real data. Background noise, which was measured during beam crossings where no collisions occurred, could be overlayed over the M.C. event. The noise level could be varied in terms of the total drift chamber occupancy. It was shown that random noise making hits on up to 20% of all the CDC's sense wires did not affect the overall performance of the track reconstruction. During the data taking close attention was paid to keep the CDC occupancy below 10% for most of the time.

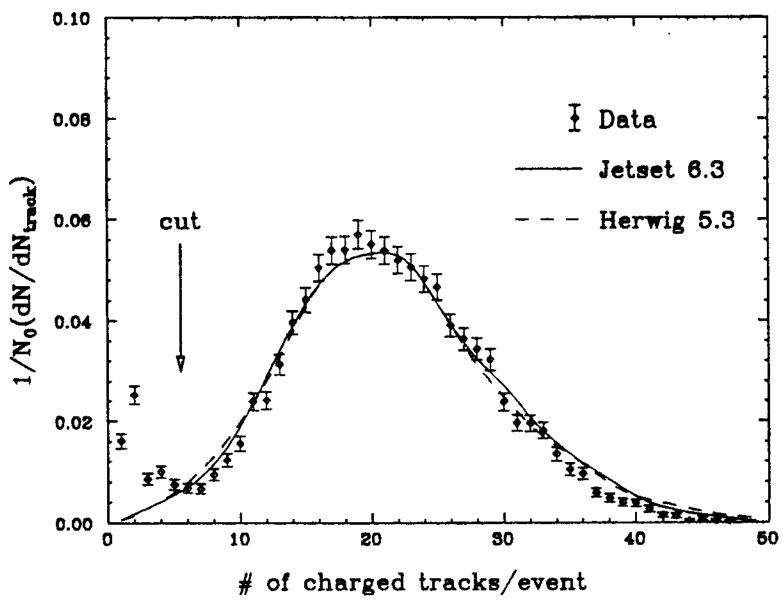

Figure 4.1 Comparison of data with JETSET (solid) and HERWIG (dashed) M.C. simulations.

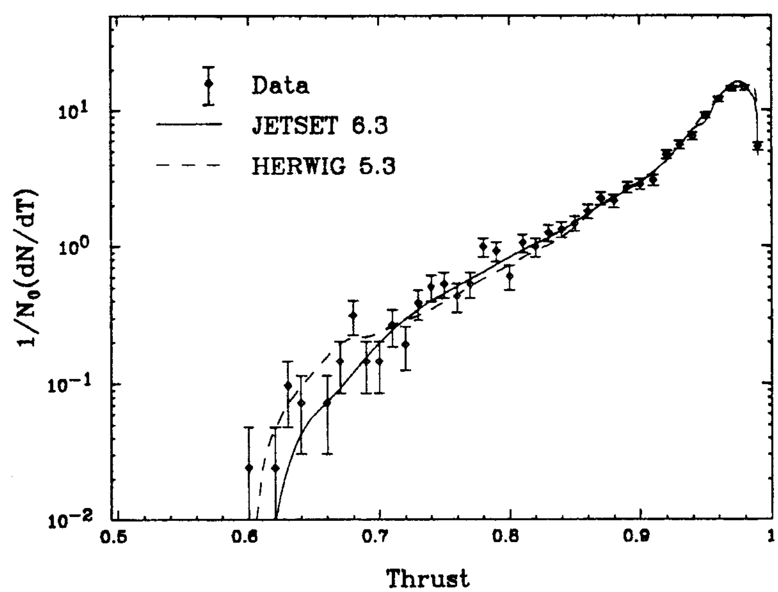

Figure 4.2 Thrust distribution T (eq. 3.2), the points with error bars are the SLD data, the solid histogram was obtained from the JETSET M.C. and the dashed histogram from the HERWIG M.C.

4.3 Jet-finding Schemes

A jet algorithm must be able to specify unambiguously a jet configuration starting from particles detected in the final state. A jet algorithm may be defined giving

(i) a test variable (e.g. energy, angle or combined mass) y_{ij}, and

(ii) a recombination procedure.

The test variable y_{ij} is needed in order to specify whether or not two hadrons h_i, h_j belong to the same jet, while the recombination procedure tells us how to combine particles, which the test variable y_{ij} tells us belong to the same jet.

One possible way to define jets in events is the "JADE algorithm",[52] It has been the most widely used jet finder, but recently, other algorithms have been suggested by theorists at Durham[53] and at CERN.[54]

The JADE algorithm is an iterative process: in the first step the scaled "invariant mass" y_{ij} of every pair of particles is calculated, assuming all hadrons to be massless:

$$y_{ij} = \frac{2E_iE_j(1-\cos\theta_{ij})}{E_{vis}^2}. \tag{4.1}$$

E_i and E_j are the particle energies and θ_{ij} the angle between them. E_{vis} is the total visible energy in the event. The usage of E_{vis} in the denominator, rather than E_{cm}, makes the measure less sensitive to detector acceptance corrections and event-to-event fluctuations. Particles can be charged tracks in the drift chamber, in which case E_{vis} is the charged energy only, or energy clusters in the calorimeter, in which case E_{vis} is the total energy measured in the calorimeter. But the jet algorithm can also be applied to partons or hadrons generated by the Monte Carlo.

In the second step the pair with the smallest invariant mass y_{ij} is combined into a pseudo-particle or cluster k by adding their four-momenta together:

$$p^k = p^i + p^j \tag{4.2}$$

The event now has one less particle.

Then step 1 is repeated, treating the newly found cluster like the other particles, calculating the invariant mass between the cluster and the other particles. This iterative procedure is continued until all scaled invariant masses $y_{ij} > y_{cut}$, where y_{cut} is the cutoff value handed to the jet-finder by the user. At this point all particles within a cluster have invariant masses $< y_{cut}$ and the invariant masses of all clusters are $> y_{cut}$. The clusters or particles at the end of this process are what we define as jets. The number of found jets is clearly a function of the cutoff, y_{cut}. The smaller the value of y_{cut}, which is a measure of the jet mass, the larger the number of jets. In the limit of $y_{cut} \to 0$ every particle is an individual jet. Increasing y_{cut} from 0.01 to 0.1 the numbers of 4-jet and 5-jet events quickly drop, while the number of 2-jet and 3-jet events increase. For an even higher y_{cut} the softest of the 3 jets is more likely to get merged with one of the two other jets, and in the limit of $y_{cut} \to 1/3$ the 3-jet rate vanishes altogether. For $y_{cut} > 1/3$ the phase space for 3-jets is 0. The jet rates as a function of y_{cut} for the *SLD* data are depicted in Figure 4.3.

Theoretical calculations of 2-,3- and 4-jet production rates, using the same definition of resolvable jets in terms of jet pair masses, are available only for massless jets in $\mathcal{O}(\alpha_s^2)$ QCD. Since jets which are formed by adding the four-momenta of two unresolved particles are not massless, other algorithms have been suggested, which differ in their prescription of how to combine the momenta of the particles. Commonly used variations on the JADE algorithm

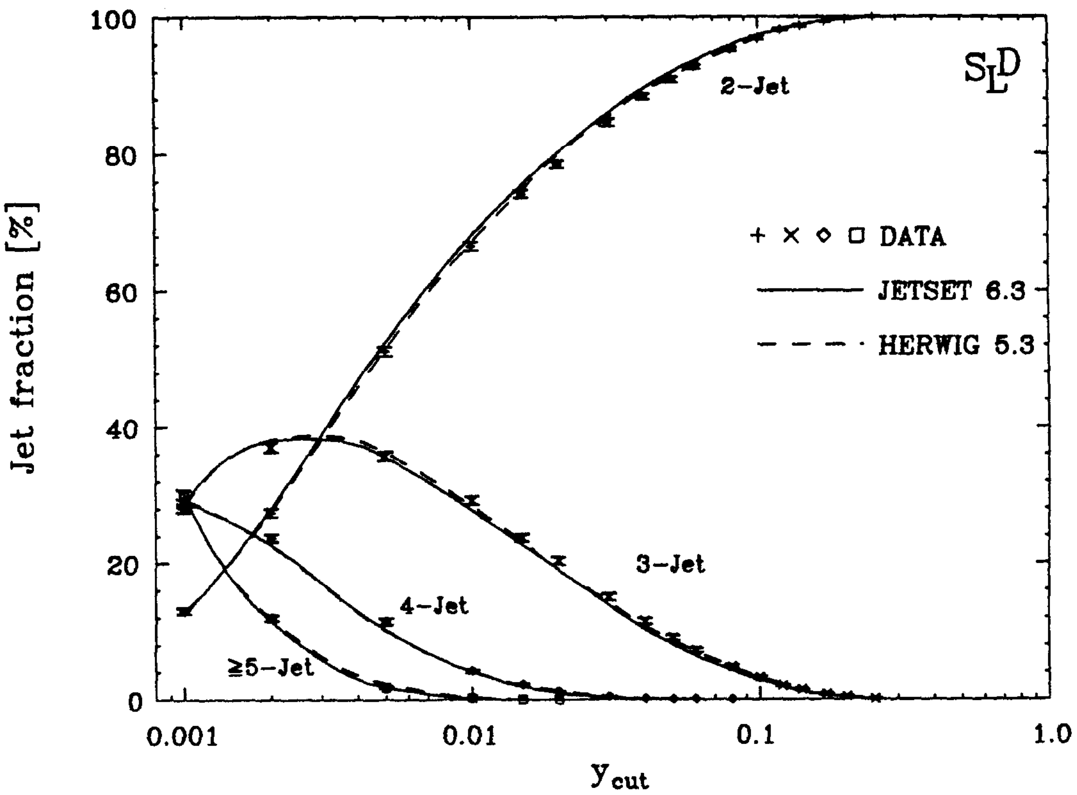

Figure 4.3 n-jet rates as a function of y_{cut}obtained with the Durham algorithm (described below) from reconstructed data and M.C. simulation. A small value for y_{cut} is equivalent to high jet resolution and hence a higher average number of jets. As y_{cut} is increased the phase space for 5-jet and 4-jet topology is reduced and subsequently vanishes. The two jets with lowest invariant mass are more likely to be combined into a single jet. Therefore the 2-jet and 3-jet rate increase with rising y_{cut}. For even higher y_{cut} the 3-jet rate starts decreasing again until the phase space vanishes altogether at $y_{cut} = 1/3$ and all events are resolved as a 2-jet event.

are the "E", "E0" and "p" schemes. In these variations the recombination criterion y_{ij} of eq. 4.1 is replaced by

$$y_{ij} = \frac{(p_i^\mu + p_j^\mu)(p_{i,\mu} + p_{j,\mu})}{E_{vis}^2}. \tag{4.3}$$

This is the same as eq. 4.1 if the particles i and j are massless, but it differs if either of the jets has a non-zero mass. In the E-scheme, one uses eq. 4.3 along with eq. 4.2 for the combining of the particles. The E-scheme is Lorentz invariant, but ends up with massive jets, which cannot be accounted for in the calculations. In the E0 and p algorithms, one uses eq 4.1 as the resolution criterion, but changes the four-momentum combination by modifying either the total jet three-momentum or the total jet energy, respectively. This results in massless jets, but they do not conserve the overall momentum or energy sum. The original JADE jet finder is equivalent to the E0 scheme and yields practically identical results. A summary of the jet-finding schemes is given in Table 4.3 at the end of this section.

The success of these and similar algorithms is mainly due to the fact that the hadronization of the parton final states can be shown to have, on average, little influence on the number of found jets. On the other hand, the substantial renormalization scale dependence of the three-jet rate, which has been calculated to next-to-leading order,[17] indicates that perturbative corrections beyond the order calculated are not yet negligible. Since calculating jet rates to even higher orders is not yet a viable option, due to the complexity of the computation, one was motivated to find new definitions of jets which would lead to smaller perturbative corrections while maintaining the insensitivity to hadronization of the original JADE scheme.

A more intuitive picture of the problems arising with the JADE algorithm

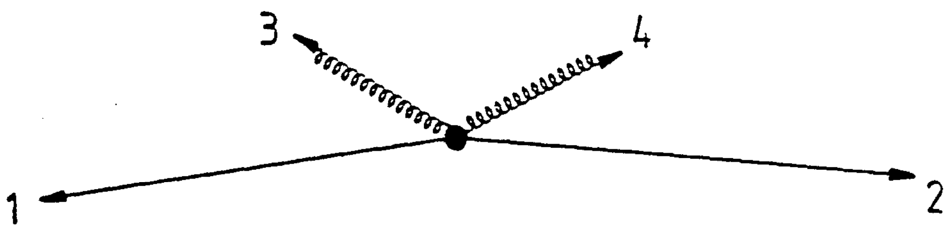

Figure 4.4 A $q\bar{q}gg$ configuration which the invariant mass algorithm assigns to a three-jet final state. The D-algorithm first combines the a g with the q and the other g with the $\bar{q}$ to form a two-jet final state.

is given in a paper by N. Brown and W.J. Stirling.[54]: QCD processes radiate numerous soft gluons. The JADE scheme tends to merge the hadronized particles from these gluons into one jet, due to their small combined mass y_{ij}, even though they may have a large angle between each other, rather than combining them with the hard hadron from which they were emitted. The result can be an "artificial" jet made of soft particles (Fig. 4.4). It also has the effect of producing an unnatural partitioning of the multi-parton final state which greatly complicates the calculation of jet production rates for small values of y_{cut} .[53] In the same paper it was proposed to replace the product of the particle energies in eq. 4.1 by the square of the smaller of the two energies:

$$y_{ij}^{D} = \frac{2 \cdot \min(E_i^2, E_j^2)(1 - \cos\theta_{ij})}{E_{vis}^2}, \tag{4.4}$$

which, in effect, clusters according to the minimum relative transverse momentum of the parton pair rather than the invariant mass. Together with the recombination process in eq. 4.2 this is called the "Durham" or D–scheme. It has been shown that with the Durham algorithm a soft gluon will only be combined with another soft gluon, instead of being combined with a high energy parton, if the angle it makes with the other soft gluon is smaller than the angle that it makes with the high energy particle. This algorithm improves the theoretical analysis at smaller values of the resolution parameter y_{cut} because the leading double logarithms exponentiate, greatly facilitating the calculations .[53] In Fig. 4.5 the transverse momentum of tracks are displayed with respect to the axis of the jet they belong to, evaluated at $y_{cut} = 0.02$. For increasing values of y_{cut} the average transverse momenta in the jets increase, shown in Fig. 4.6. The data points are compared with the M.C. simulations and are found to be in good agreement.

Another possible definition of y_{ij} was suggested by S Bethke et al.:[55]

$$y_{ij}^{G} = \frac{8}{9}\frac{E_i E_j(1-\cos\theta_{ij})}{(E_i+E_j)^2}. \tag{4.5}$$

This algorithm uses the same recombination scheme as does the JADE and Durham routines and is called the "Geneva" (G) algorithm. (The factor 8/9 is provided so that the maximum value of y_{cut} for which three jets can still be obtained from three partons is $1/3$, as it is for the JADE and Durham version of y_{ij}). With the Geneva algorithm two soft gluons will only get combined together if the angle between them is *much* smaller than the angle between the energetic partons. It turns out, that the features of the G-algorithm do not allow the exponentiation of the leading logarithms and hence make it very difficult to calculate the jet production rates at low values of y_{cut} and is therefore not used in the subsequent analysis.

As a comparison to the JADE-like algorithms, the LUCLUS algorithm,[56] introduced by the Lund group, uses a distance measure

$$d_{ij} = \frac{2p_i^2 p_j^2(1-\cos\theta_{ij})}{(p_i+p_j)^2}. \tag{4.6}$$

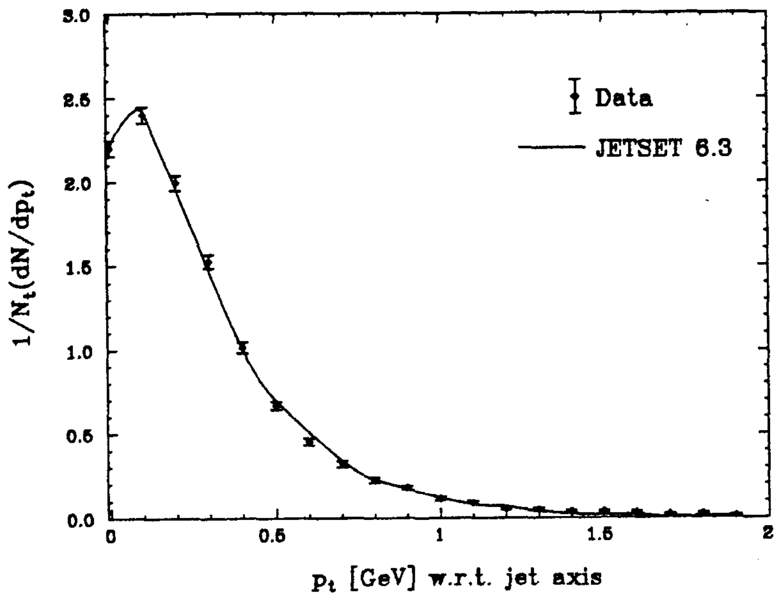

Figure 4.5 The transverse momentum of tracks w.r.t. the jet axis at $y_{cut} = 0.02$. The data are compared with M.C. and are found to be in good agreement.

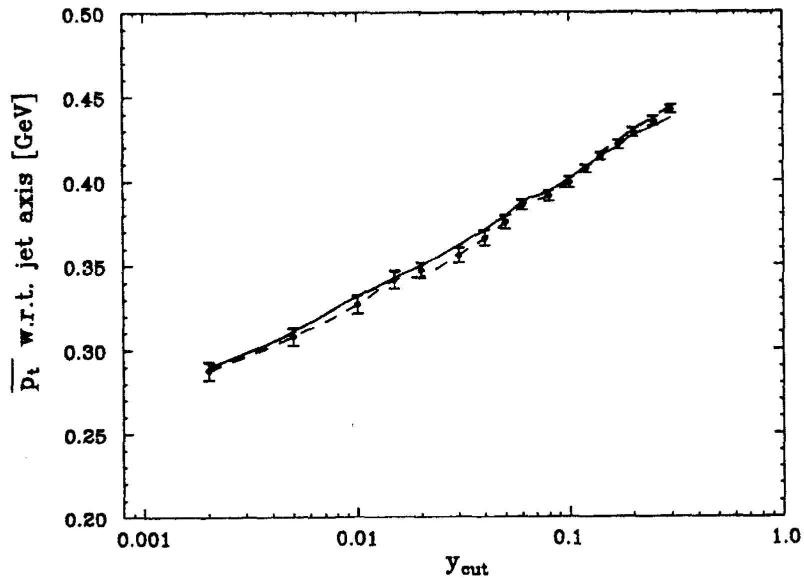

Figure 4.6 The average transverse momentum as a function of y_{cut}. The solid line are the average p_t obtained from JETSET 6.3, the dashed line from HERWIG 5.3.

Algorithm	Resolution	Combination	Remarks
JADE	$\frac{2E_iE_j(1-\cos\theta_{ij})}{E_{vis}^2}$	$p_k = p_i + p_j$	conserves $\sum E, \sum \vec{p}$
E	$\frac{(p_i+p_j)^2}{E_{vis}^2}$	$p_k = p_i + p_j$	Lorentz invariant
E0		$E_k = E_i + E_j$ $\vec{p}_k = \frac{E_k}{\lvert\vec{p}_i+\vec{p}_j\rvert}(\vec{p}_i + \vec{p}_j)$	conserves $\sum E$, but violates $\sum \vec{p}$
P		$\vec{p}_k = \vec{p}_i + \vec{p}_j$ $E_k = \lvert\vec{p}_k\rvert$	conserves $\sum \vec{p}$, but violates $\sum E$
D	$\frac{2min(E_i^2,E_j^2)(1-\cos\theta_{ij})}{E_{vis}^2}$	$p_k = p_i + p_j$	conserves $\sum E, \sum \vec{p}$ avoids exp. problem
G	$\frac{8E_iE_j(1-\cos\theta_{ij})}{9(E_i+E_j)^2}$	$p_k = p_i + p_j$	conserves $\sum E, \sum \vec{p}$ avoids exp. problem
LUCLUS	$\frac{2\lvert\vec{p}_i\rvert\cdot\lvert\vec{p}_j\rvert\cdot\sin(\theta_{ij}/2)}{\lvert\vec{p}_i\rvert+\lvert\vec{p}_j\rvert}$	$p_k = p_i + p_j$	conserves $\sum E, \sum \vec{p}$ incalculable in pert. th.

Table 4.3 Definition of the resolution measures y_{ij} (d_{join} for LUCLUS) and of combination schemes for various jet algorithms; E_{vis} the total energy in the event.[54]

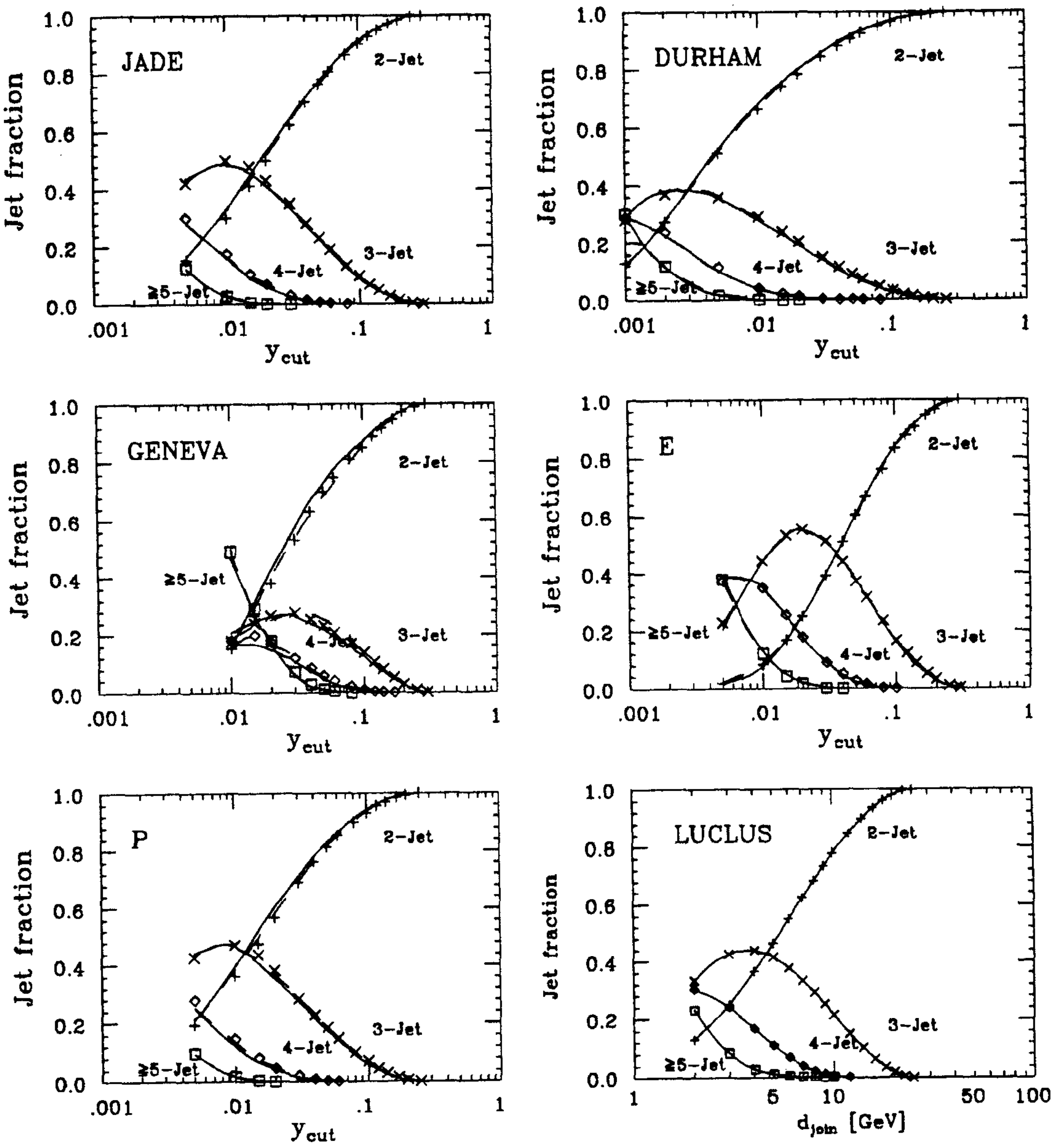

Figure 4.7 Jet rates as a function of the resolution parameter y_{cut} for different jet finding algorithms for the SLD data and two Monte Carlo simulations JETSET 6.3 (solid lines) and HERWIG 5.3 (dashed lines). It is important that the simulated jet rates describe the data well. The number of jets found as a function of y_{cut} depends on the definitions of the resolution variable y_{ij} in the various jet algorithms.

The idea is to define a jet as a collection of particles with a limited transverse momentum with respect to the jet direction. LUCLUS clusters hadrons starting with the fastest particles of the event, and reassigns all particles to the closest jet axis after each combination step. The jet rates in this scheme are not calculable in a perturbative QCD, due to the particular recombination scheme used, and is therefore less suited for QCD studies.

A summary of the algorithms described is given in Table 4.3.[54] The jet rates obtained from the data with all jet finding algorithms described above are shown in Figure 4.7. Also shown in Figure 4.7 are two M.C. simulations (JETSET 6.3 and HERWIG 5.3) of the jet rates. There is a good agreement between the distributions. It is apparent that the different jet-finding schemes have quite different behaviours as a function of y_{cut}, due to the various definitions of their resolution variables y_{ij}. For instance, the y_{cut} value for which the 3-jet rate reaches its maximum varies from 0.003 for the D-algorithm to 0.03 for the G-algorithm. The E- and G-schemes yield larger 4-jet and 5-jet rates compared to the other schemes while the smallest multijet rates are obtained from the D-scheme, which can be extended down to smaller values of y_{cut}.

In order to be able to effectively compare different jet finding algorithms with each other we therefore have to define an effective y_{cut} scale. This can be done for instance by requiring that the maxima of the 3-jet rates, R_3, appear at the same effective y_{cut}, called y_{eff} and that R_3 vanish at the phase space limit of $y_{eff} = 1/3$. Taken the JADE algorithm as the standard, its y_{eff} scale is equal to the y_{cut} scale. y_{cut} vs. y_{eff} for all jet schemes is shown in Figure 4.8. The y_{eff} for the G- and E-scheme are smaller than y_{cut} since their 3-jet maxima lie at a higher y_{cut} value than for the JADE algorithm and the y_{eff} for the p- and D-scheme are larger than y_{cut}.

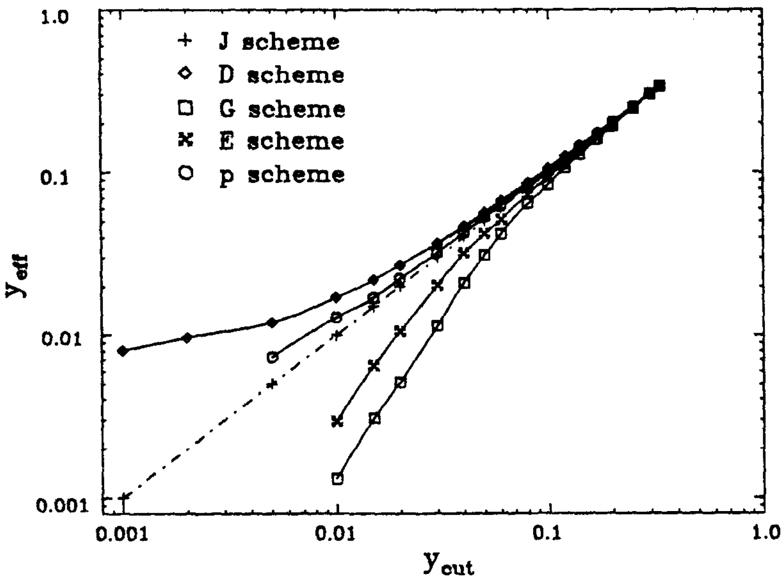

Figure 4.8 y_{cut}vs. the effective y_{eff}. The y_{eff} is chosen so that the maxima of the 3-jet rate R_3 coincide for all jet algorithms and vanish at the limit of $y_{eff} = {}^1/_3$

Another way of comparing the jet-finding algorithms is to measure the ratio of the number of jets found in M.C. events at the parton level and after detector simulation, shown in Figure 4.9a and b as a function of y_{cut} and as a function of y_{eff}. Both the original JADE and the D-scheme reproduce the number of parton jets very well, for all y_{cut}. The E-scheme overestimates the number of parton jets by 10-20%, while the G-algorithm finds 10% too few.

The average angle between jet axes found from partons and the corresponding jet found after the detector simulation is plotted in Figure 4.10a and b as a function of y_{cut} and as a function of y_{eff}, respectively. When plotted against y_{cut}, the D-algorithm reproduces the jet direction best over the whole range of y_{cut} while the E-scheme shows the largest deviation of the found jets from the original parton direction. All algorithms, except for the E-scheme, reproduce the angle equally well when plotted against the effective scale y_{eff}.

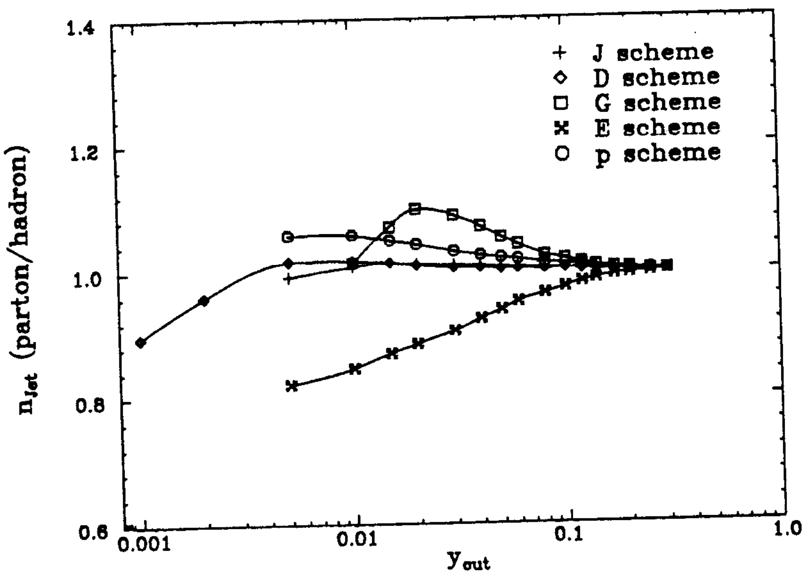

Figure 4.9a The ration of Number of parton jets / Number of hadron jets in Monte Carlo events as a function of y_{cut}.

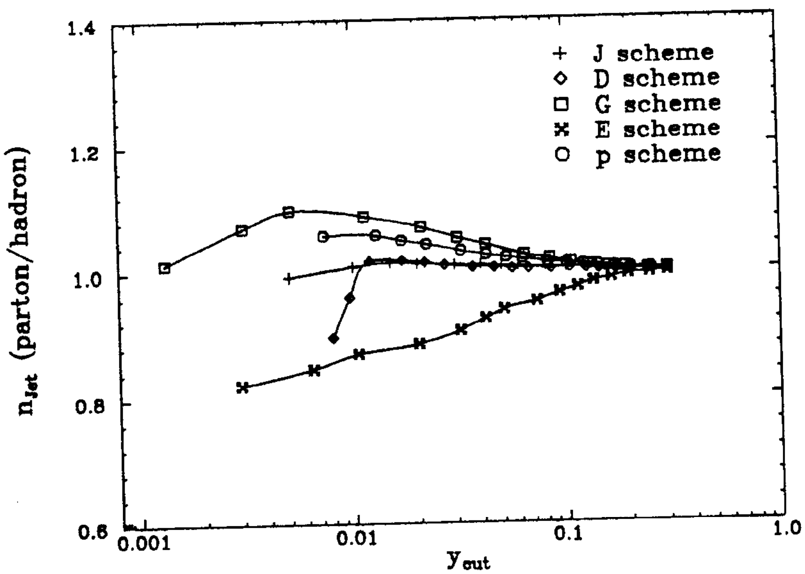

Figure 4.9b The ration of Number of parton jets / Number of hadron jets in Monte Carlo events as a function of the effective y_{eff}.

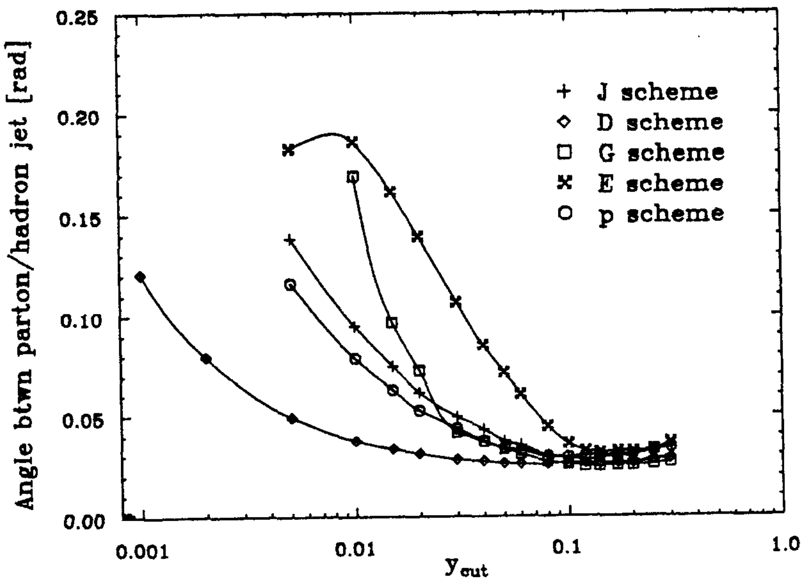

Figure 4.10a The angle between parton jets and hadron jet in Monte Carlo events as a function of y_{cut}.

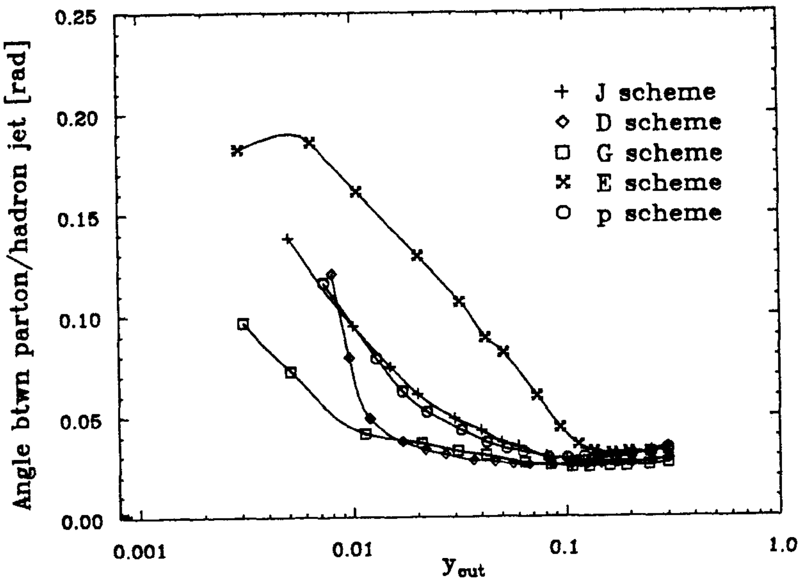

Figure 4.10b The angle between parton jets and hadron jet in Monte Carlo events as a function of the effective y_{eff}.

All these effects will be corrected for when the data are unfolded for hadronization and detector acceptance, described in a following section. It is apparent, though, that the D- and J-schemes are least affected by the limited detector acceptance and resolution, while the E-scheme is rather sensitive to detector effects and hadronization.

To compare the measured jet rates with perturbative QCD calculations one has to use the regular y_{cut} scale, since the calculations are done with y_{cut} for every jet scheme. The following analysis is done with the JADE, D, E and p jet-finding schemes and the results are compared with each other.

4.4 Jet Production Rates and Differential 2-Jet Rates

Within the context of the algorithms just described it only makes sense to talk about a number of jets in an event as a function of the cutoff value y_{cut}. In Figure 4.7 the 2–, 3–, 4– and 5–jet rates, R_n, are shown for the data taken with *SLD*. Also shown are the jet rates calculated from JETSET and HERWIG Monte Carlos with a full detector simulation. It is evident that the data and the simulation are in excellent agreement.

In the *integral* presentation of the R_n distributions as shown in Fig. 4.7 the data points at any value of y_{cut} are strongly correlated with those at other y_{cut} values, as the whole dataset is used in calculating the R_n at each y_{cut} value. In contrast, the statistical errors in bins of the *differential* presentation, $D_2(y_{cut})$, are independent of each other since each event enters the distribution only once. The D_2 distribution is defined as the change in the number of 2–jet events in the distribution R_2 as the value of y_{cut} is changed:

$$D_2(y_{cut}) = \frac{R_2(y_{cut}) - R_2(y_{cut} - \Delta y)}{\Delta y}. \tag{4.7}$$

Each event enters this distribution only once. Essentially, the D_2 distribution

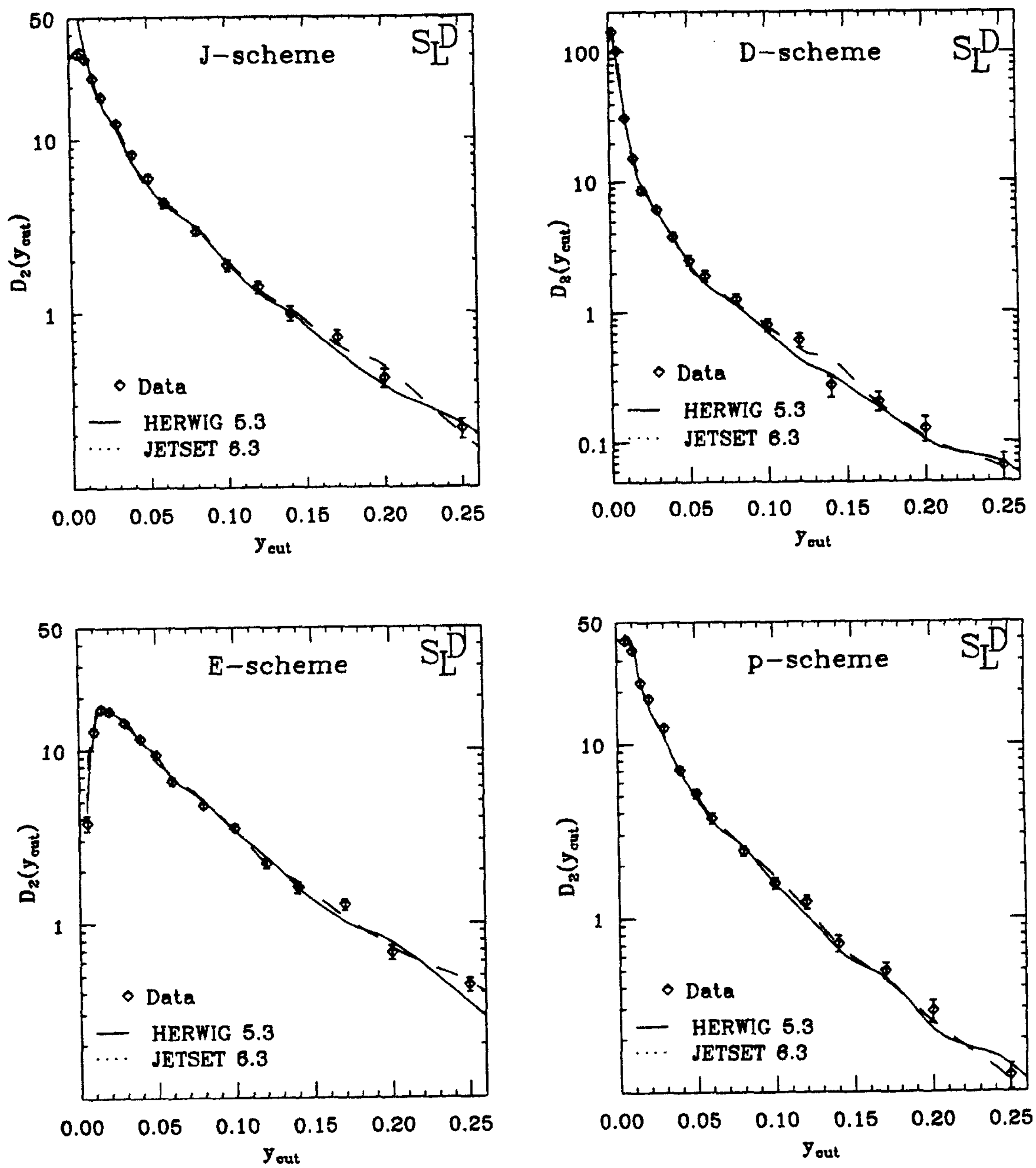

Figure 4.11 Differential 2-Jet rates D_2 as a function of the resolution parameter y_{cut} for the JADE, D, E and p jet finding algorithms. Also shown are the D_2 obtained from JETSET (solid) and HERWIG (dashed) M.C. the statistical errors on the M.C. curves are 2-3 times smaller than the error bars on the data points.

shows the y_{cut} bin at which an event changes from being a 3-jet event to a 2-jet event. $D_2(y_{cut})$ is shown in figure 4.11 for data and Monte Carlo, obtained with the J, D, E and p-schemes.

4.5 Correction for Hadronization and Detector Effects

To study the effects of hadronization on the jet rates in the JETSET Monte Carlo, the jet rates from partons were compared with the jet rates from stable hadrons (charged and neutral) in 100,000 M.C. events without any detector simulation, for the jet finding algorithms described above. The results are shown in Figure 4.12. Both the JADE and Durham algorithms show a very small effect introduced by the hadronization process, while the E-scheme shows rather sizable corrections to the jet rates. The p-scheme shows a moderate but significant correction.

To unfold the measured distributions for the effects of hadronization as well as finite detector resolution and acceptance, the commonly used bin-by-bin correction method was employed. To determine these constants, a distribution is generated in the form of a histogram for two Monte Carlo samples, (I) with no detector simulation and a sample (II) using the same Monte Carlo but including detector simulation and initial-state radiation. The events of sample (II) are subjected to the same reconstruction routines and event selection criteria as are the real data. The Monte Carlo sample (I) treats all particles with lifetime greater than $3 \cdot 10^{-10}s$ as stable particles and includes all stable charged and neutral particles including neutrinos. Let N_G^{MC} be the number of events generated for sample (I) and G_i^{MC} be the number of entries in bin i of a distribution of generated events. Let N_D^{MC} and D_i^{MC} be the number of events which survive after the same event reconstruction and selection that the data was subjected to, for sample (II) and number of entries in the ith bin

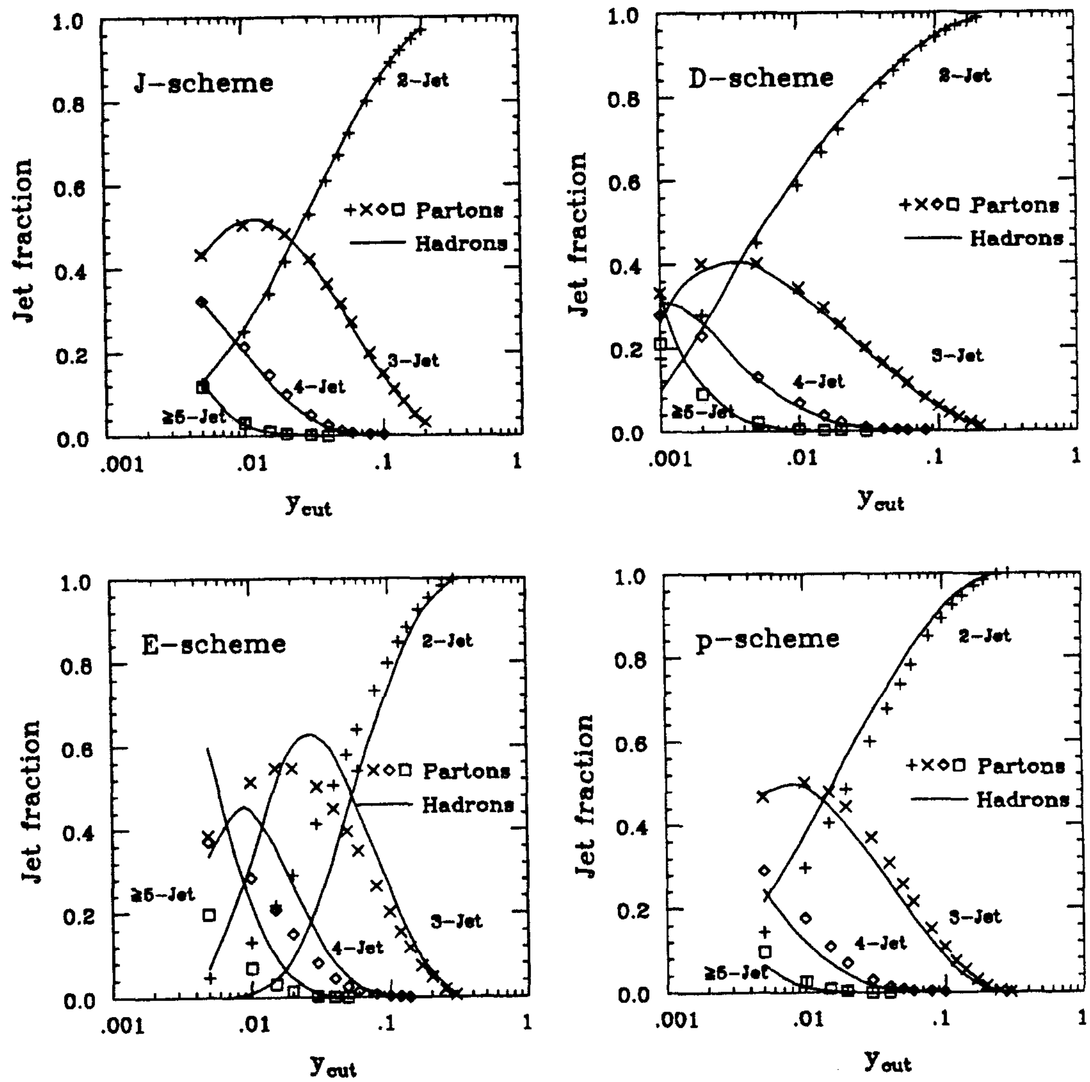

Figure 4.12 Jet rates as a function of the resolution parameter y_{cut} as predicted by the JETSET QCD shower model before (partons) and after (hadrons) the hadronization process. The agreement for the J and D algorithm is remarkably good, while for the E and p algorithm the difference is sizeable. The data are being corrected for hadronization effects.

respectively. The correction factor C_i for bin i in this histogram is then

$$C_i = \frac{\left(G_i^{MC}/N_G^{MC}\right)}{\left(D_i^{MC}/N_D^{MC}\right)}. \tag{4.8}$$

This correction factor is multiplied with the number of entries D_i in the experimentally measured distribution, to give the unfolded value U_i:

$$U_i = C_i \cdot D_i \tag{4.9}$$

For this technique to be applicable it is imperative that the Monte Carlo with detector simulation and intial-state radiation provide a good description of the distributions at the detector level, which was shown in Fig. 4.7.

Due to the finite resolution of any detector an element which appears in the ith bin on the generator level of Monte Carlo histogram may appear in a different bin j in the histogram after the detector simulation. The bin-by-bin procedure is valid if this bin-to-bin migration is symmetric and therefore the correction factors C_i are near unity. This is accomplished by choosing appropriate bin widths of the size of the experimental resolution. To study the bin-to-bin migration and thus the resolution one can look at the y_{cut} values for which an event changes from having 3 jets to having 2 jets, $y_{cut}(3 \to 2)$. Figure 4.13 shows a scatter plot of $y_{cut}(3 \to 2)$ for Monte Carlo events before vs. after the detector simulation was applied. With a perfect detector all events would lie on a diagonal line in this figure. The spread around the diagonal is caused by the finite experimental resolution and acceptance. The resolution at any value of $y_{cut}(3 \to 2)$ can be determined by plotting the vertical distance to the diagonal of every point in the scatter plot and fitting a Gaussian curve to it as shown in Figure 4.14. The standard deviation of these distributions as a

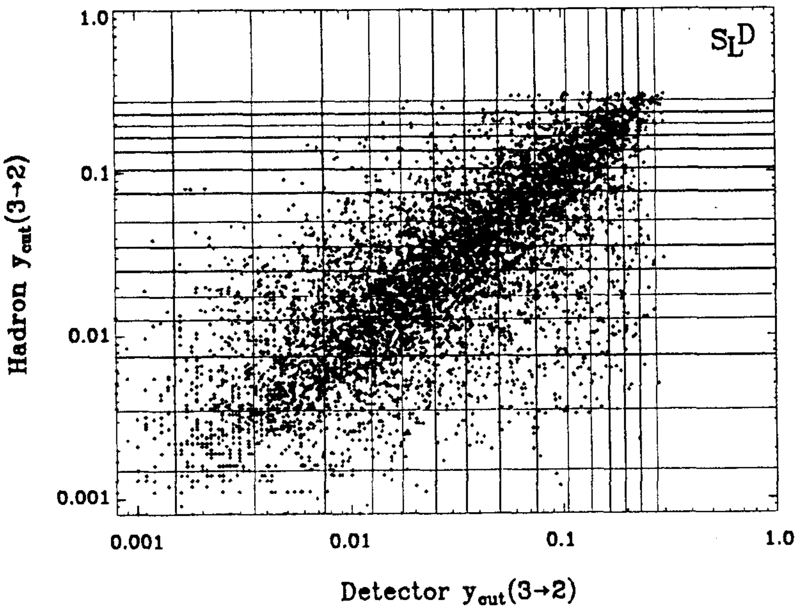

Figure 4.13 y_{cut} value for which an event changes from 3 jets to 2 jets, $y_{cut}(3 \rightarrow 2)$ of Monte Carlo events before vs. after detector simulation.

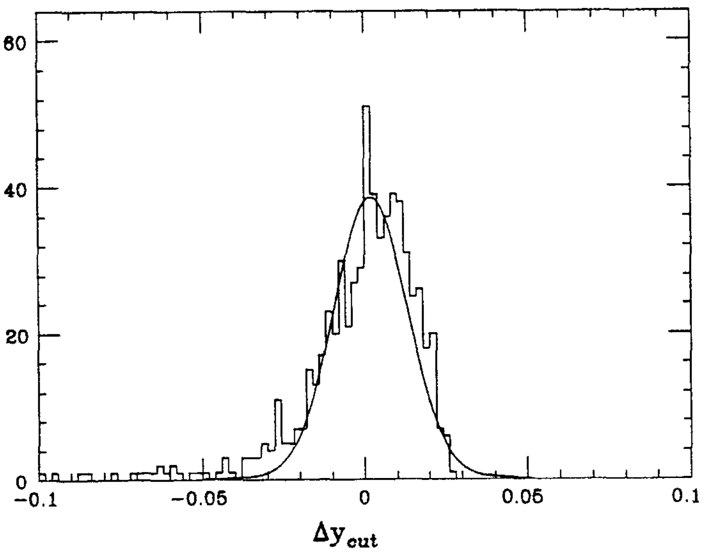

Figure 4.14 The resolution function at y_{cut}=0.03 with a Gaussian curve fit to it. The histogram contains the distances of all $\{y_{cut}^{had.}(3 \rightarrow 2), y_{cut}^{det.}(3 \rightarrow 2)\}$ points to the diagonal $y_{cut}^{had.} = y_{cut}^{det.}$. The width of the fitted Gaussian function is defined to be the *resolution*.

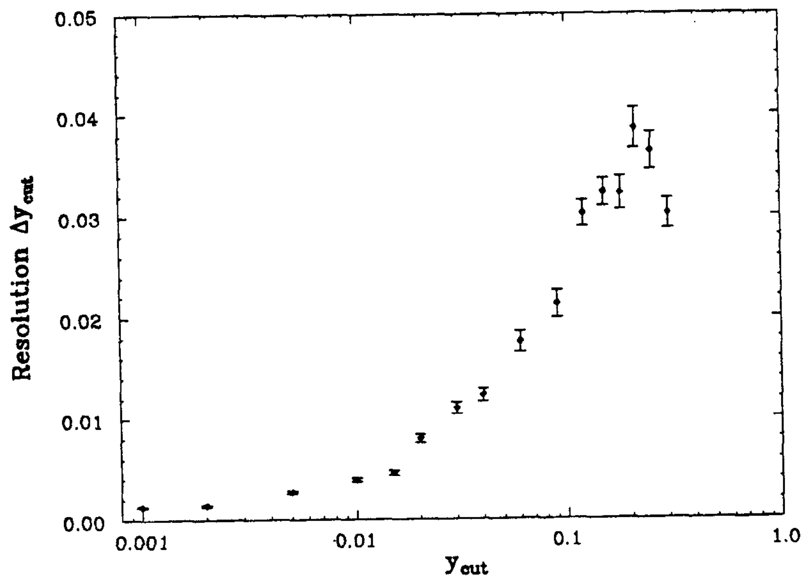

Figure 4.15 The resolution as a function of y_{cut}. The bin widths of the D_2 distribution were chosen to be roughly equal to the Resolution at the given value of y_{cut}.

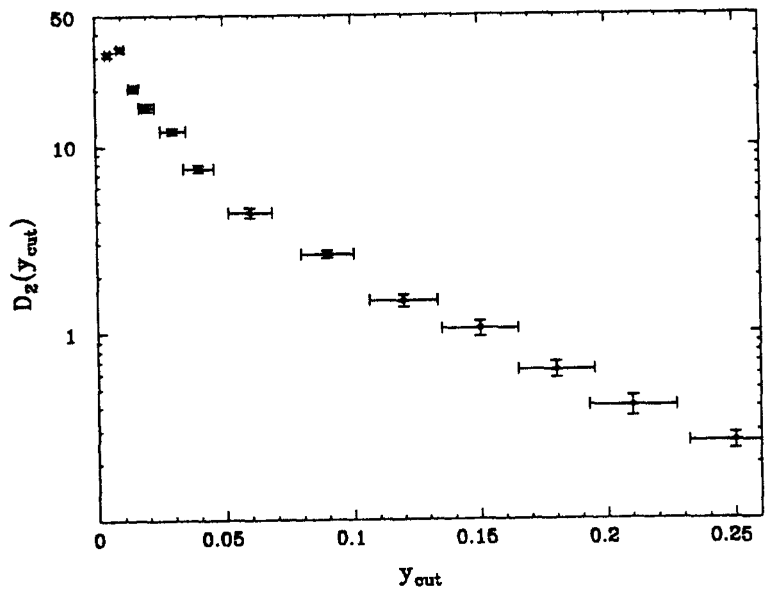

Figure 4.16 D_2 distribution with the chosen bin widths. The horizontal error bars indicate the resolution at each y_{cut} value.

function of y_{cut} is shown in Figure 4.15. The bin widths of the D_2 distribution (Fig. 4.11) to which the results of the QCD calculations are being fitted in this analysis were chosen to be about the same as the experimental resolution at the center of the bin. Figure 4.16 shows the D_2 distribution with the horizontal error bars indicating the resolution at the center of each bin.

4.6 The Corrected Data

To correct the data for this analysis, correction factors C_i determined from JETSET 6.3 were used. The correction factors for the 2–jet, 3–jet and 4–jet rates used for the JADE jet scheme are shown in Figure 4.17. The values of C_i which were obtained for the 2–jet rate, R_2, are very close to unity. For high values of y_{cut} the correction factors for the R_3 and R_4 are substantially larger than 1, but never larger than 2, which indicates that after detector simulation we tend to find fewer jets, due the loss of tracks down the beam pipe or into non-active detector regions as a result of the finite acceptance of the detector. Figure 4.18 shows the influence of the correction for hadronization as well as initial state radiation and detector simulation on the reconstruction of n-jet rates with the p-algorithm, simulated in model calculations, as a function of the jet resolution parameter y_{cut}.

Initial-state photon radiation, whose effects are also removed in the correcting process, contributes only about 2% or less to the values of the bin–by–bin correction constants. To first order, variations in the center-of-mass energy has little influence on the number of jets. The unfolded jet rates obtained with the J, D, E and p-scheme are tabulated in Tables 4.4-4.7. In Table 4.8 the differential 2-jet rates are listed for the 4 different algorithms calculated from the unfolded R_2 distributions.

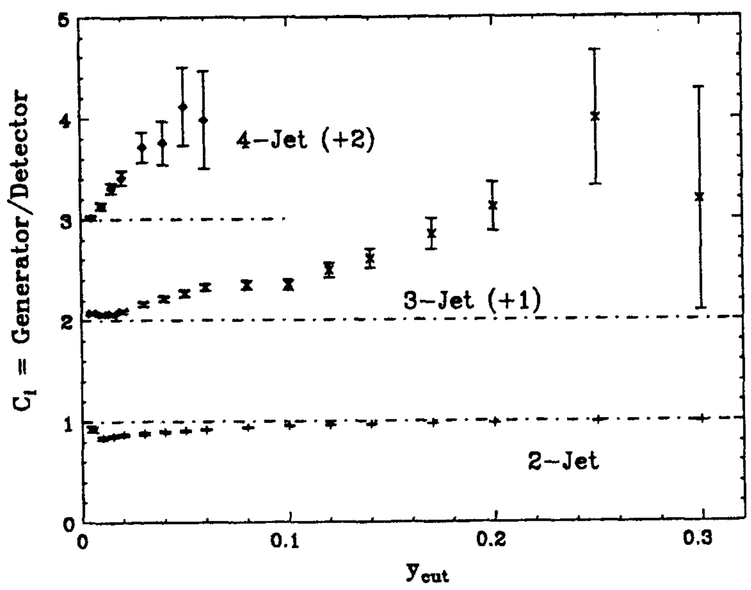

Figure 4.17 The bin-by-bin correction factors for detector effects for 2-, 3- and 4-jet rates evaluated with the JADE algorithm. For display purposes one and two units are added to the 3- and 4-jet coefficients respectively.

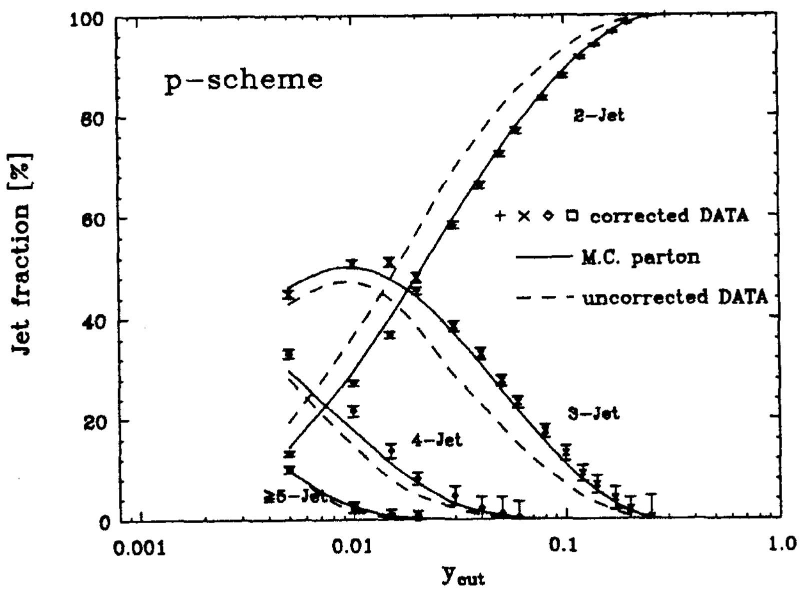

Figure 4.18 The influence of hadronization as well as initial state radiation and detector simulation on the reconstruction of n-jet rates with the p algorithm, simulated in model calculations, as a function of the jet resolution parameter y_{cut}.

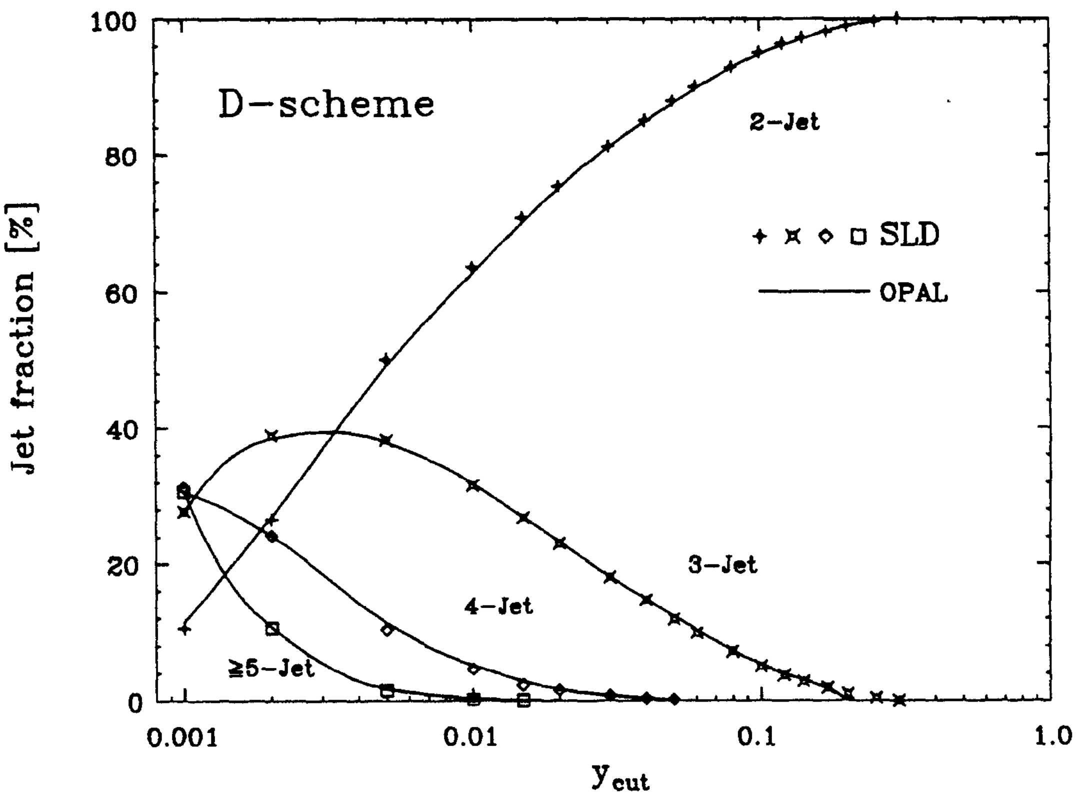

Figure 4.19 After correcting the data for detector effects, the jet rates can be compared with the results from other experiments. The data points with error bars are the jet rates R_n, corrected for hadronization and detector acceptance, compared with the corrected jet rates from the OPAL experiment at LEP which are shown as solid lines.

JADE recombination scheme				
y_{cut}	R_2	R_3	R_4	$R_{>5}$
0.005	13.46 ± 0.62	44.62 ± 0.70	31.64 ± 0.68	10.21 ± 0.41
0.010	24.77 ± 0.62	51.89 ± 0.72	20.95 ± 0.73	3.02 ± 0.61
0.015	33.88 ± 0.65	51.72 ± 0.74	14.63 ± 0.83	0.83 ± 0.67
0.020	41.75 ± 0.67	48.94 ± 0.75	10.16 ± 0.88	0.14 ± 0.44
0.030	53.50 ± 0.68	42.54 ± 0.77	4.56 ± 0.90	0.09 ± 1.22
0.040	61.75 ± 0.66	36.49 ± 0.78	2.38 ± 0.95	–
0.050	68.07 ± 0.63	31.21 ± 0.79	1.17 ± 1.06	–
0.060	72.84 ± 0.60	27.09 ± 0.81	0.66 ± 1.23	–
0.080	79.94 ± 0.53	20.53 ± 0.87	0.26 ± 2.45	–
0.100	84.72 ± 0.47	16.12 ± 0.94	0.02 ± 2.51	–
0.120	88.55 ± 0.41	12.13 ± 0.98	–	–
0.140	91.49 ± 0.35	9.06 ± 1.10	–	–
0.170	94.92 ± 0.28	5.30 ± 1.10	–	–
0.200	96.76 ± 0.21	3.41 ± 1.12	–	–
0.250	98.80 ± 0.12	1.45 ± 1.14	–	–
0.300	99.80 ± 0.05	0.13 ± 1.20	–	–

D recombination scheme				
y_{cut}	R_2	R_3	R_4	$R_{>5}$
0.001	21.02 ± 0.92	34.75 ± 0.74	26.99 ± 0.61	17.53 ± 0.44
0.002	30.06 ± 0.67	39.11 ± 0.68	22.45 ± 0.60	8.03 ± 0.41
0.005	46.13 ± 0.65	39.28 ± 0.70	13.15 ± 0.69	1.73 ± 0.54
0.010	59.28 ± 0.64	35.13 ± 0.75	5.73 ± 0.78	0.30 ± 0.77
0.015	67.03 ± 0.61	29.76 ± 0.76	3.72 ± 1.02	0.02 ± 0.52
0.020	71.88 ± 0.59	26.40 ± 0.78	2.43 ± 1.21	$.005 \pm 2.15$
0.030	78.71 ± 0.53	21.02 ± 0.83	0.90 ± 1.28	–
0.040	82.76 ± 0.48	17.52 ± 0.90	0.47 ± 1.79	–
0.050	85.85 ± 0.44	14.68 ± 0.95	0.20 ± 1.75	–
0.060	88.26 ± 0.40	12.20 ± 1.00	0.11 ± 2.28	–
0.080	91.73 ± 0.34	8.71 ± 1.08	0.02 ± 2.54	–
0.100	94.03 ± 0.28	6.37 ± 1.19		–
0.120	95.89 ± 0.23	4.15 ± 1.19	–	–
0.140	96.86 ± 0.19	3.35 ± 1.39	–	–
0.170	98.00 ± 0.15	2.14 ± 1.59	–	–
0.200	98.84 ± 0.11	1.19 ± 1.62	–	–
0.250	99.57 ± 0.05	0.65 ± 1.77	–	–

Table 4.4, 4.5 Experimental n-jet event production rates, R_n in % of the total hadronic cross section, analyzed in the JADE and the Durham (D) recombination scheme respectively. The data have been corrected for the final acceptance and resolution of the detector and for initial state photon radiation.

	E recombination scheme			
y_{cut}	R_2	R_3	R_4	$R_{>5}$
0.005	5.50 ± 1.76	4.24 ± 1.09	35.74 ± 0.63	19.34 ± 0.43
0.010	13.63 ± 0.92	5.16 ± 0.75	28.44 ± 0.57	6.79 ± 0.34
0.015	21.49 ± 0.73	5.50 ± 0.71	20.94 ± 0.54	2.65 ± 0.33
0.020	28.53 ± 0.68	5.48 ± 0.69	15.46 ± 0.54	1.16 ± 0.34
0.030	40.36 ± 0.68	5.11 ± 0.69	8.31 ± 0.53	0.19 ± 0.32
0.040	50.02 ± 0.68	4.49 ± 0.69	5.09 ± 0.59	0.01 ± 0.13
0.050	57.71 ± 0.67	3.93 ± 0.69	2.98 ± 0.66	–
0.060	63.65 ± 0.66	3.47 ± 0.69	1.64 ± 0.65	–
0.080	72.17 ± 0.61	2.76 ± 0.72	0.38 ± 0.72	–
0.100	79.11 ± 0.55	2.08 ± 0.73	0.13 ± 0.81	–
0.120	83.66 ± 0.49	1.66 ± 0.79	–	–
0.140	87.24 ± 0.44	1.31 ± 0.85	–	–
0.170	92.09 ± 0.35	8.02 ± 0.86	–	–
0.200	94.77 ± 0.28	5.47 ± 0.99	–	–
0.250	98.04 ± 0.17	1.98 ± 1.08	–	–
0.300	99.64 ± 0.06	0.26 ± 0.88	–	–

	p recombination scheme			
y_{cut}	R_2	R_3	R_4	$R_{>5}$
0.005	13.24 ± 0.51	44.81 ± 0.78	33.01 ± 0.91	9.98 ± 0.76
0.010	27.24 ± 0.59	50.73 ± 0.81	21.61 ± 1.16	2.43 ± 1.00
0.015	36.83 ± 0.62	51.14 ± 0.89	13.71 ± 1.35	0.75 ± 1.21
0.020	45.41 ± 0.65	48.00 ± 0.95	8.13 ± 1.31	0.71 ± 1.36
0.030	58.28 ± 0.65	38.45 ± 0.98	4.70 ± 1.89	–
0.040	66.13 ± 0.62	32.93 ± 1.05	2.23 ± 2.26	–
0.050	72.27 ± 0.58	27.64 ± 1.11	1.19 ± 3.17	–
0.060	76.98 ± 0.55	23.38 ± 1.17	0.46 ± 3.04	–
0.080	83.43 ± 0.47	17.52 ± 1.32	–	–
0.100	87.90 ± 0.41	13.15 ± 1.48	–	–
0.120	91.54 ± 0.34	9.14 ± 1.59	–	–
0.140	93.90 ± 0.28	6.84 ± 1.80	–	–
0.170	96.53 ± 0.21	4.10 ± 2.20	–	–
0.200	98.32 ± 0.14	1.90 ± 2.22	–	–
0.250	99.64 ± 0.05	0.39 ± 4.23	–	–
0.300	99.98 ± 0.01	0.00 ± 0.00	–	–

Table 4.6, 4.7 Experimental n-jet event production rates, R_n in % of the total hadronic cross section, analyzed in the E-scheme and the p-scheme respectively. The data are corrected for the final acceptance and resolution of the detector and for initial state photon radiation.

		D-scheme	J-scheme	E-scheme	p-scheme
y_{cut}	Δy_{cut}	D_2	D_2	D_2	D_2
0.002	0.001	99.19 ± 21.02	–	–	–
0.005	0.003	118.84 ± 5.45	16.14 ± 4.27	6.67 ± 0.99	15.89 ± 4.74
0.010	0.005	26.27 ± 2.95	22.34 ± 4.85	16.89 ± 2.82	28.06 ± 5.91
0.015	0.005	15.59 ± 1.74	18.53 ± 3.90	16.05 ± 3.18	19.15 ± 3.97
0.020	0.005	9.593 ± 0.89	16.07 ± 3.21	14.18 ± 2.94	17.65 ± 3.43
0.030	0.010	6.909 ± 0.54	11.95 ± 1.64	11.85 ± 1.76	13.44 ± 1.75
0.040	0.010	4.064 ± 0.39	8.55 ± 1.14	9.57 ± 1.43	7.90 ± 1.02
0.050	0.010	3.145 ± 0.31	6.48 ± 0.85	7.64 ± 1.15	6.29 ± 0.78
0.060	0.010	2.500 ± 0.16	4.80 ± 0.63	5.94 ± 0.85	4.83 ± 0.59
0.080	0.020	1.808 ± 0.12	3.47 ± 0.31	4.27 ± 0.43	3.21 ± 0.28
0.100	0.020	1.199 ± 0.12	2.38 ± 0.21	3.48 ± 0.34	2.27 ± 0.20
0.120	0.020	1.071 ± 0.71	1.96 ± 0.17	2.26 ± 0.22	1.98 ± 0.18
0.140	0.020	0.448 ± 0.73	1.46 ± 0.14	1.78 ± 0.17	1.19 ± 0.13
0.170	0.030	0.402 ± 0.92	1.24 ± 0.10	1.69 ± 0.13	0.93 ± 0.10
0.200	0.030	0.315 ± 0.54	0.64 ± 0.06	0.88 ± 0.08	0.73 ± 0.13
0.250	0.050	0.142 ± 0.21	0.40 ± 0.05	0.69 ± 0.05	0.29 ± 0.08
0.300	0.050	0.118 ± 0.21	0.22 ± 0.06	0.33 ± 0.05	0.07 ± 0.18

Table 4.8 Differential 2-jet rate, $D_2(y_{cut})$. The data are corrected for the final acceptance and resolution of the detector and for initial state photon radiation.

The corrected data can now be compared directly to the results of other experiments which have corrected their data in a similar fashion. In Fig. 4.19 the corrected *SLD* data are shown together with the unfolded results obtained with the OPAL detector at LEP.[59] The jet production rate from both experiments are in good agreement with each other.

4.7 Determination of $\Lambda_{\overline{MS}}$ from Differential 2–jet Rates

The QCD scale parameter $\Lambda_{\overline{MS}}$ can be determined by fits of the analytic $\mathcal{O}(\alpha_s^2)$ QCD calculations to the experimental, differential 2–jet distributions $D_2(y_{cut})$. As described in the introductory chapter, the relative jet production rates R_n are quadratic functions of α_s:

$$\begin{aligned} R_2 &\equiv \sigma_2/\sigma_{tot} = 1 + C_{2,1}\alpha_s + C_{2,2}\alpha_s^2, \\ R_3 &\equiv \sigma_3/\sigma_{tot} = C_{3,1}\alpha_s + C_{3,2}\alpha_s^2, \\ R_4 &\equiv \sigma_4/\sigma_{tot} = C_{4,2}\alpha_s^2. \end{aligned} \tag{4.10}$$

The kth order QCD coefficients for n-jet production, $C_{n,k}$, were calculated for each jet algorithm and tabulated by G. Kramer and B. Lampe[16] and Z. Kunszt and B.R. Nason.[17] Calculations in higher than second order are not yet available. The coefficients depend only on the value of the resolution parameter y_{cut}, but do not exhibit an explicit dependence on the energy. The only energy dependence of the jet production rates is determined by the energy dependence of α_s. The strong coupling α_s can be written as a function of $\log(Q^2/\Lambda^2_{\overline{MS}})$ (eq. 1.8), where $\Lambda_{\overline{MS}}$ is the QCD scale parameter and Q is the QCD renormalization scale. The subscript $\overline{MS}$ (modified minimum subtraction scheme) denotes the renormalization scheme used to calculate the parameter Λ (see Ch. 1.5).

The calculated values of the differential 2–jet rate, $D_2^{th.}(y_{cut}, \Lambda_{\overline{MS}})$ can be fit to the experimentally measured $D_2^{exp.}$ distribution by minimizing χ^2

$$\chi^2 = \sum_{y_{cut}} \left(\frac{D_2^{exp.} - D_2^{th.}}{\delta D_2^{th.}} \right)^2 , \tag{4.11}$$

using the minimization program MINUIT.[58] $\delta D_2^{th.}$ is the statistical error in the expected bin contents. Within each jet recombination scheme, the corresponding $\mathcal{O}(\alpha_s^2)$ QCD calculations are fitted to the data for two different treatments of the renormalization scale Q^2:

1) The QCD parameter $\Lambda_{\overline{MS}}$ is determined for fixed renormalization scale $Q^2 = E_{cm}^2$. The fit is performed in regions of y_{cut} where the experimental 4-jet rate R_4 is less than 1%. This is motivated by the fact that $\mathcal{O}(\alpha_s^2)$ calculations with $Q^2 = E_{cm}^2$ do not describe the observed production rates of 4-jet events[52] and thus, by the overall unitarity condition $R_2 + R_3 + R_4 = 1$, must also fail to describe the 2- and 3-jet production rates in regions where $R_4 \neq 0$. For the different algorithms the fits were performed in the regions of $y_{cut} > 0.04$ in the D-scheme, $y_{cut} > 0.05$ for the p-scheme, $y_{cut} > 0.06$ for the J-scheme and $y_{cut} > 0.08$ in the E-scheme.

2) Both $\Lambda_{\overline{MS}}$ and the renormalization scale factor $f = Q^2/E_{cm}^2$ are treated as free parameters and are determined in a two parameter fit. $\mathcal{O}(\alpha_s^2)$ calculations predict unphysical negative 2-jet production rates, R_2, for small values of $y_{cut} < 0.01$, depending on the actual values of $\Lambda_{\overline{MS}}$ and Q^2. This region of y_{cut} must therefore be excluded from the fit. Also, these calculations do not account for 5-jet rates, therefore the two parameter fits were restricted to regions of y_{cut} for which the experimental 5-jet rate $R_5 < 1\%$, i.e. to data points with $y_{cut} > 0.01$ for the D-scheme, $y_{cut} > 0.02$ for the JADE and p-scheme and $y_{cut} > 0.03$ for the E-scheme. The differences in the fit results from varying the fit regions is part of the systematic error described below.

Figure 4.20 shows the experimentally measured D_2 distributions for the different schemes. Also displayed are the theoretical curves from the best fit results as well as the ranges of y_{cut} for which the fits were performed. The results for $\Lambda_{\overline{MS}}$ and f from all fits are summarized in Table 4.9 as are the χ^2 of the fits.

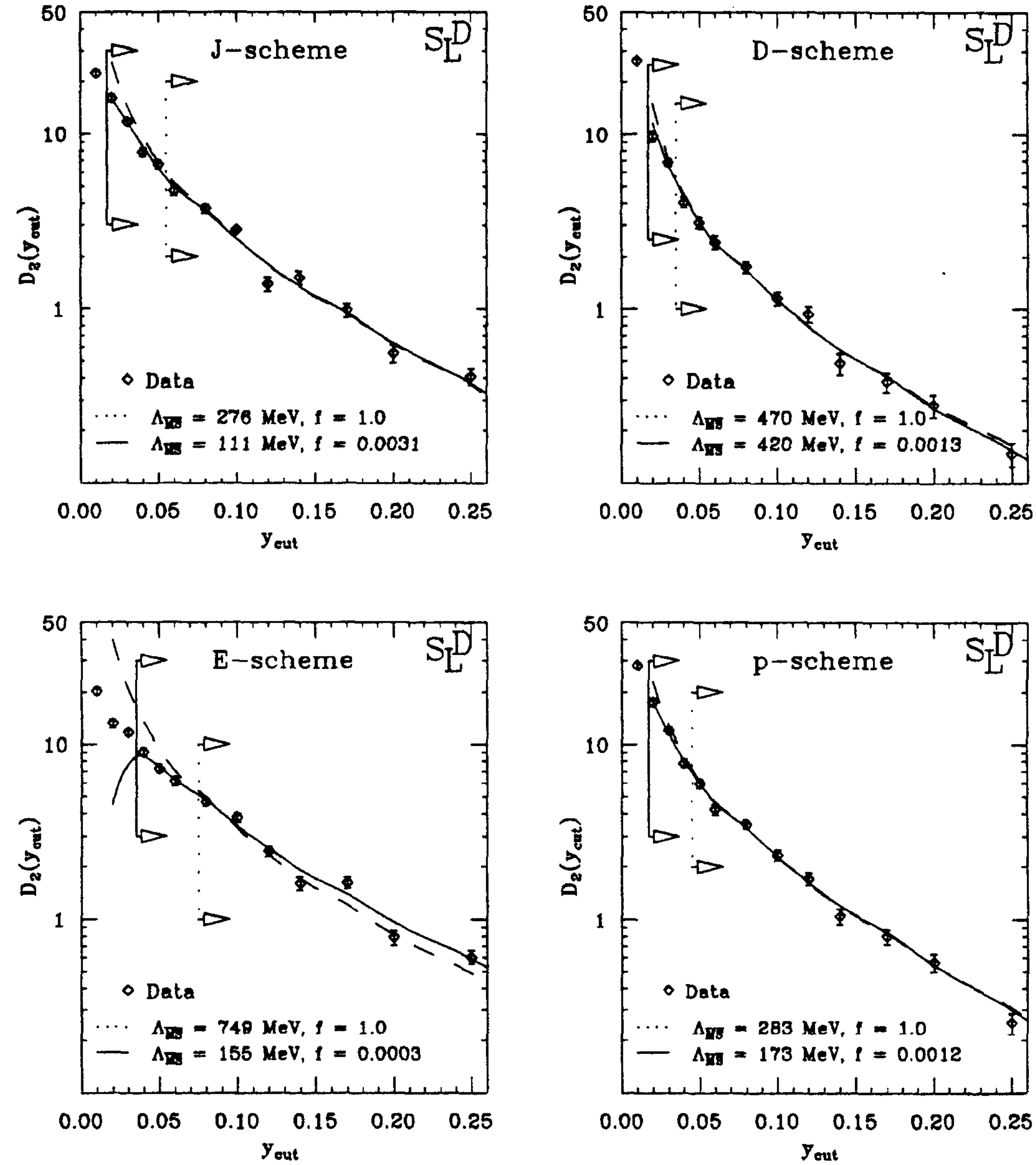

Figure 4.20 Measured distributions of $D_2(y_{cut})$, obtained from the 2-jet production rates, R_2, which were corrected for hadronization, initial state radiation and detector acceptance, compared to the analytic $\mathcal{O}(\alpha_s^2)$ QCD calculations. The QCD parameters are taken from the fit results of $\Lambda_{\overline{MS}}$ with $f = 1$ and of $\Lambda_{\overline{MS}}$ and Q^2 in the regions of y_{cut} indicated by the arrows.

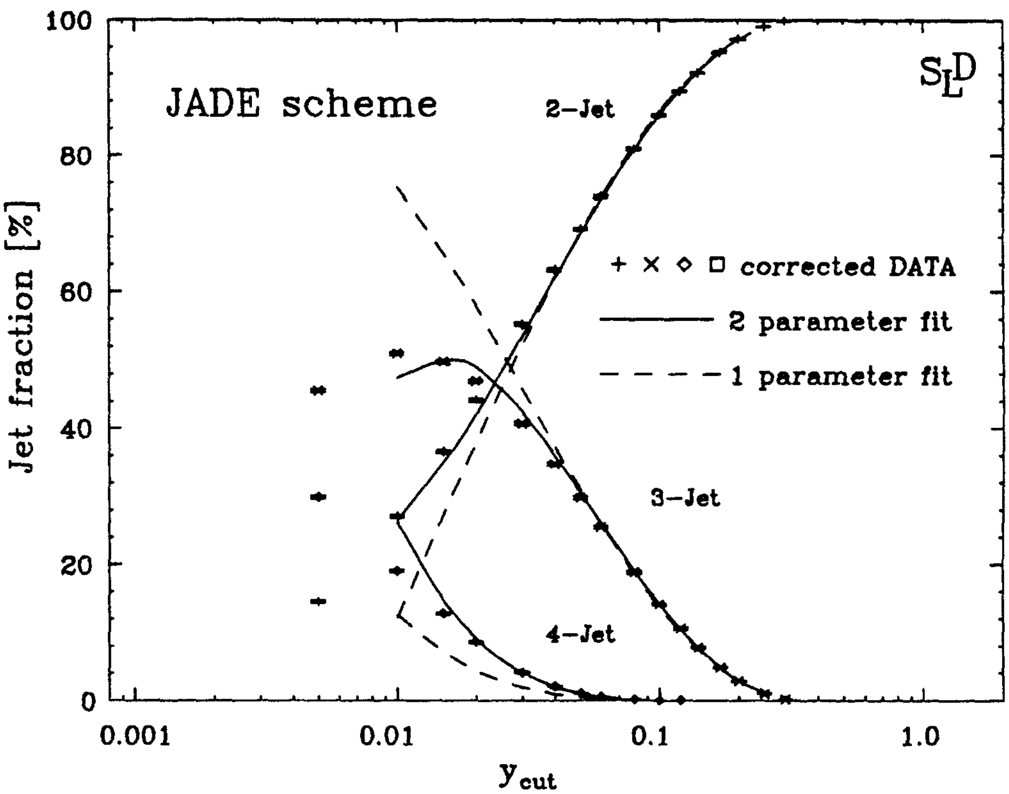

Figure 4.21 The corrected data obtained with the JADE scheme are compared with the jet rates obtained from the 1- and 2-parameter fits. Both fits describe the data well in the region the fit was performed (J-scheme: > 0.06 for the 1-param. fit and > 0.01 for the 2-param. fit). As predicted the 1 param. fit underestimates the 4-jet rate considerably, motivating the restriction of the fits to the region where R_4 is negligible.

	$(f\ =\ 1)$		$(f$ fitted$)$		
scheme	$\Lambda_{\overline{MS}}$ (MeV)	$\chi^2/d.o.f$	$\Lambda_{\overline{MS}}$ (MeV)	$f = Q^2/E^2_{cm}$	$\chi^2/d.o.f$
D	470 ± 41	9/8	420 ± 18	0.0013 ± 0.0002	7/10
J	276^{+33}_{-30}	16/8	111 ± 10	$0.0031^{+0.0004}_{-0.0003}$	9/10
E	749^{+76}_{-83}	14/5	155 ± 19	0.0003 ± 0.00001	11/6
P	283^{+34}_{-37}	6/8	173 ± 25	$0.0012^{+0.0003}_{-0.0004}$	5/10

Table 4.9 Results of fitting $\mathcal{O}(\alpha_s^2)$ QCD calculations to SLD data, for fixed and variable renormalization scales. The errors are statistical only. Note that α_s only depends on the $\log(Q^2/\Lambda^2)$.

The theoretical curves all provide a good description of the data in the regions where the fits were performed; the χ^2 values are always around 1 per degree of freedom for these regions except for the E-scheme which is about 3 per degree of freedom. The calculations with $Q^2 = E^2_{cm}$ or $f = 1$ do not provide a good description of the data below the regions of $y_{cut} > 0.04$ in the D-scheme, $y_{cut} > 0.05$ for the p-scheme, $y_{cut} > 0.06$ for the J-scheme and $y_{cut} > 0.08$ in the E-scheme, where apparently smaller renormalization scales need to be applied to reproduce the data. The resulting "optimized" scale factors f are significantly different for the various jet finding schemes ranging from 0.0001, corresponding to $Q \approx 0.9$ GeV at the Z^0 mass, for the E-scheme to 0.031 ($Q \approx 16$ GeV) for the J-scheme. As a direct consequence, the difference between the fitted values of $\Lambda_{\overline{MS}}$ for $f = 1$ and for f as a free parameter is largest for the E-scheme and smallest for the J-scheme. The results of $\Lambda_{\overline{MS}}$ for $f = 1$ differ greatly between the four jet algorithms, but are closer to each other if f is treated as a free parameter.

In Figure 4.21 the R_n distributions from the JADE-scheme are displayed overlayed by the jet rates calculated with the QCD parameters from the fits to the D_2 distributions. The dashed lines indicate the jet rates from the one parameter fit with $Q^2 = E_{cm}^2$. It is evident that the 4-jet rate is not well reproduced. The solid line is from the two parameter fit with f a free parameter. The agreement over the whole range of y_{cut} is much better. By definition, neither of the fits account for the 5-jet rate.

The values for $\Lambda_{\overline{MS}}$ and Q can be inserted into eq. 1.8 to obtain the corresponding value for the strong coupling α_s. Note that α_s only depends on the $\log(Q^2/\Lambda^2)$. Large variations in $\Lambda_{\overline{MS}}$ have relatively small effects on α_s.

4.8 Statistical Errors

For a large number of events the number of entries in every bin of the n-jet rates as a function of y_{cut} is distributed binomially. The error in such a distribution is given by $\sigma^2 = k(1 - k/n)$, where n is the total number of events and k the number of entries in a particular bin. As opposed to the R_n distributions, the bin contents of the D_2 distribution are completely uncorrelated, so, the statistical error is just one over the square root of the number of entries in that bin.

The minimization routine MINUIT provides the user with an error on the parameter(s) to which the data are being fitted. MINUIT calculates the Hessian error matrix,[58] which is the full matrix of second derivatives of the function with respect to the currently variable parameters, and inverts it. For the 5500 events that passed all the selection cuts the value and statistical error on $\Lambda_{\overline{MS}}$ in the 1 parameter fit to the data obtained with the J-scheme is

$$\Lambda_{\overline{MS}} = 276.7^{+33.2}_{-30.2}\,\mathrm{MeV} \quad \text{and}$$

$$\Lambda_{\overline{MS}} = 111.2^{+10.5}_{-\ 9.8}\,\mathrm{MeV}, \quad f = 0.00313^{+0.00041}_{-0.00033}$$

for the 2 parameter fit.

To translate the error in $\Lambda_{\overline{MS}}$ and f into an error of α_s one has to take the partial derivative of eq. 1.8:

$$\Delta\alpha_s = \sqrt{\left(\frac{\partial\alpha}{\partial\Lambda}\right)^2 \Delta\Lambda^2 + \left(\frac{\partial\alpha}{\partial f}\right)^2 \Delta f^2} \tag{4.12}$$

yielding

$$\alpha_s^{(J)}(Q^2 = M_Z^2) = 0.1217 \pm 0.0022 \quad \text{(1 parameter fit)}$$
$$\alpha_s^{(J)}(Q^2 = 0.0031 M_Z^2) = 0.1767 \pm 0.0044 \quad \text{(2 parameter fit)}$$

The value of α_s at the fitted value for Q^2 from the two parameter fit is then translated to $Q^2 = M_Z^2$ yielding

$$\alpha_s^{(J)}(Q^2 = M_Z^2) = 0.1066 \pm 0.0014$$

The values for $\alpha_s(M_{Z^0})$ from the two fits are averaged and listed in Table 4.11. The fit results along with the corresponding statistical errors for the D-, J-, E- and p-scheme are listed in table 4.9. The difference between the two fit results is treated as part of the theoretical systematic error described below.

4.9 Systematic Errors

Estimating the size of the systematic errors of a measurement introduced by the detector and analyzing methods is complex. The systematic uncertainties can be divided into two categories. One contains the experimental systematic errors which arise from limited acceptance, efficiency and resolution of the detector, and from biases and imperfection in detector simulation and in event reconstruction programs, and due to selection criteria applied to the data for this analysis. The other encompasses the theoretical uncertainties which arise from hadronization and from unknown higher order corrections, in addition to uncertainties in the theoretical calculations themselves.

4.9.1 Experimental Systematic Uncertainty

To calculate the errors of the measurement introduced by the detector uncertainties we have to rely on M.C. simulations. Acceptance effects were estimated by varying the cuts on the polar angles of the tracks and thrust axis, described in Chapter 3. A set of loose cuts ($\cos\vartheta_{track} < 1.0$ and $\cos\vartheta_{track} < 0.8$) and a set of tight cuts ($\cos\vartheta_{track} < 0.71$ and $\cos\vartheta_{track} < 0.6$) were applied to the data set and M.C. events and compared against the standard cuts ($\cos\vartheta_{track} < 0.8$ and $\cos\vartheta_{track} < 0.71$). The relative change in the correction factors, C_i, which are used to correct the 2-jet rates, are plotted in Fig. 4.22 (cut A and cut B) as a function of y_{cut}. The resulting variations in the values of α_s were about the same for all jet algorithms, averaging $\Delta\alpha_s = \pm 0.0013$ for the tight acceptance cuts and ± 0.0015 for the loose acceptance cuts, listed in Table 4.10.

Other cuts were also varied: cut C ($I_z < 100cm$, $p_t > 0.0$GeV and $E_{vis}/E_{cm} > 0.0$) and cut D ($I_z < 7.5cm$, $p_t > 0.2$GeV and $E_{vis}/E_{cm} > 0.25$)

and compared with the standard cuts of the z-component of the track impact parameter, $I_z < 10$cm, and the transverse momentum, $p_t > 0.15$GeV and the visible, charged energy fraction $E_{vis}/E_{cm} > 0.2$. To verify that all cuts had the same efficiencies for the data and M.C. the number of data events that passed the cuts were divided by the number of M.C. events for all sets of cuts and were found to vary less than the statistical error on these numbers.

Another possible systematic uncertainty is introduced by the error in the measurement of the magnetic field in SLD, which has the effect of scaling all track momenta by a constant factor. To estimate the magnitude, all track momenta in the M.C. events were multiplied by a factor of 1.02, which corresponds to a missmeasurement of the B-filed of $\Delta B/B = 2\%$ which is much larger than the actual measured uncertainty in the B-field measurement. The corresponding correction factors C_i are also shown Fig. 4.22. The effects are minute and can safely be neglected.

The systematic errors from momentum resolutions was estimated by smearing all M.C. track momenta by $3\% \times$ a random Gaussian number, effectively doubling the errors on the momentum resolution measured in the CDC and leaving all other cuts unchanged. The relative change in the correction factors, C_i, which are used to correct the data, are plotted in Fig. 4.23. The variation in the resulting values of α_s were found to be smaller than the statistical error. Also, since the momentum resolution of the CDC is worse in the z direction, only the z component of the M.C. track momenta were varied by 3%. The resulting uncertainty of α_s was found to be more than twice the size of the error from smearing all momentum components equally, $\Delta\alpha_s = \pm 0.0005$.

The effects of the track reconstruction inefficiency was simulated by randomly removing 10%, 15% and then 20% of all tracks in every M.C. event.

Source of syst. error	$\Delta\alpha_s$
high acceptance cut	$\pm 0.0013^{+}$
no acceptance cut	$\pm 0.0015^{+}$
high $p_t, E_{vis}/E_{cm}$ cut	$\pm 0.0005^{+}$
no $p_t, E_{vis}/E_{cm}$ cut	$\pm 0.0023^{+}$
error in B-field	± 0.0002
varying p by $\Delta p/p = 3\%$	± 0.0002
varying p_z by $\Delta p_z/p = 3\%$	$\pm 0.0005^{*}$
removing 10% of tracks	± 0.0008
removing 15% of tracks	± 0.0014
removing 20% of tracks	± 0.0021
removing 15% of tracks as function of angle w.r.t. jet axis	$\pm 0.0019^{*}$
Varying fit range	$\pm 0.0015^{*}$
total experimental systematic error	± 0.0031

Table 4.10 Summary of errors contributing to the experimental systematic uncertainty of the α_s measurement. The numbers indicated with a $^{+}$ were averaged and added in quadrature with the numbers indicated with a * to get the final value for the experimental systematic error.

Also, 15% of all tracks were removed randomly as a function of the angle ϑ of the track with respect to the jet axis.

It was found that the systematic errors from uncertainties in the track momentum resolution are negligible. Systematic errors from track reconstruction inefficiencies of less than 15% were found to be smaller than the statistical errors. The tracking reconstruction efficiency was estimated by counting vec-

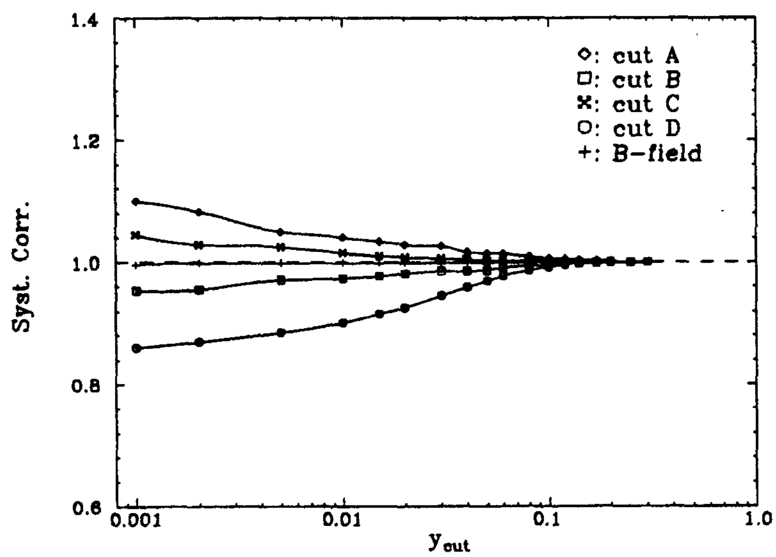

Figure 4.22 The correction factors C_i of the 2-jet rate R_2 for different sets of cuts. **A**: Wide acceptance **B**: Narrow acceptance **C**: Low p_t and energy cut **D**: High p_t and energy cut **E**: High B-field, scaled all momenta by factor 1.02

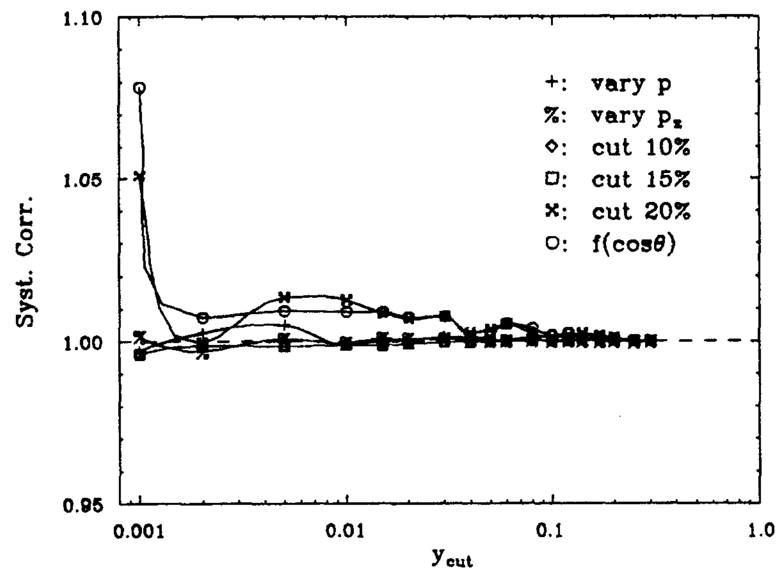

Figure 4.23 The correction factors C_i for various tracking efficiencies. 10-20% of the tracks were randomly removed from M.C. sample. 15% of tracks were randomly removed as a function of the angle with the nearest neighbor track and with the jet axis. (Note the different scale from the previous plot).

tor hits (track segments of hits in a single CDC cell, see Chapter 2.5.7) that were not used in any of the tracks and was found to be smaller than 5%. The effects from varying the acceptance cuts, the transverse momentum cut and the minimum visible energy cut were found to be non-negligible.

Another part of the systematic uncertainty is introduced by the choice of the the regions of y_{cut} in which the fits were performed (see chapter 4.7). They were estimated by varying these fit regions for all jet algorithms. The resulting variation is indicated by the shaded regions around the measured values of α_s in Figure 4.25. The uncertainty is largest for the E-scheme, which has the fewest degrees of freedom in the fit, and smallest for the p-scheme, which produces the best overall fit. The average error from choosing a fit region is $\Delta\alpha_s = \pm 0.0015$, somewhat smaller than the average statistical error of the measurement.

Adding these errors in quadrature, an upper limit to the experimental systematic uncertainties in the measurement of α_s from detector effects was calculated to be $\Delta\alpha_s(exp.syst.) = \pm 0.003$. All sources of systematic detector effects are listed in Table 4.10 along with the corresponding systematic uncertainty in the measured value of α_s.

4.9.2 Theoretical Uncertainty

The hadronization process in the Monte Carlo calculation is a source of uncertainty since we have to depend on models describing the transition from partons to hadrons. There are two ways to estimate this error: (i) use different hadronization models and (ii) and vary parameters in each model.

The difference between the results of α_s obtained with the JETSET M.C. and the HERWIG programs gives a good estimate of this error:

α_s(HERWIG) $-$ α_s(JETSET) $= -0.003$, for the J, D and p jet-finding algorithm and -0.001 for the E-algorithm.

Another estimate of the error introduced by the shower model is obtained by varying the parameter Q_0 in the M.C. program, which determines the lower cutoff of the gluon radiation in the parton shower. From optimizing the M.C. parameters to fit the data, Q_0 was determined to be about 1 GeV. Figure 4.24 shows the difference in α_s from the value of α_s determined at the default value of 1 GeV, as a function of Q_0 for each recombination scheme as Q_0 is varied from 0.5–5.0 GeV. Not all jet schemes are equally sensitive to variations of the Q_0 parameter. The Q_0 uncertainties, $\Delta\alpha_s(Q_0)$, are listed in Table 4.11 for all algorithms, along with a summary of all other experimental and systematic errors in α_s. The systematic error from hadronization models for each jet-finding scheme is taken to be the larger of the two estimates.

Another source of systematic errors are the QCD calculations of the finite order matrix elements contributing to the jet rates. The error in calculating the multi-jet cross section can be estimated by comparing two different methods of calculations by Kunszt and Nason[17](KN) and by Kramer and Lampe[16](KL). Both sets of calculations were fitted to the corrected data. The difference in α_s for the two methods, $\Delta\alpha_s(calc.) = \pm 0.0006$, is much smaller than the statistical error and can safely be neglected.

A much larger source of uncertainty is the choice of the renormalization scale Q. In Figure 4.25 the dependence of α_s on Q is shown. The error bars in this figure indicate the statistical error of the measurements. The shaded area indicates the uncertainty from choosing the fit region. Arrows indicate the fitted values of f and the resulting value for α_s. An upper limit of the scale uncertainty is obtained by taking the difference of the α_s values at $f = 1$ and

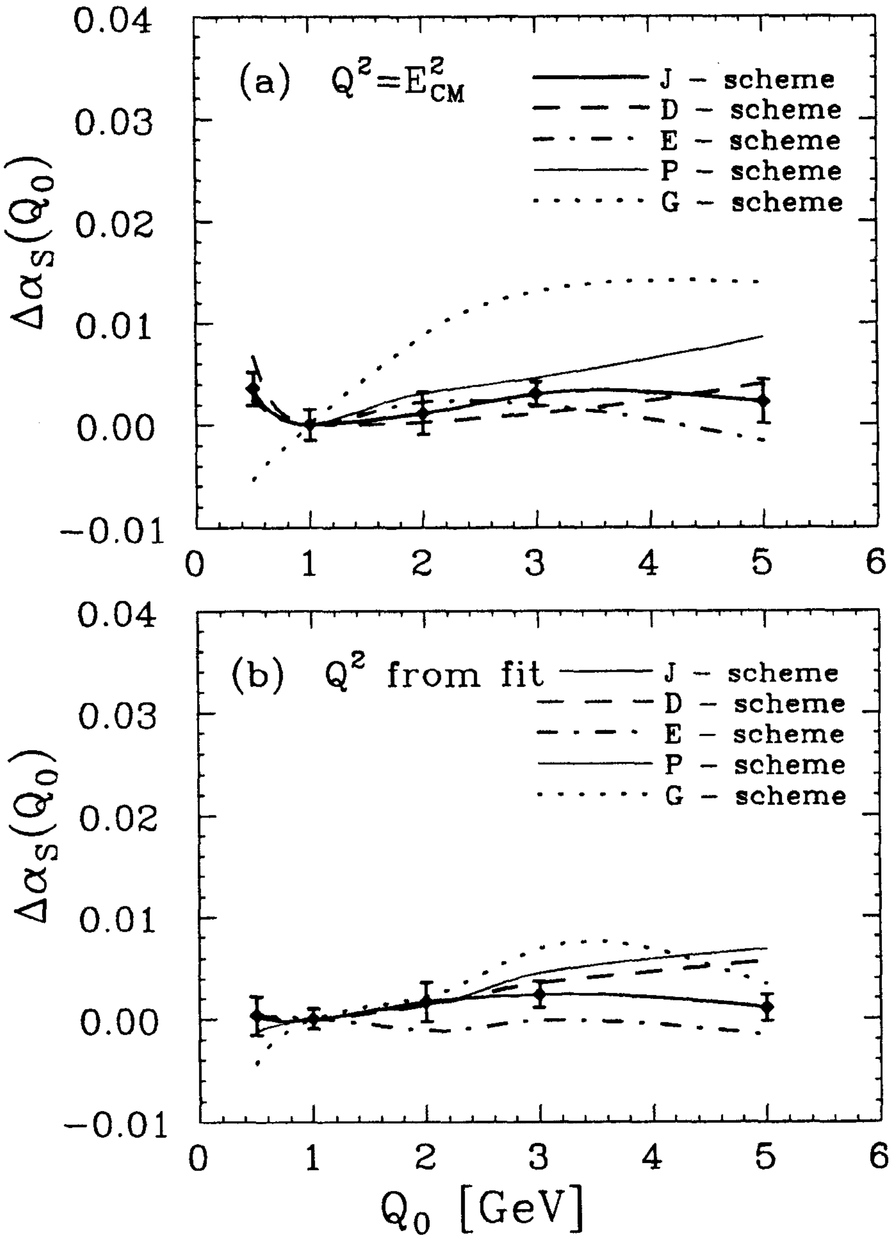

Figure 4.24.a,b Values of α_s from fit results of $\Lambda_{\overline{MS}}$ as a function of Q_0 for $Q = E_{CM}$ **(a)** and for Q as a free parameter **(b)**. The results are displayed for different recombination schemes: J (JADE), D (Durham), E and P schemes. The errors displayed for the JADE results represent the experimental errors of the fits. As a comparison, the Q_0 dependence for the G (Geneva) algorithm is also plotted. It's strong dependence on M.C. parameters make it unsuitable for this analysis.

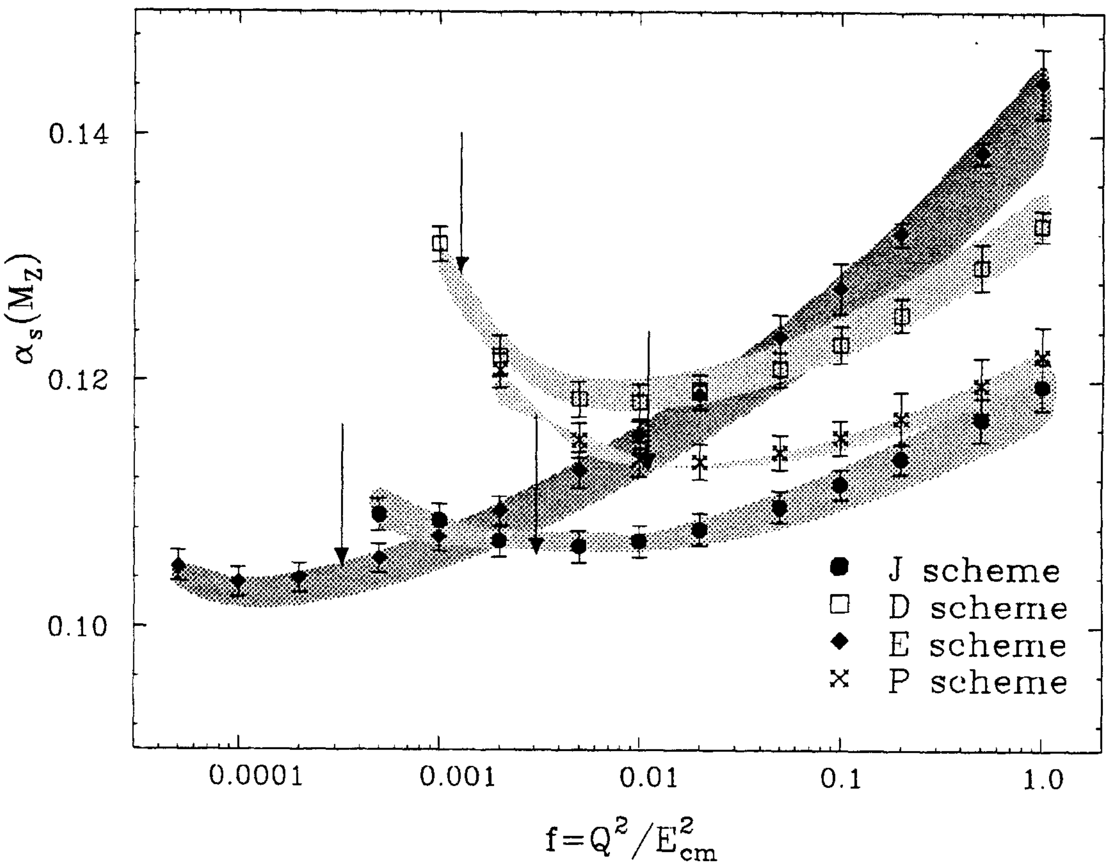

Figure 4.25 α_s as a function of the renormalization scale Q/E_{cm} for the different jet algorithms. The error bars are statistical only. The shaded area indicates the error introduced by varying the fit region. The vertical arrows indicate the value of α_s and f from the 2-parameter fit where f is varied as well.

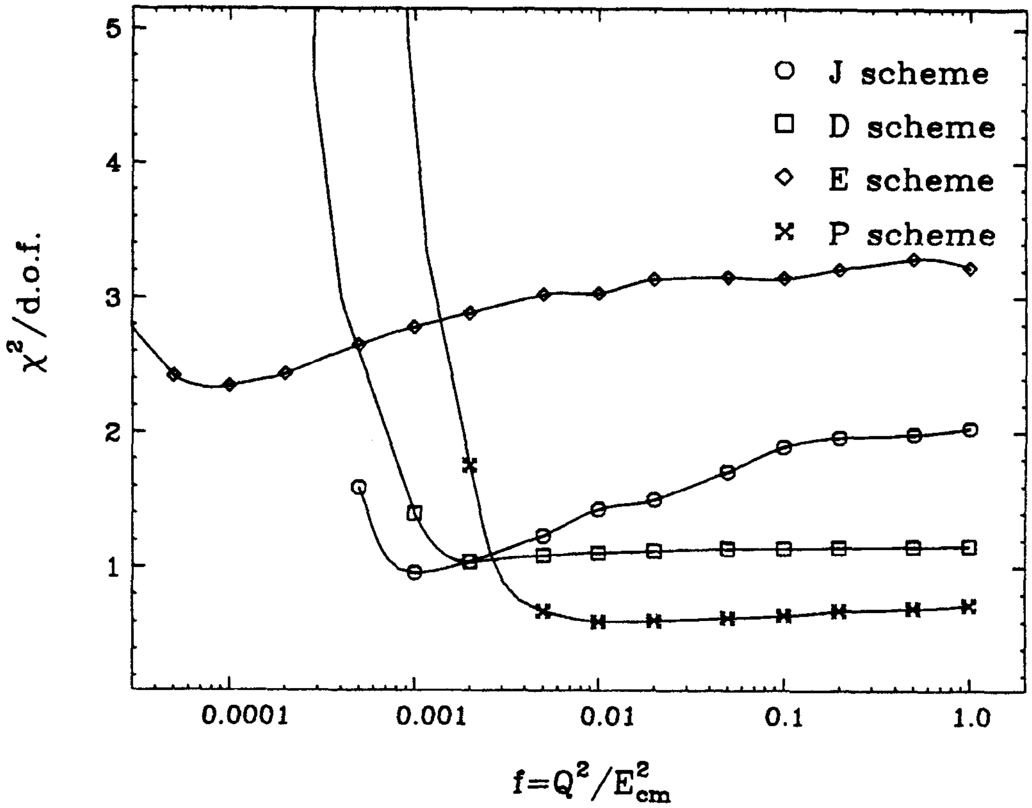

Figure 4.26 $\chi^2/d.o.f.$ of the fit of the analytic $\mathcal{O}(\alpha_s^2)$ calculation to the measured D_2 distribution as a function of the renormalization scale Q/E_{cm}

Scheme	$\alpha_s(M_{Z^0})$	stat. error	systematic errors exp.	HERWIG	Q_0	hadr.	scale
J	0.114	± 0.002	± 0.003	-0.003	$+0.003$	± 0.003	± 0.007
D	0.137	± 0.002	± 0.003	± 0.003	$+0.004$	± 0.004	± 0.007
E	0.126	± 0.002	± 0.003	-0.001	± 0.002	± 0.002	± 0.013
P	0.118	± 0.002	± 0.003	-0.003	$+0.008$	± 0.005	± 0.009

Table 4.11 Summary of errors contributing to the measurement of α_s. The first column in this table contains the average number for α_s from the two fits with $Q = E_{CM}$ and with Q as free parameter. The error in the last column is the scale uncertainty which is half the difference between the two fit results.

at the minimum of the curves. The size of the error depends on the jet-finding algorithm and ranges from $\pm(0.004 - 0.019)$. Figure 4.26 shows the $\chi^2/d.o.f.$ for all the fits as a function of $f = Q^2/E_{cm}^2$. The best fits are obtained for values of f that minimize α_s. No additional error is added from the differences in the results from the four jet-finding algorithms, since this error is contained in the scale uncertainty. A more detailed discussion of the values of α_s as a function of the renormalization scale is given in the following chapter.

All sources of uncertainty considered and the magnitude of their contribution to the total error of the measurement are summarized in Table 4.11. The first column in this table contains the average number for α_s from the two fits with $Q^2 = E_{CM}^2$ and with Q as free parameter and half the difference between the two results is quoted as the scale uncertainty listed in the last column of Table 4.11.

CHAPTER 5

DISCUSSION AND SUMMARY

5.1 Combined Results

In the previous chapter the strong coupling α_s was measured by fitting second order QCD predictions of the differential 2-jet rate, $D_2(y_{cut})$, to the SLD data using four different jet-finding schemes and using different QCD renormalization scales, $f = Q^2/E_{cm}^2$. The results listed in the Tables 4.9 and 4.11 differ quite considerably from each other and Figure 4.25 shows the strong dependence of α_s on the chosen scale. QCD itself does not predict at which value of the scale the second order formulae should be evaluated.

If we average the numbers for α_s obtained from the fits with $f = 1$

scheme	$\alpha_s(M_{Z^0})$
J	$0.121^{+0.006}_{-0.005}$
D	$0.135^{+0.007}_{-0.006}$
E	$0.144^{+0.005}_{-0.005}$
p	$0.123^{+0.010}_{-0.007}$

we get the rather large value of

$$\alpha_s(M_{Z^0}) = 0.131^{+0.007}_{-0.006} \quad \text{(fits with } f = 1\text{)}.$$

There are many indications that $f = 1$ is not necessarily a good choice in a finite order perturbative QCD. Theoretical methods, described earlier in chapter 1.6, which try to reduce the dependence of the physical observables

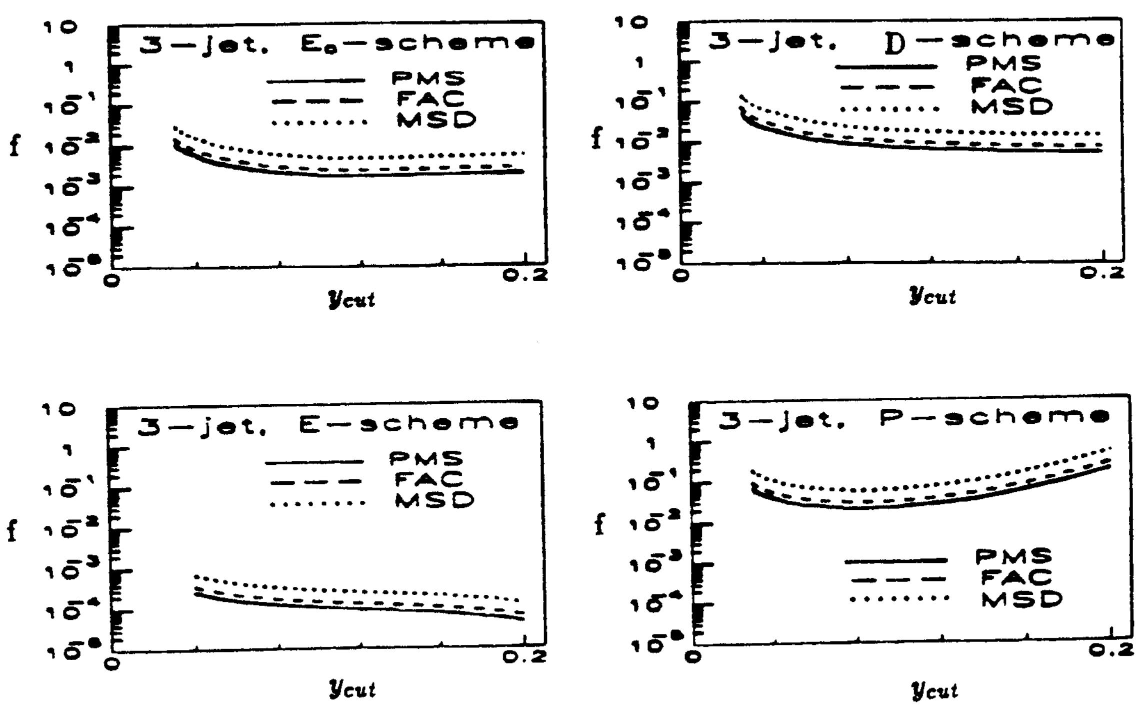

Figure 5.1 Theoretical prediction of the optimized renormalization scale factor $f = Q^2/E_{cm}^2$ for various jet-finding schemes. All methods suggest scales significantly smaller than $f = 1$.

on the scale f suggest that better choices of the scale are $f = 10^{-5} - 10^{-1}$, depending on the physical observable. The differences in the scales may be understood in terms of the difference in the size of the known second order and unknown higher order corrections for different observables. The theoretically suggested scales are plotted in Fig 5.1 for the four jet-finding schemes as a function of y_{cut}.

The theoretical prediction for the optimized scale are in good agreement with the experimental 2-parameter fit results where f is varied, yielding

scheme	$\alpha_s(M_{Z^0})$
J	$0.106^{+0.006}_{-0.005}$
D	$0.130^{+0.007}_{-0.006}$
E	$0.109^{+0.005}_{-0.004}$
p	$0.114^{+0.009}_{-0.006}$

averaging to

$$\alpha_s(M_{Z^0}) = 0.115^{+0.007}_{-0.005} \quad \text{(fits with } f \text{ free).}$$

By choosing regions of f which yield the best χ^2 in the fits (Fig.4.26) the optimized f can be estimated to be 0.0008-0.008 for the JADE-scheme, 0.0025-0.05 for the D-scheme, 0.005-0.1 for the p-scheme, and 0.00005-0.0005 for the E-scheme. In these regions $\alpha_s(M_{Z^0})$ is determined from the fitted values of $\Lambda_{\overline{MS}}$:

scheme	$\alpha_s(M_{Z^0})$
J	$0.107^{+0.006}_{-0.005}$
D	$0.118^{+0.008}_{-0.005}$
E	$0.104^{+0.006}_{-0.005}$
p	$0.113^{+0.009}_{-0.006}$

These four results lie markedly closer together than the results from the fits with $f = 1$ and all the χ^2 of the fits are better. These results average to

$$\alpha_s(M_{Z^0}) = 0.111^{+0.008}_{-0.005} \quad f \text{ (optimized).}$$

This result is in good agreement with the QCD prediction of $\alpha_s(M_{Z^0}) = 0.11 \pm 0.01$ [60] based on the lower energy experimental results and with measurements from processes where the renormalization scale ambiguity is not important, eg.

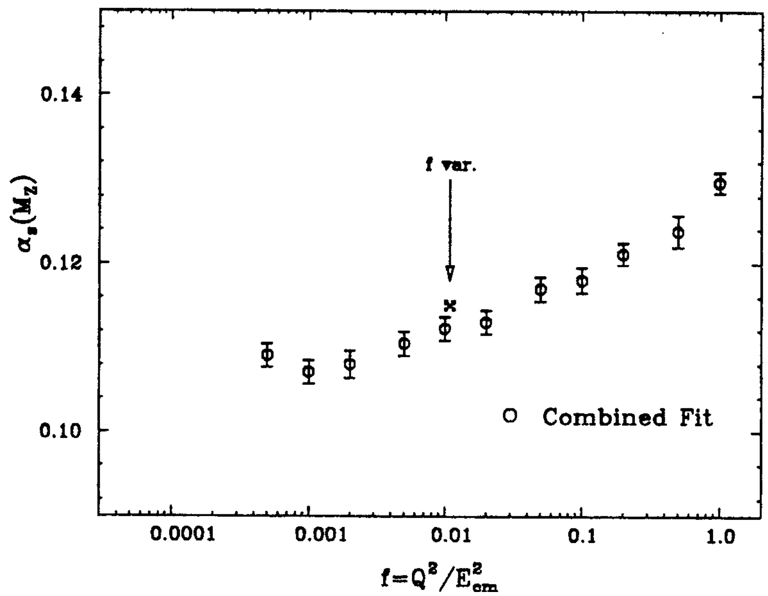

Figure 5.2 α_s as a function of the scale f for a simultaneous fit to the data from all four jet schemes. The arrow indicates the value of f and the resulting α_s for the fit with one single scale f for all schemes. Allowing an individual scale for each scheme yielded $f = 0.00039 - 0.0025$ and $\alpha_s(M_{Z^0}) = 0.116$. The error bars are statistical only.

$\alpha_s(M_{Z^0}) = 0.119^{+0.004}_{-0.005}$ predicted from the analysis of deep inelastic scattering data[62] and $\alpha_s(M_{Z^0}) = 0.105 \pm 0.004$ from the charmonium spectrum.[63]

Simultaneous fits to the $D_2(y_{cut})$ distributions of all four jet-finding schemes as performed with $f = 1$ and with f as a free parameter, allowing for individual scale factors for each jet-finding scheme, yield

$$\alpha_s(M_{Z^0}) = 0.129 \pm 0.006 \quad \text{and}$$
$$\alpha_s(M_{Z^0}) = 0.116^{+0.005}_{-0.004} \quad \text{(simultaneous fit)}$$

respectively. The χ^2 of $3.6/d.o.f$ for the first fit with $f = 1$ is larger than any of the individual fits which confirms that a single value of $\Lambda_{\overline{MS}}$ cannot fit all the data if f is fixed at 1. The combined fit with free scale factors provides a description of the data consistent with the individual fits. A combined fit with only one common scale f yielded the same value for α_s as the fit with separate scales, but with a considerably worse χ^2.

With hindsight there are many signs that indicate that the renormalization scale should be smaller than 1, but there are no rigorous theoretical arguments that predict that α_s should be evaluated at the scale which minimizes the value of α_s and what the value of that scale should be. A more conservative estimate would be to take the weighted average of the results from the fits with $f = 1$ and of the results from the optimized scale using the formula $\bar{\alpha}_s = \sum w_i \alpha_s^i / \sum w_i$, where the weights $w_i = (\frac{x_i + y_i}{2})^{-2}$, and $\binom{+x_i}{-y_i}$ are the experimental and statistical uncertainties. This procedure provides the weighted average of

$$\alpha_s(M_{Z^0}) = 0.120^{+0.008}_{-0.005} \quad \text{(weighted average)}.$$

To this result we have to add a scale uncertainty, derived from the difference of the results at $f = 1$ and at $f =$optimized, yielding

$$\boxed{\alpha_s(M_{Z^0}) = 0.120^{+0.012}_{-0.010} \quad \text{(final result)}.}$$

The error is a composite of the statistical error of ± 0.002, the experimental systematic error of ± 0.003 and the theoretical uncertainty of ${}^{+0.011}_{-0.009}$ added in quadrature. This result is in good agreement with values earlier by the same experiment.[64]

5.2 Running of α_s

The non-Abelian structure of QCD predicts an energy dependence of the strong coupling α_s. According to eq. 4.10, the energy dependence of the jet production rate is only determined by the energy evolution of α_s. Therefore we can test the validity of QCD by comparing the jet production rates measured in similar experiments at various center-of-mass energies. In Figure 5.3 the 3-jet rates, obtained with the JADE algorithm at a $y_{cut} = 0.08$, from JADE,[65] TASSO,[66] AMY,[67] Mark II,[68] OPAL[59] and SLD experiment are plotted against the center-of-mass energy, E_{cm}.

The 3-jet rate measured by JADE and TASSO at the PETRA accelerator at an energy of 22 GeV is larger by of factor of 1.43 ± 0.05 than the 3-jet rate measured at the Z^0 mass and the measurement from Mark II at PEP at an energy of 29 GeV is larger by a factor 1.24 ± 0.02. Measurements at higher energies are a factor 1.18 ± 0.02 and 1.07 ± 0.02 larger at 34.6 GeV and 44 GeV, respectively. This comparison therefore establishes the observation of significant scaling violations. In the framework of QCD, these scaling violations can be attributed to the energy dependence of α_s.

Also shown in Figure 5.3 are the predictions of $\mathcal{O}(\alpha_s^2)$ QCD calculations with the measured values for the QCD parameter $\Lambda_{\overline{MS}}$ and the renormalization scale factor f. The dashed curve was obtained from the fitted value of $\Lambda_{\overline{MS}} = 276 \pm 31$ MeV with the scale $f = 1$. This curve appears to fit the data obtained at lower energies of 20-40 GeV reasonably well. The extrapolated curve from $\Lambda_{\overline{MS}} = 111 \pm 10$ MeV and $f = 0.0031$ significantly overestimates the 3-jet rates at lower energies. This may indicate the need for different optimized scales for measurements at lower center-of-mass energies. Using the results from all measurements shown in Figure 5.3 to make a 1-parameter fit to $\Lambda_{\overline{MS}}$

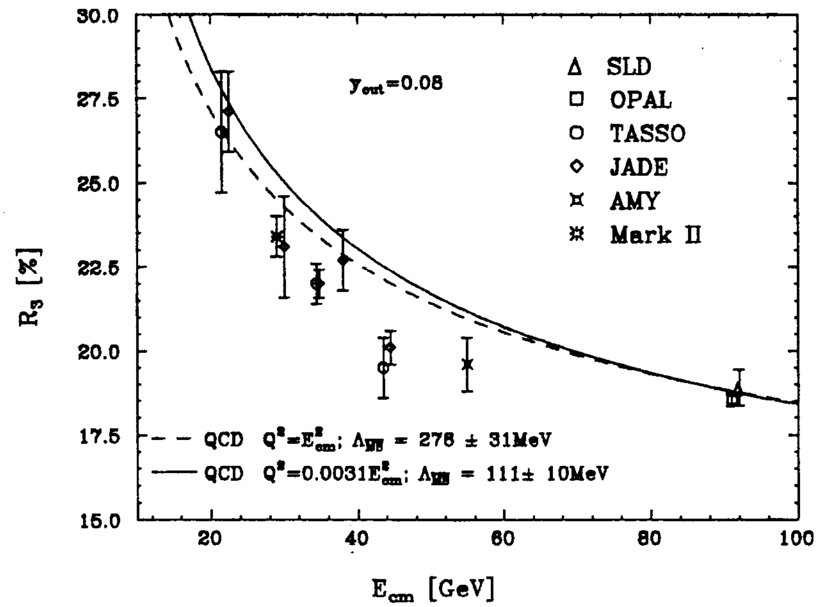

Figure 5.3 The 3-jet rate obtained with the JADE algorithm for y_{cut}=0.08 as a function of the center-of-mass energy. The curves indicate the energy dependence of α_s calculated with the measured values of $\Lambda_{\overline{MS}}$ and f.

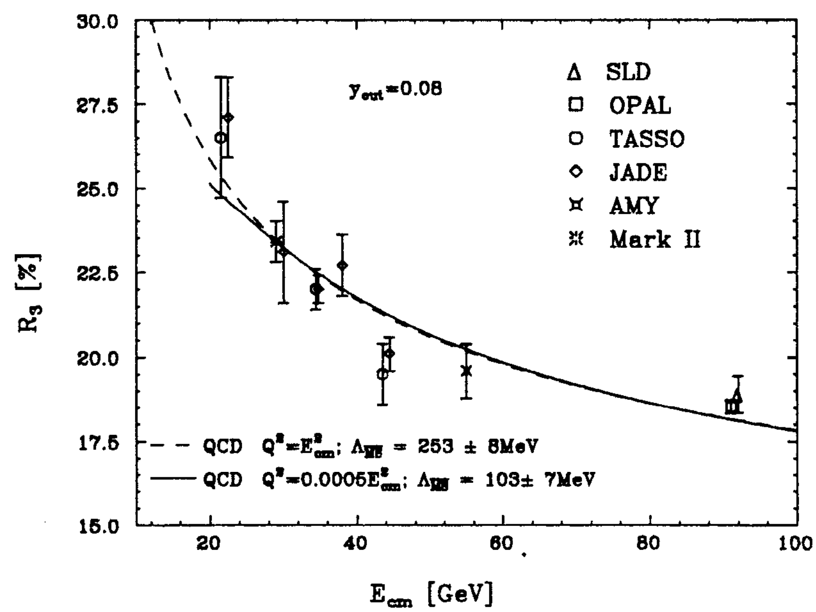

Figure 5.4 The fitted curves of the energy dependence of α_s to the measured 3-jet rate of all indicated experiments yield values for $\Lambda_{\overline{MS}}$ which are well within statistical errors of the values measured with SLD but with a significantly smaller scale f.

at fixed scale f and a 2-parameter fit to $\Lambda_{\overline{MS}}$ and f, shown in Figure 5.4, yield the values

$$\Lambda_{\overline{MS}} = 252 \pm 8\,\mathrm{MeV} \quad \text{and}$$

$$\Lambda_{\overline{MS}} = 103 \pm 7\,\mathrm{MeV}; \quad f = 0.00049 \pm 0.00004$$

which are well within errors of the values for $\Lambda_{\overline{MS}}$ measured with SLD at the Z^0 mass (c.f. Table 4.9) but require a significantly smaller scale f. For both fits the $\chi^2/d.o.f.$ is around 2.

5.3 Jet rates from polarized Z^0 decays

SLC is able to deliver longitudinally polarized electron beams to the interaction point. During the physics run in 1992 electrons with an average polarization of $\mathcal{P} = \pm 22\%$ were produced by shining a circularly polarized laser beam on a GaAs cathode. This is the first time such beams have been available in e^+e^- collisions. It is therefore of interest to measure physical quantities in decays of Z^0s produced with left-handed and right- handed electrons separately and compare the measurements.

All the hadronic Z^0 events recorded with the SLD detector were split up into two data samples according to the handedness of the electron beam with which the Z^0 was produced. The analysis described in the previous chapter was repeated for both data sets. In Figure 5.5 the ratio of $R_3^{(L)}/R_3^{(R)}$ is shown. The jet production rates R_n were not corrected for hadronization and detector acceptance, since these systematic effects cancel out by taking the ratios of the left- and right-handed data samples.

After applying the bin-by-bin correction to both data sets the $\mathcal{O}(\alpha_s^2)$ QCD calculations were fitted to the measured $D_2^{(L)}$ and $D_2^{(R)}$ distributions. The

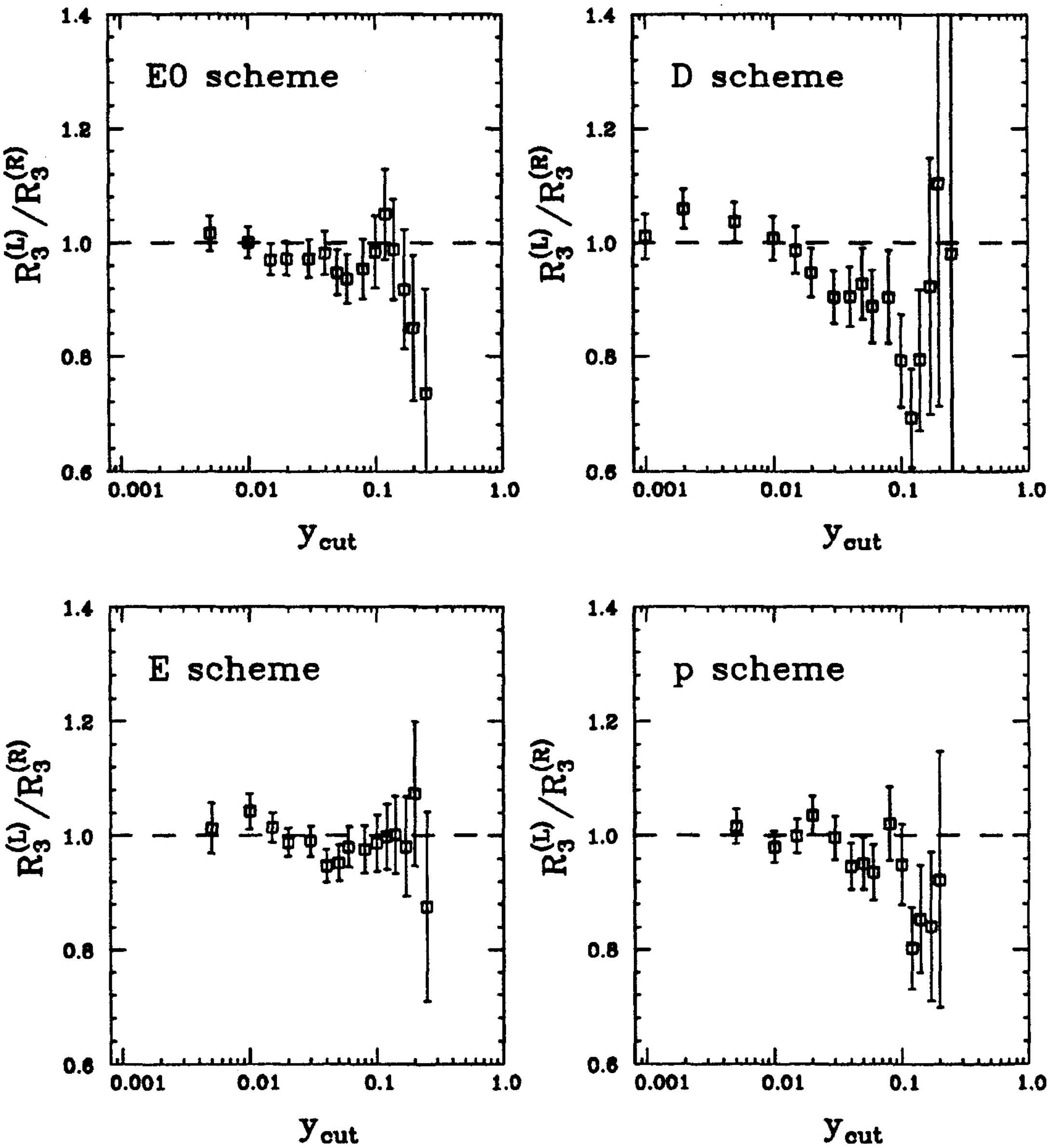

Figure 5.5 The ratio of uncorrected 3-jet rates as a function of y_{cut} obtain from the left-handed and right-handed data sample. For each jet-finding scheme, the data points are strongly correlated with each other, since all the data were used to calculate the jet production rates at every value of y_{cut}.

results for α_s obtained in the same way as described in the previous chapter by taking the average number from all jet finding algorithms and the two different fits were found to be:
for right handed electrons

$$\alpha_s^{(R)}(M_Z) = 0.119^{+0.012}_{-0.010}$$

for left handed electrons

$$\alpha_s^{(L)}(M_Z) = 0.121^{+0.012}_{-0.010}$$

Both numbers agree with each other within statistical errors. This is in agreement with the perturbative QCD calculations, which predict the strong coupling α_s to be the same in both cases, since QCD is vectorlike and parity is conserved.

5.4 Summary

We have presented an analysis of jet rates from a data sample of about 12,000 hadronic Z^0s recorded by the SLD. Only charged tracks measured with the central drift chamber (CDC) were used in this study. We have determined the value of the strong coupling, $\alpha_s(M_{Z^0})$, using four different jet finding algorithms (J,p,E and D). The jet rates were then corrected for effects of hadronization, detector resolution and acceptance. These measurements were compared with analytic calculations in complete second order perturbative QCD. The QCD parameter $\Lambda_{\overline{MS}}$, and thus $\alpha_s(M_{Z^0})$, was then determined in fits of the QCD calculations to the corrected data distributions. The weighted average of the four results is thus

$$\alpha_s(M_{Z^0}) = 0.120 \pm 0.002(stat.) \pm 0.003(\mathrm{exp.})^{+0.011}_{-0.009}(\mathrm{theor.})$$

Experimental uncertainties due to the modelling of the detector response lead to relative uncertainties of 3% in $\alpha_s(M_{Z^0})$. The statistical errors are less than 2% in all cases. The theoretical error quoted above is the sum of $\Delta\alpha_s(had.)$, $\Delta\alpha_s(Q_0)$ and $\Delta\alpha_s(scale)$ added in quadrature. We find that the largest error in this measurement is the theoretical error from varying the renormalization scale f. Calculations to $\mathcal{O}(\alpha_s^3)$ will be needed to significantly reduce the uncertainty introduced by this scale ambiguity.

Our result is in good agreement with results from the LEP experiments. Also, we find that this result is in excellent agreement with the prediction of the energy dependece of the strong coupling α_s when compared with the measurements at lower energies.

REFERENCES

1. M.Akrawy *et al.* Measurement of the Z mass, Phys. Lett. B **231** (1989) 530.
2. M. Gell-Mann, Y. Ne'eman, The Eightfold Way, New York (1972).
3. T. Cheng and L.Li, Gauge theory of elementary paricle physics, 1985
4. T. Sjöstrand, QCD and Jets at LEP, CERN-TH.5902/90 (1990).
5. F. Halzen and A. Martin, Quarks & Leptons , 1984
6. J. Ellis, Gaillard, Ross, Nucl.Phys. **B111** (1976) 253.
7. A. Ali *et al.*, Nucl. Phys. **B167** (1980) 229.
8. K.J.F. Gaemers, J.A.M. Vermaseren, Z.Physik **C7** (1980) 81.
9. R.K. Ellis, Nucl. Phys. **B178** 421 (1981)
10. D. Danckaert, Phys. Lett. **114B** (1982) 203.
11. Particle Data Group, J.J. Hernández *et al.*, Phys. Lett. **B239** III.51 (1990)
12. K. Hagiwara, Nucl. Phys. **B220** (1989) 560.
13. F.A. Berends, Nucl. Phys. **B231** (1989) 39.
14. P. Nättig, DESY Preprint, DESY 88-125, August 1988.
15. G. Hanson *et al.*, Phys. Rev. Lett. **35** (1975) 1609
16. G. Kramer, B. Lampe, Fortschritte der Pysik, **37** (1989), 161
17. Z. Kunszt, B.R. Nason, Physics at LEP I, (1989), 374
18. G. Kramer, N. Magnussen, Z. Phys C, **49**, (1991), 301
19. G. Kramer, Private communications
20. W.A. Bardeen *et al.*, Phys. Rev. **D18**, 3998 (1978).
21. G. t'Hooft, Nucl. Phys. **B86** (1973) 455.
22. W.A. Bardeen, *et al.,* Phys. Ref **D18** (1978) 3998.
23. OPAL Collaboration, P.D. Acton et al., CERN-PPE/91-214 (1991)
24. S. Brodsky, Phys. Rev. **D28** (1983) 228.
25. P.M. Stevenson, Phys. Rev. **D23** (1981) 2916.
26. S. Sanghera, Proceedings of the 7th DPF meeting, Batavia, Nov. 1992.

27. G. Grunberg, Phys. Lett. **95B** (1980) 70.
28. P.D. Acton *et al.* A Global Determination of α_s at LEP, CERN-PPE/92-18 (1992)
29. A.H. Mueller, Nucl. Phys. **B213** (1983) 85.
30. X. Artru, G. Mennessier, Nucl. Phys. **B70** (1983) 93.
31. T. Sjöstrand, Phys. Lett **B185** (1987) 810.
32. G. Marchesini, B.R. Webber Nucl. Phys. **B310** (1988) 453.
33. T.D. Gottschalk, Nucl. Phys **B288** (1987) 279.
34. Mark II Collab., A. Peterson *et al.* Phys. Rev. **D37** (1988) 1.
35. P. Hoyer *et al.* Nucl. Phys. **B161** (1979) 349.
36. A. Ali *et al.* Nucl. Phys. **B168** (1980) 409.
37. J. Jackson *Classical Electrodynamics* (1975).
38. SLD Design Report, SLAC-273, UC-34D (1984).
39. Morris L. Swartz *Polarization at SLC* SLAC-PUB-4656 (1988).
40. C. Damerell, Nucl. Inst. and Meth. **A253** (1987) 478.
41. The Endcap Drift Chambers for the SLAC SLD Detector, submitted to **NIM**.
42. J. Va'Vra, Nuc. Inst. and Methods, **Vol 244, 1986**.
43. Cheng-Gang Fan, The DC Electric Filed Distribution in the EDC Drift Cell, CU-HEP-248.
44. Jan Lauber, A Study of the Drift Time vs. Distance for the EDC cell, unpublished.
45. John Carr, *SLD Note 174*, Oct 1987.
46. M. Böhm et al., CERN 89-08,*p.203*.
47. F.A. Berends, Nucl. Phys. **253** (1985) 441.
48. B. Ward, private communications (1991).
49. B. Andersson *et al.* Phys. Rep. **97** (1983) 31.
50. G.C. Fox, S. Wolfram, Nucl. Phs. B **168** (1980) 285.
51. OPAL Collaboration, Z. Phys. **C47**, (1990) 505.

52. JADE Collab., W. Bartel *et al.*, Z. Phys. **C33** (1986) 23.
53. N. Brown, W.J.Stirling, Finding Jets and summing soft gluons: a new algorithm, RAL-91-049 DTP/91/30 (1991).
54. S. Bethke *et al.*, New Jet Cluster Algorithms, CERN-TH.6222/91.
55. G. Kramer and B. Lampe, Z. Phys. **C34**, (1987) 497.
56. T. Sjöstrand, Computer Physics Commun. **28** (1983) 229.
57. R. Brun *et al.*, GEANT3 User's Guide, CERN DD/EE/84-1 (1989).
58. F. James, M. Ross. Minuit, CERN D506, 1989.04.20.
59. The OPAL Collab. CERN-PPE/92-18, (1992).
60. G. Altarelli, CERN-TH-5290/89; Ann. Rec. of Nucl. and Part. Science, Vol.39 (1989) 357.
61. S. Bethke and J.E. Pilcher, to be published in Ann. Rev. of Nucl.and Part.Sci., vol 42 (1992)¿
62. A.C. Benvenuti *et al.*, BCDMS Collab., Phys. Lett. **B223** (1989)490.
63. A.X. El-Kahadara *et al.*, FERMILAB-PUB-91/354-T.
64. J.A. Lauber *et al.*, SLAC-PUB 5974, 1992.
65. The JADE Collab., Phys. Lett. B, **213** (1988)235.
66. The TASSO Collab., Phys. Lett. B, **214** (1988)286.
67. The AMY Collab., Phys. Rev. Lett. **62** (1989)713.
68. The Mark II Collab., Z. Phys. C, **43** (1989)325.

APPENDIX A

THE ELECTROWEAK CROSS SECTION FOR e^+e^-ANNIHILATION

To obtain a meaningful result from an experiment it is essential to understand the theory we are comparing it against in detail. Foremost we have to know the cross section of the fundamental process $e^+e^- \rightarrow f\bar{f}$. Below I calculate the cross section for the decay into a muon pair and then generalize it for any fermion pair.

Two fundamental processes contribute, as described in chapter 1.2:

$$\left.\frac{d\sigma}{d\Omega}\right|_{cm} = \frac{1}{64\pi^2 s}\frac{p_f}{p_i}\left|\mathcal{M}_\gamma + \mathcal{M}_z\right|^2 \tag{A.1}$$

The electromagnetic part of the cross section $\mathcal{M}_\gamma$ is

$$\begin{aligned}\mathcal{M}_\gamma &= J^\nu_{muon}\frac{1}{q^2}\,J^e_\nu \\ &= -\frac{e^2}{s}\bar{\mu}(k')\gamma^\nu\mu(k)\bar{e}(p')\gamma_\nu e(p).\end{aligned} \tag{A.2}$$

μ and e in this expression are dirac spinors describing the wavefunction of the interacting particles.

$$e,\mu = \sqrt{E+m}\begin{pmatrix}\chi \\ \frac{\sigma\cdot p}{E+m}\chi\end{pmatrix};\quad \chi = \begin{pmatrix}1\\0\end{pmatrix},\begin{pmatrix}0\\1\end{pmatrix}$$

Squaring (A.2) we can write the result in a part that only depends on the electron wavefunction and one that only depends on the muon wavefunction:

$$\left|\mathcal{M}_\gamma\right|^2 = \frac{e^4}{s^2}L_e^{\mu\nu}L^{muon}_{\mu\nu} \tag{A.3}$$

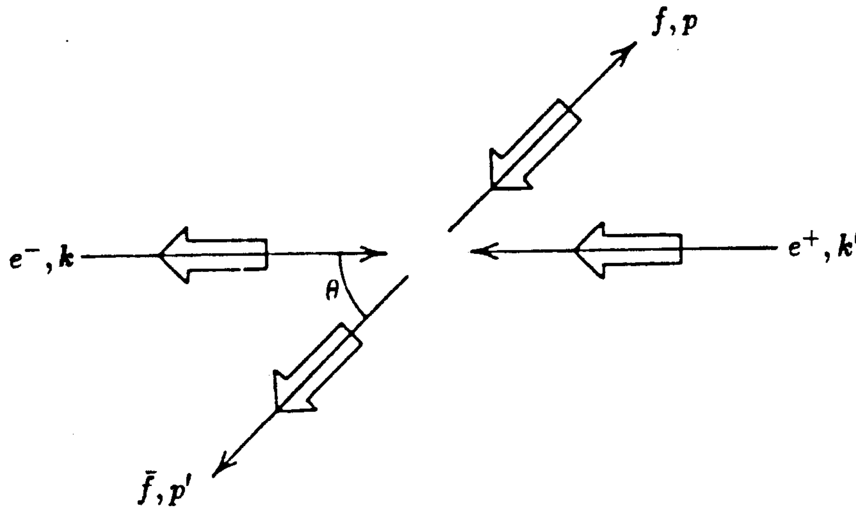

Fig A.1 Initial and final spin states.

where

$$
\begin{aligned}
L_e^{\mu\nu} &= \frac{1}{2}\sum_{spin} \left[\bar{v}(p')\gamma^\mu u(p)\right] \left[\bar{v}(p')\gamma_\mu u(p)\right]^* \\
&= \frac{1}{2}\sum_{s'} \underbrace{v_\delta(p')\bar{v}_\alpha(p')}_{(\not{p}'-m)_{\delta\alpha}} \gamma^\mu_{\alpha\beta} \sum_{s} \underbrace{u_\beta(p)\bar{u}_\gamma(p)}_{(\not{p}+m)_{\beta\gamma}} \gamma^\nu_{\gamma\delta} \qquad (A.4) \\
&= \frac{1}{2}\mathrm{Tr}(\not{p}'\gamma^\mu \not{p}\gamma^\nu) + \frac{1}{2}m^2 \mathrm{Tr}(\gamma^\mu\gamma^\nu).
\end{aligned}
$$

We wrote the sum over all spin states in form of a trace. Applying the trace rules

$$
L_e^{\mu\nu} = 2(p'^\mu k^\nu + p'^\nu p^\mu - (p' \cdot p - m^2)g^{\mu\nu}). \qquad (A.5)
$$

A similar expression can be derived for the muon, so

$$
\begin{aligned}
|\mathcal{M}_\gamma|^2 =& \frac{8e^4}{s^2}\left[(k' \cdot p')(k \cdot p) + (k' \cdot p)(k \cdot p') + M^2(k' \cdot k)\right] \\
=& \frac{8e^4}{s^2}p^4 \left[(1 - \frac{k}{p}\cos\vartheta)^2 + (1 + \frac{k}{p}\cos\vartheta)^2 + \frac{M^2}{p^2}\right],
\end{aligned} \qquad (A.6)
$$

where M is the mass of the muon and neglecting terms proportional to the electron mass. From Figure A.1 it is easy to see that $(k' \cdot k) = (p' \cdot p) = -p^2$, $(k' \cdot p) = (k \cdot p') = p^2 \cos^2 \vartheta$ and $(k' \cdot p') = (k \cdot p) = p^2 \sin^2 \vartheta$. Again, neglecting the mass of the electron $p_f/p_i = \sqrt{1 - 4M^2/s}$, so the electromagnetic part of the cross section is

$$\frac{d\sigma^{em}}{d\Omega} = \frac{\alpha^2}{64\pi^2 s}\sqrt{1 - \frac{4M^2}{s}}\left(1 + \cos^2\vartheta + \frac{4M^2}{s}\sin^2\theta\right). \qquad (A.7)$$

The weak part of the cross section gets somewhat more complicated:

$$\mathcal{M}_z = -\frac{g^2}{4\cos^2\theta_w}\left[\bar{\mu}\gamma^\nu(c_V^\mu - c_A^\mu\gamma^5)\mu\right]\left(\frac{g_{\nu\sigma} - k_\nu k_\sigma/M_z^2}{k^2 - M_z^2}\right)\left[\bar{e}\gamma^\sigma(c_V^e - c_A^e\gamma^5)e\right]. \qquad (A.8)$$

Substituting

$$c_R \equiv c_V - c_A, \qquad c_L \equiv c_V + c_A \qquad (A.9)$$

we can write

$$c_V - c_A\gamma^5 = \frac{1}{2}c_R(1+\gamma^5) + \frac{1}{2}c_L(1-\gamma^5) \qquad (A.10)$$

The $1/2(1 \pm \gamma^5)$ are projection operators, so, $\mathcal{M}_z$ can be expressed explicitly in terms of right- and left-handed spinors. Ignoring the electron mass, the Dirac equation for the incoming positron reads $1/2k_\sigma\bar{e}\gamma^\sigma = 0$ and the numerator of the propagator simplifies to $g_{\nu\sigma}$ and the weak part of the invariant amplitude becomes

$$\mathcal{M}_z = -\frac{g^2}{4\cos^2\theta_w}\left[c_R^\mu(\bar{\mu}_R\gamma^\nu\mu_R) + c_L^\mu(\bar{\mu}_L\gamma^\nu\mu_L)\right]\left[c_R^e(\bar{e}_R\gamma_\nu e_R) + c_L^e(\bar{e}_L\gamma_\nu e_L)\right] \qquad (A.11)$$

$\mathcal{M}_\gamma$ in (A.2) can be put into a similar form

$$\mathcal{M}_\gamma = -\frac{e^2}{s}\left[\bar{\mu}_R\gamma^\nu\mu_R 6i + \bar{\mu}_L\gamma^\nu\mu_L\right]\left[\bar{e}_R\gamma_\nu e_R + \bar{e}_L\gamma_\nu e_L\right] \qquad (A.12)$$

so the sum of the two amplitudes takes the form

$$\begin{aligned}\mathcal{M}_\gamma + \mathcal{M}_z = -\frac{e^2}{s}\,[&(1 + a\xi c^\mu_R c^e_R)(\bar\mu_R\gamma^\nu\mu_R)(\bar e_R\gamma_\nu e_R)\\ &+(1 + a\xi c^\mu_R c^e_L)(\bar\mu_R\gamma^\nu\mu_R)(\bar e_L\gamma_\nu e_L)\\ &+(1 + a\xi c^\mu_L c^e_R)(\bar\mu_L\gamma^\nu\mu_L)(\bar e_R\gamma_\nu e_R)\\ &+(1 + a\xi c^\mu_L c^e_L)(\bar\mu_L\gamma^\nu\mu_L)(\bar e_L\gamma_\nu e_L)\end{aligned} \tag{A.13}$$

where

$$a = \frac{1}{4\cos^2\theta_w \sin^2\theta_w}, \qquad \xi = \frac{s}{s - M_z^2 + i\Gamma_z M_z} \tag{A.14}$$

When squaring (A.13) we get 16 terms that look very similar to (A.6). But since left-handed e^- and μ^- don't couple to left-handed e^+ and μ^+, and the same for the right-handed particles, most terms vanish:

$$\begin{aligned}e^+_L\gamma^\nu e^-_L =&\frac{1}{4}e^+(1+\gamma^5)\gamma^\nu(1+\gamma^5)e^-\\ =&\frac{1}{4}e^+\gamma^\nu(1-\gamma^5)(1+\gamma^5)e^-\\ =&0\end{aligned} \tag{A.15}$$

where we used $\gamma^\nu\gamma^5 = -\gamma^5\gamma^\nu$ and $(\gamma^5)^2 = 0$. The nonvanishing terms take the form

$$\begin{aligned}\frac{d\sigma}{d\Omega}(e^-_L e^+_R \to \mu^-_L\mu^+_R) =&\frac{\alpha^2}{4s}\sqrt{1-\frac{4M^2}{s}}\left((1+\frac{k}{p}\cos\vartheta)^2 + \frac{M^2}{2p^2}\right)\left|1 + a\xi c^\mu_L c^e_L\right|^2\\ \frac{d\sigma}{d\Omega}(e^-_L e^+_R \to \mu^-_R\mu^+_L) =&\frac{\alpha^2}{4s}\sqrt{1-\frac{4M^2}{s}}\left((1-\frac{k}{p}\cos\vartheta)^2 + \frac{M^2}{2p^2}\right)\left|1 + a\xi c^\mu_R c^e_L\right|^2\end{aligned} \tag{A.16}$$

and similar expressions result for the two other terms with the right-handed electron and the left-handed positron. To obtain the total cross section we have to sum over the initial states and average over the final states. In an unpolarized beam we find an equal number of left- and right-handed particles. But for a polarized beam we have to weight the terms differently. For $P^-(P^+) = 1$, the polarization of the electrons, all the electrons (positrons) in the beam are left-handed and for $P = 0$ half are left-handed and half are right-handed. Substituting the four helicity configurations by A, B, C and D the total cross section becomes

$$\begin{aligned}\frac{d\sigma}{d\Omega} =& \frac{1}{2}\left[(1+P^-)(1-P^+)(A+B) + (1-P^-)(1+P^+)(C+D)\right] \\ =& [1-P^+P^-](A+B+C+D) - [P^+ - P^-](A+B-C-D)\end{aligned} \qquad (A.17)$$

which results in the expression

$$\begin{aligned}\frac{d\sigma}{d\Omega} = \frac{\alpha^2}{4s}\sqrt{1-\frac{4M^2}{s}}(1-P^+P^-)&\left[A_0(1+\cos^2\vartheta) + A_1\frac{4M^2}{s}\sin^2\vartheta + A_2\cos\vartheta\right] \\ -(P^+ - P^-)&\left[A_3(1+\cos^2\vartheta) + A_4\frac{4M^2}{s}\sin^2\vartheta + A_5\cos\vartheta\right]\end{aligned} \qquad (A.18)$$

where

$$\begin{aligned}A_0 =& q_e^2q_f^2 + 2q_eq_fv_ev_fRe(\xi) + (v_e^2+a_e^2)(v_f^2+a_f^2-\frac{4M^2}{s}a_f)\,|\xi|^2 \\ A_1 =& q_e^2q_f^2 + 2q_eq_fv_ev_fRe(\xi) + (v_e^2+a_e^2)v_f^2\,|\xi|^2 \\ A_2 =& 2q_eq_fa_ea_fRe(\xi) + 4v_ea_ev_fa_f\,|\xi|^2 \\ A_3 =& 2q_eq_fv_fa_eRe(\xi) + 2(v_f^2+a_f^2-\frac{4M^2}{s}a_f)v_ea_e\,|\xi|^2 \\ A_4 =& 2q_eq_fv_fa_eRe(\xi) + 2v_f^2v_ea_e\,|\xi|^2 \\ A_5 =& 4q_eq_fa_fv_eRe(\xi) + 4v_fa_f\,|\xi|^2\end{aligned} \qquad (A.19)$$

For P^+ and $P^- = 0$ this reduces to the expression A.20. For nonzero polarization, but neglecting all terms proportional to $\frac{M^2}{s}$ we get the formula 1.2 in chapter 1.2.

$$
\begin{aligned}
\frac{d\sigma}{d\cos\vartheta} = N_c \frac{\pi\alpha^2}{2s}\sqrt{1-\frac{4m_f^2}{s}} \times \left\{ Q_e^2 Q_f^2 \left[1+\cos^2\vartheta + \frac{4m_f^2}{s}\sin^2\vartheta \right] \right\} \\
\times \left\{ 2Q_e Q_f \mathrm{Re}\xi_0 \left[v_e v_f \left(1+\cos^2\vartheta + \frac{4m_f^2}{s}\sin^2\vartheta \right) + 2a_e a_f \sqrt{1-\frac{4m_f^2}{s}}\cos\vartheta \right] \right\} \\
\times \left\{ |\xi_0|^2 \left[(v_e^2+a_e^2) \left[\left(v_f^2 + (1-\frac{4m_f^2}{s})a_f^2 \right)(1+\cos^2\vartheta) + v_f^2\frac{4m_f^2}{s}\sin^2\vartheta \right] \right.\right. \\
\left.\left. + 8v_e a_e v_f a_f \sqrt{1-4\frac{m_f^2}{s}}\cos\vartheta \right] \right\}
\end{aligned}
\qquad (A.20)
$$

APPENDIX B

THE SLD COLLABORATION

Adelphi University: R. Steiner;

Boston University: J. Coller, A. Johnson, J.T. Shank, M. Tahar, D. Warner, J.S. Whitaker, B. Wilson;

Brunel University: P.D. Acton, G. Agnew, P.E.L. Clarke, R. Cotton, S. Hedges, A.K. McKemey, S.J. Watts;

Calif. Inst. of Technology: F. DeJongh, G. Eigen, D.G. Hitlin, M.H. Kelsey, M. Klein, A.I. Mincer, W.J. Wisniewski;

Columbia University: C. Arroyo, Y. Au, A.O. Bazarko, T. Bolton, L. Camilleri, E. Hyatt, P.C. Rowson, M.H. Shaevitz;

Indiana University: H. Ogren, D. Rust, A. Snyder;

INFN Sezione di Bologna: A.C. Benvenuti;

INFN Sezione di Ferrara and Universitá di Ferrara: B. Camanzi, E. Dicapua, E. Mazzucato, L. Piemontese, B. Saitta, P. Zuchelli;

INFN, Sezione di Pisa: M. Carpinelli, R. Castaldi, R. Dell'Orso, E. Pieroni, C. Vannini, P.G. Verdini;

KEK National Lab: J. Fujimoto;

Lab. Nazionali di Frascati: A. Calcaterra, R. De Sangro, P. De Simone, S. De Simone, M. Gallinaro, I. Peruzzi, M. Piccolo;

Lawrence Berkeley Laboratory: M. Kowitt, B. Schumm, G. Shapiro, H. Steiner;

Massachusetts Institute of Tech.: O. Bardon, P.N. Burrows, W. Busza, S. Cartwright, R.F. Cowan, B. Farhat, M.J. Fero, J.I. Friedman, S. Gonzalez, T. Hansl-Kozanecka, H.W. Kendall, A. Lath, T. Lyons, L.S. Osborne, A. Palounek, J. Quigley, L. Rosenson, U. Schneekloth, F.E. Taylor, E. Torrence, R. Verdier, B.F. Wadsworth, D.C. Williams, R.K. Yamamoto, J.M. Yamartino;

Nagoya University: R. Kajikawa, A. Sugiyama, S. Suzuki;

Rutgers University: K.G. Baird, P. Jacques, M. Kalelkar, J.N. Matthews, R.J. Plano, P. Stamer, G.B. Word;

Rutherford Appleton Laboratory: C.J.S. Damerell, R.L. English, T. Gillman, L. Lintern, R.J. Stephenson, D. Su, G.J. Tappern, F.J. Wickens;

Stanford Linear Accelerator Center: D.F. Alzofan, P. Antilogus, W.W. Ash, M.D. Aston, W.B. Atwood, W. Baker, F. Barrera, R.A. Bell, R. Berger, E. Beville, T. Bienz, R. Blumberg, J.R. Bogart, G.R. Bower, R.F. Boyce, M. Breidenbach, T.E. Browder, D. Burke, B. Burgess, B.L. Byers, R. Cassell, R. Claus, G.B. Chadwick, D. Chambers, W. Craddock, H. Cutler, R. Davis, S. Dasu, T. Dean, R. Dubois, W. Dunwoodie, J. Escalera, R.D. Elia, F. Fernandez-Texon, J. Ferrie, J. Flynn, J.D. Fox, M.J. Fox, D.R. Freytag, G.M. Haller, G.D. Hallewell, V. Hamilton, M. Hildreth, R.C. Hilomen, J. Hodgson, J.J. Hoeflich, D. Horelick, M.E. Huffer, E.W. Hughes, C. Jako, S. Jones, T. Junk, S. Kaiser, H. Kang, H. Kawahara, D. Kharakh, P.C. Kim, R. King, P.F. Kunz, Y. Kwon, J.F. Labs, R. Larsen, D.W.G. Leith, H.L. Lynch, D. Mansour, T.W. Markiewicz, T. Maruyama, H. Masuda, G. Mazaheri, R. Messner, K.C. Moffeit, B. Mours, G. Mueller, D. Muller, T. Nagamine, H. Neal, D. Nelson, M. Nordby, A. Nuttall, J. Olsen, R. Ossa, G. Oxoby, L. Paffrath, T.J. Pavel, H. Petersen, M. Petradza, C.Y. Prescott, G.D. Punkar, G. Putallaz, B.N. Ratcliff, P.E. Rensing, R. Rinta, L.S. Rochester, A. Rothenberg, J.J. Russell, P. Saez, O.H. Saxton, R.H. Schindler, D. Schultz, S.L. Shapiro, H. Shaw, D.J. Sherden, C. Simopoulous, K. Skarpaas, S.R. Smith, P. Stiles, M. Swartz, T. Takahashi, N. Toge, T. Usher, J. Va'Vra, A.P. Waite, D. Walz, R. Watt, T. Weber, S.H. Williams, C. Yee, A. Yim, C.C. Young, R.W. Zdarko;

Tohoku University: K. Abe, K. Hasegawa, Y. Hasegawa, Y. Iwasaki, F. Suekane, H. Yuta;

TRIUMF: D.P. Gurd, C. Oram;

U.C. Santa Barbara: D.A. Bauer, A. Bean, D.O. Caldwell, R. Dolin, J.E. Duboscq, D.L. Hale, J. Huber, A. Lu, L. Mathys, S. McHugh, R.J. Morrison, J.D. Richman, S.A. Wickert, M.S. Witherell, S.J. Yellin;

U.C. Santa Cruz: G. Blaylock, M. Cavalli-Sforza, P.A. Coyle, D.G. Coyne, X. Liu, T. Schalk, M. Schneider, A. Seiden, E.N. Spencer, D.A. Williams;

Universita di Padova: N. Bacchetta, D. Bisello, A. Castro, M. Loreti, A. Mazzucato, L. Pescara, M. Tecchio, J. Wyss;

Universita di Perugia: R. Battiston, M. Biasini, G.M. Bilei, G. Mancinelli, G. Mantovani, M. Pauluzzi, L. Servoli;

University of British Columbia: D.A. Axen, S. Bougerolle, D. Peters, R.L. Shypit, R. Sobie;

University of Cincinnati: K. Choi, A. D'Oliveira, R.A. Johnson, J.L. Martinez, B.T. Meadows, M. Nussbaum, E. Rutz, A.K. Santha, A. Shoup, M.D. Sokoloff, I.E. Stockdale;

University of Colorado: C. Alber, G.J. Baranko, J. Carr, D.D. Durrett, E. Erdos, C. Fan, N.M. Krishna, J.A. Lauber, U. Nauenberg, P. Rankin, G. Schultz;

University of Illinois: I. Abt, D. Blockus, R.W. Downing, B.I. Eisenstein, K.M. Fortune, G. Gladding, M.J. Haney, J.M. Izen, I. Karliner, W.A. Majid, J.F. McGowan, D.J. Mellor, G. Stewart, J.J. Thaler;

University of Massachusetts: R.J. Belcinski, S.S. Hertzbach, R. Kofler, M.G. Strauss;

University Of Oregon: J. Brau, R. Frey, K. Furuno, H. Hwang, H. Park, K.T. Pitts, C. Zeitlin;

University of Tennessee: S.C. Berridge, B. Bugg, H.O. Cohn, P. Du, T. Handler, E.L. Hart, R.S. Kroeger, A.W. Weidemann, S.L. White;

University of Victoria, TRIUMF: A. Astbury, G. Beer, T.A. Hodges, A. Honma, R.K. Keeler, R.R. Langstaff, G.R. Mason, P.R. Poffenberger, L.P. Robertson, P.R. Schenk, M. Turcotte;

University of Washington: T.H. Burnett, V. Cook, D.A. Forbush, J. Harrison, H.Y. Kim, J. Ma, P.M. Mockett, J.E. Rothberg, A. Szumilo, F. Toevs, E. Vella, R.W. Williams, K.K. Young;

University of Wisconsin: H.R. Band, J.R. Johnson, R. Prepost, G. Zapalac;

Vanderbilt University: L-P Chen, R.S. Panvini, T.W. Reeves, J.P. Venuti;

Yale University: C. Baltay, R. Ben-David, A. Disco, W.T. Emmet II, S. Manly, J.A. Snyder, J.D. Turk.